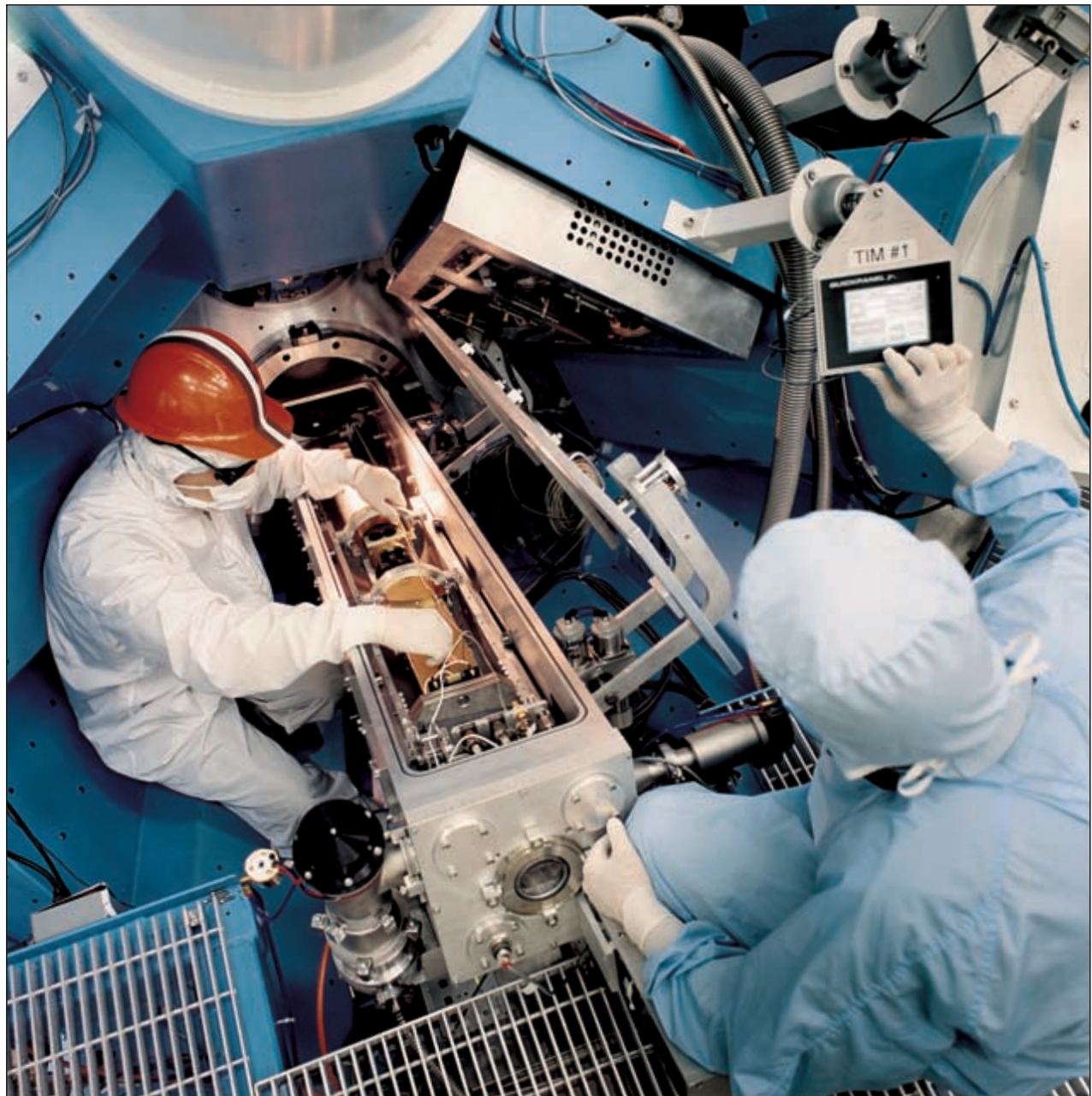


# LLE Review

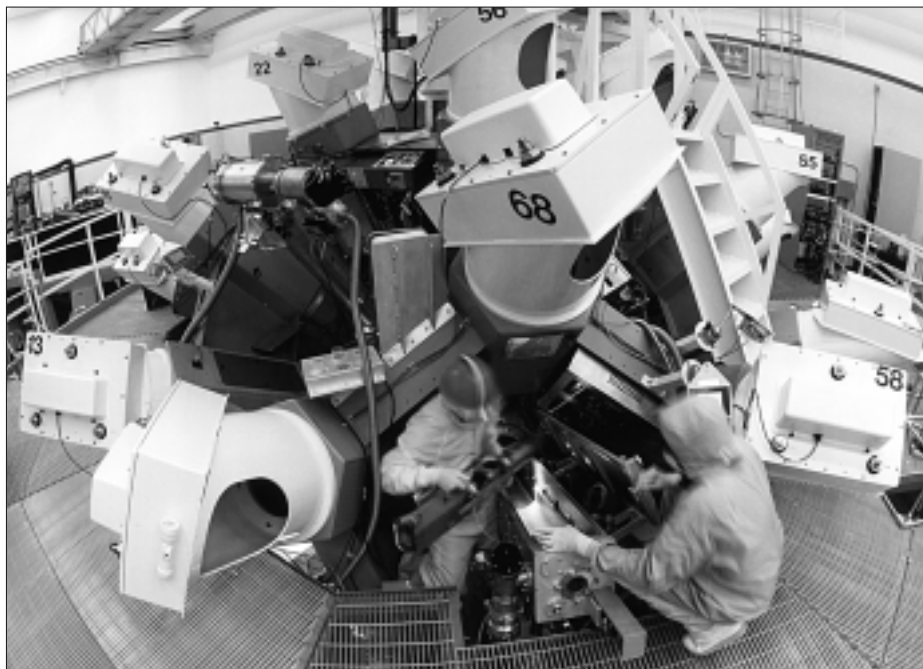


## Quarterly Report



## About the Cover:

The cover photograph shows Laboratory Engineer Charles Sorce and Research Engineer Ray Bahr inserting an x-ray streak camera into a ten-inch manipulator (TIM). This streak camera was used to record the Ar *K*-shell spectra for the experiments described in the article beginning on p. 47. The camera used a flat RbAP (rubidium acid phthalate) crystal to disperse the x-ray spectrum onto an Au cathode, and it was operated with a 2-ns temporal window to attain a temporal resolution of 25 ps.



The diagnostics on the OMEGA system are divided between those that are permanently attached to the target chamber and those, such as the streak camera shown in the photograph, that are inserted with one of the six OMEGA TIM's. TIM-based diagnostics are removable and can be reconfigured between system shots. The TIM's provide a great deal of flexibility in the configuration of diagnostic systems to meet the needs of the various experiments.

This report was prepared as an account of work conducted by the Laboratory for Laser Energetics and sponsored by New York State Energy Research and Development Authority, the University of Rochester, the U.S. Department of Energy, and other agencies. Neither the above named sponsors, nor any of their employees, makes any warranty, expressed or implied, or assumes any legal liability or responsibility for the accuracy, completeness, or usefulness of any information, apparatus, product, or process disclosed, or represents that its use would not infringe privately owned rights. Reference herein to any specific commercial product, process, or service by trade name, mark, manufacturer, or otherwise, does not necessarily constitute or imply its endorsement, recommendation, or favoring by

the United States Government or any agency thereof or any other sponsor. Results reported in the LLE Review should not be taken as necessarily final results as they represent active research. The views and opinions of authors expressed herein do not necessarily state or reflect those of any of the above sponsoring entities.

The work described in this volume includes current research at the Laboratory for Laser Energetics, which is supported by New York State Energy Research and Development Authority, the University of Rochester, the U.S. Department of Energy Office of Inertial Confinement Fusion under Cooperative Agreement No. DE-FC03-92SF19460, and other agencies.

Printed in the United States of America  
Available from  
National Technical Information Services  
U.S. Department of Commerce  
5285 Port Royal Road  
Springfield, VA 22161

For questions or comments, contact John M. Soures, *Editor*,  
Laboratory for Laser Energetics, 250 East River Road, Rochester, NY 14623-1299, (716) 275-3866.

Price codes: Printed Copy A04  
Microfiche A01

Worldwide-Web Home Page: <http://www.lle.rochester.edu/>

# LLE Review



## Quarterly Report

### Contents

In Brief .....	iii
Characterization of Direct-Drive-Implosion Core Conditions on OMEGA with Time-Resolved Ar <i>K</i> -Shell Spectroscopy .....	47
Study of Direct-Drive, DT-Gas-Filled-Plastic-Capsule Implosions Using Nuclear Diagnostics on OMEGA .....	54
A Consistent Measurement-Based Picture of Core-Mix in Direct-Drive Implosions on OMEGA .....	68
High-Resolution Neutron Imaging of Laser-Imploded DT Targets .....	74
The Smoothing Performance of Ultrafast Pickets on the NIF .....	79
Tests of EXAFS on OMEGA: Feasibility for Shock-Heating Measurements .....	92
Microhardness and Indentation Fracture of Potassium Dihydrogen Phosphate (KDP) .....	101
Publications and Conference Presentations	



## In Brief

This volume of LLE Review, covering January–March 2001, includes a report on the characterization of direct-drive implosion core conditions using time-resolved Ar *K*-shell spectroscopy. This work was carried out by a team that included S. P. Regan, J. A. Delettrez, P. A. Jaanimagi, B. Yaakobi, V. A. Smalyuk, F. J. Marshall, D. D. Meyerhofer, and W. Seka of the Laboratory for Laser Energetics (LLE), University of Rochester; D. A. Haynes, Jr. of the Department of Engineering Physics, University of Wisconsin; and C. F. Hooper, Jr. of the Department of Physics, University of Florida. The experiments involved the implosion of polymer shells filled with Ar-doped deuterium gas driven with up to 24-kJ, 1-ns square laser pulses smoothed with 1-THz, 2-D smoothing by spectral dispersion (SSD) and polarization smoothing (PS). The emissivity-averaged core electron temperature and density were inferred from the measured time-dependent Ar *K*-shell spectral line shapes. Electron densities in excess of  $2.5 \times 10^{24} \text{ cm}^{-3}$  and electron temperatures  $\sim 2.5 \text{ keV}$  were measured in these experiments. This represents the highest combination of electron temperature and density measured for these types of implosions in laser-driven inertial fusion experiments.

Additional research highlights reported in this issue include the following:

- C. K. Li, F. H. Séguin, D. G. Hicks, J. A. Frenje, K. M. Greene, S. Kurebayashi, and R. D. Petrasso of the Massachusetts Institute of Technology (MIT) Plasma Science and Fusion Center (PSFC); D. D. Meyerhofer, J. M. Soures, V. Yu. Glebov, R. L. Keck, P. B. Radha, S. Roberts, S. Skupsky, and C. Stoeckl of LLE; and T. C. Sangster of Lawrence Livermore National Laboratory (LLNL) report on studies of the implosions of direct-drive, DT-gas-filled polymer capsules using nuclear diagnostics. In addition to traditional neutron measurements, a comprehensive array of knock-on deuteron, triton, and proton spectra were used to compare the performance of capsules irradiated with full beam smoothing on OMEGA (1-THz, 2-D SSD and PS) versus implosions of similar targets carried out with reduced beam smoothing (0.35-THz, 2-D SSD without PS). With full beam smoothing, implosions with moderate radial convergence ( $\sim 10$  to  $20$ ) are shown to produce neutron yields, fuel areal densities, and shell areal densities approximately 80%, 60%, and 35% higher, respectively, than those with the reduced level of beam smoothing.
- To improve the understanding of the moderate-convergence-ratio ( $\sim 10$  to  $20$ ), direct-drive implosions carried out on OMEGA, P. B. Radha, V. Yu. Glebov, D. D. Meyerhofer, C. Stoeckl, and J. M. Soures of LLE in collaboration with C. K. Li, R. D. Petrasso, and F. H. Séguin of MIT-PSFC developed a consistent measurement-based static model of the stagnated core and fuel–pusher mix. The model, presented in this issue, assumes that the imploded core is comprised of a clean fuel region and a “mix” region where the shell material is mixed into the fuel. Excellent agreement with a suite of neutron and particle diagnostics is obtained through the use of this model. The model suggests that approximately  $1 \mu\text{m}$  of shell material is mixed into the fuel during the thermonuclear burn. It also suggests that the fuel areal density is distributed equally between the clean core and the fuel–shell mix region.
- L. Disdier, A. Rouyer, J-P Garconnet, A. Fedotoff, and J.-L. Bourgade of the Commissariat à l'Énergie Atomique (CEA) of France; V. Yu. Glebov, C. Stoeckl, and W. Seka of LLE; and D. C. Wilson of the Los Alamos National Laboratory (LANL) discuss high-resolution neutron imaging of capsules imploded on the OMEGA laser. Their diagnostic is based on penumbral imaging using a

biconical aperture. The CEA-designed diagnostic demonstrated the highest spatial resolution yet achieved on ICF implosions (45 to 60  $\mu\text{m}$ ) on direct-drive implosions carried out on the OMEGA facility. Modifications that are expected to improve the resolution to 13  $\mu\text{m}$  for OMEGA implosions have recently been carried out on this diagnostic.

- Ultrafast picket-fence pulses have been proposed by an LLNL scientist as a means to maximize the frequency-conversion efficiency and minimize beam-power imbalance on the National Ignition Facility (NIF). In this issue J. A. Marozas and J. D. Zuegel of LLE report on the results of an analysis of the beam-smoothing performance of ultrafast picket-fence pulses for direct-drive targets on the NIF. They found that beam smoothing achieved with ultrafast picket-fence pulses is equivalent to the smoothing attained with the NIF's base-line 2-D SSD design if the applied bandwidth and divergence used for the picket-fence-configuration SSD is close to that of the base-line-design SSD system. Furthermore, it is shown that the diffraction-limited far-field pattern produced by chirped picket-fence pulses can reduce the pinhole loading, potentially leading to a larger permissible beam divergence for the NIF with 2-D SSD.
- B. Yaakobi, F. J. Marshall, T. R. Boehly, R. P. J. Town, D. D. Meyerhofer, and W. Seka report on a test of the feasibility of using extended x-ray absorption spectrum (EXAFS) to characterize the properties of solid materials shocked at moderately high pressures (up to a few Mbar). This work is part of LLE's participation in the Department of Energy's Stewardship Science Program (SSP). The initial results presented in this issue show very-high-contrast EXAFS modulations when a thick, undriven Ti foil is backlit by the x-ray radiation from an imploded CH shell.
- KDP is an important electro-optic tetragonal crystal used widely in high-power laser systems. In this issue, T. Fang of Crystal Technologies and J. C. Lambropoulos of the UR's Department of Mechanical Engineering and LLE report on studies of the microhardness and indentation fracture of KDP. They develop an approximate model for analyzing crack-load micro-indentation data in tetragonal crystals. The model uses the minimum elastic modulus of the material.

John M. Soures  
*Editor*

# Characterization of Direct-Drive-Implosion Core Conditions on OMEGA with Time-Resolved Ar *K*-Shell Spectroscopy

## Introduction

In the direct-drive approach to inertial confinement fusion (ICF), capsules are directly irradiated by a large number of symmetrically arranged laser beams.<sup>1,2</sup> Time-resolved Ar *K*-shell spectroscopy has been established as a reliable technique to diagnose the compressed core of direct-drive implosions,<sup>3–10</sup> as well as indirect-drive implosions.<sup>6,11–16</sup> This technique has been used on the 60-beam OMEGA laser system<sup>17</sup> to characterize the core conditions of direct-drive implosions. Plastic shells with an Ar-doped deuterium fill gas were driven with a 23-kJ, 1-ns square laser pulse smoothed with phase plates,<sup>18</sup> 1-THz smoothing by spectral dispersion (SSD),<sup>19–21</sup> and polarization smoothing (PS) using birefringent wedges.<sup>22</sup> Laser beam smoothing reduces the effects of the ablative Rayleigh–Taylor hydrodynamic instability by reducing the initial imprint levels.<sup>23</sup> The targets in this experiment are predicted to have a convergence ratio of  $\sim 15$ . Measured convergence ratios of 14 have been reported for similar capsules on OMEGA.<sup>24</sup> The emissivity-averaged core electron temperature and density were inferred from the measured time-dependent Ar *K*-shell spectral line shapes.

Two properties of the Ar *K*-shell spectrum emitted from hot, dense plasmas ( $n_e > 10^{23} \text{ cm}^{-3}$ ;  $T_e > 1 \text{ keV}$ ) are exploited to infer a unique combination of emissivity-averaged core electron temperature and density: (1) The line shapes depend strongly on density and are relatively insensitive to variations in electron temperature. (2) The relative intensities of the Ar *K*-shell lines and their associated *L*-shell satellites are sensitive to variations in electron temperature and density.<sup>8</sup> The Stark-broadened line profiles for the Ar He $\beta$  ( $1s3l-1s^2$ ), He $\gamma$  ( $1s4l-1s^2$ ), He $\delta$  ( $1s5l-1s^2$ ), and Ly $\beta$  ( $3l-1s$ ) resonant transitions and associated satellites were calculated using a second-order quantum mechanical relaxation theory.<sup>8</sup> These line profiles were combined using relative intensities derived from a detailed non-LTE kinetics code corrected for the effects of radiative transfer using an escape-factor approximation. The Stark-broadened line profiles were corrected for the effects of opacity using a slab opacity model.

In this article we present time-resolved Ar *K*-shell spectroscopic measurements of a direct-drive implosion on OMEGA. The following sections (1) describe experimental setup, including the photometric calibration of the spectroscopic diagnostics; (2) describe the atomic physics model and the line-fitting procedure; (3) compare the modeled spectra with the measured data; and (4) give the inferred temporal evolution of the electron temperature and density. Conclusions are presented in the last section.

## Experimental Setup

The layout of the experimental setup on OMEGA and a schematic of the target are shown in Fig. 86.1. The 20- $\mu\text{m}$ -thick, 954- $\mu\text{m}$ -diam plastic shell with an Ar-doped deuterium fill gas was driven with a 24-kJ, 1-ns square laser pulse, and the Ar *K*-shell emission was recorded with time-resolved and time-integrated flat crystal spectrometers. The total fill pressure was 15 atm with an atomic Ar percentage of 0.18 resulting in a partial pressure of Ar of  $\sim 0.05 \text{ atm}$ . The impact of the Ar dopant on the capsule performance reduces the primary neu-

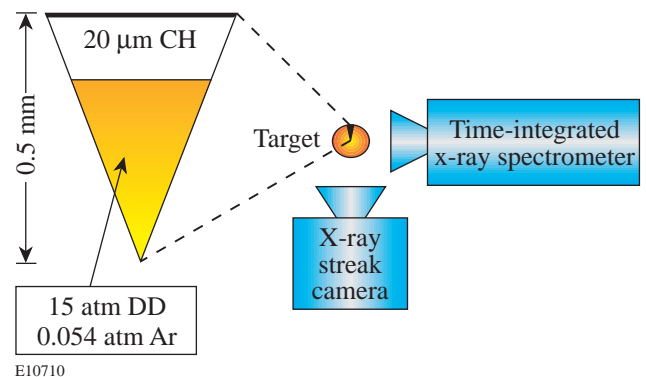


Figure 86.1

The layout of the experimental setup on OMEGA and a schematic of the target. The plastic shell with an Ar-doped deuterium fill gas was driven with a 23-kJ, 1-ns square laser pulse. The total fill pressure was 15 atm with an atomic Ar percentage of 0.18 resulting in a partial pressure of Ar of  $\sim 0.05 \text{ atm}$ . Streaked and high-resolution, time-integrated x-ray spectra of Ar *K*-shell emission were recorded with flat crystal spectrometers.

tron yield to  $\sim 75\%$  of an undoped target.<sup>24</sup> The on-target beam uniformity has been significantly improved on OMEGA: single-beam irradiation nonuniformity has been reduced with 1-THz SSD and PS, and the beam-to-beam rms power imbalance is 5% or less for square laser pulses.<sup>24</sup>

The time-dependent Ar *K*-shell spectral line shapes were monitored using time-resolved x-ray spectroscopy. Two x-ray streak cameras were fielded for this experiment: one had an  $\sim 2$ -ns temporal window and was used to measure the spectral line shapes with 25-ps temporal resolution; the other had an  $\sim 4$ -ns temporal window and was used to measure the absolute timing of the Ar *K*-shell emission with an accuracy of 50 ps.

The spectrum recorded with the faster streak camera is shown in Fig. 86.2 with temporal streak distortions removed. This spectral range includes the following Ar *K*-shell resonance lines: Ar Ly $_{\alpha}$  ( $2l-1s$ ), He $_{\beta}$  ( $1s3l-1s^2$ ), He $_{\gamma}$  ( $1s4l-1s^2$ ), Ly $_{\beta}$  ( $3l-1s$ ), He $_{\delta}$  ( $1s5l-1s^2$ ), He $_{\epsilon}$  ( $1s6l-1s^2$ ), Ly $_{\gamma}$  ( $4l-1s$ ), Ly $_{\delta}$  ( $5l-1s$ ), and Ly $_{\epsilon}$  ( $6l-1s$ ). The prominent ones have been identified in Fig. 86.2. The x-ray streak camera,<sup>25</sup> which utilized a flat RbAP (rubidium acid phthalate) crystal to disperse the spectrum onto an Au photocathode, was timed (see Fig. 86.2) to capture the coronal plasma emission at the end of the laser pulse just after 1 ns through the peak x-ray emission at 2 ns. The slower streak camera recorded the same spectral range with a similar spectrometer; however, as shown in Fig. 86.3, it was timed to record the entire evolution of the x-ray emission from the start of the coronal plasma emission when the laser strikes the target to the peak x-ray production at

peak compression. Temporal streak distortions have also been removed from the time-resolved spectra in Fig. 86.3. The time axis of the slower streak camera was established with the temporally modulated ultraviolet fiducial laser pulse (see Fig. 86.3). The exponential rise of the coronal plasma emission was extrapolated back to the beginning of the laser pulse.

The absolute timing of the peak x-ray emission in Fig. 86.2 was taken from Fig. 86.3. The average sweep speed of the faster streak camera was measured to be 48 ps/mm on a subsequent shot during the experimental campaign using a temporally modulated ultraviolet fiducial laser pulse. As seen in Fig. 86.2, the onset of the Ar *K*-shell line emission occurs during the shock heating beginning at  $\sim 1.6$  ns, and as the implosion proceeds, the amount of Stark-broadening increases. The dispersion of the streaked spectrum was determined using the relatively narrow spectral features observed just after the onset of the Ar *K*-shell emission lines at  $t = 1.77$  ns (see Fig. 86.4). The modeled spectrum also shown in Fig. 86.4 is discussed in the next section. A portion of the streak camera's x-ray photocathode was blocked, providing a wavelength fiducial (see Fig. 86.2) to establish the orientation of the streak axis. The spectra were recorded on Kodak T-max 3200 film. The film was digitized using a PDS (Perkin-Elmer Photometric Data Systems) microdensitometer and corrected for film sensitivity.

The streaked spectra were corrected for variations in x-ray spectral sensitivity and streak camera flat-fielding effects using the photometrically calibrated spectra of a time-integrated

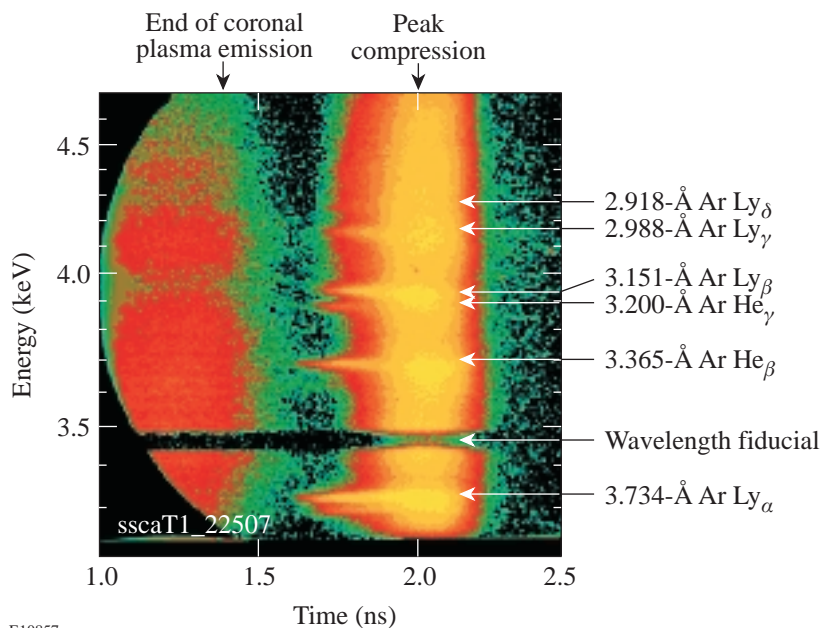


Figure 86.2

The time-resolved Ar *K*-shell spectral measurement with an  $\sim 2$ -ns temporal window for shot number 22507. Temporal streak distortions have been removed, and the orientation of the streak axis is determined with the wavelength fiducial. The onset of the Ar *K*-shell line emission occurs during the shock heating beginning at  $\sim 1.6$  ns, and the Stark-broadening increases as the implosion proceeds. The dispersion of the streaked spectrum was determined using the relatively narrow spectral features observed just after the onset of the Ar *K*-shell emission lines.

spectrometer. The time-integrated instrument utilized an ADP (ammonium dihydrogen phosphate) crystal to disperse the spectrum onto Kodak DEF (direct exposure) film. This instrument was calibrated using a combination of measured and published crystal reflectivities,<sup>26</sup> and the film was digitized with the PDS microdensitometer and corrected for film sensitivity. The bremsstrahlung emission from an undoped capsule, which was measured with the time-integrated spectrometer and found to be characteristic of an electron temperature equal to 0.68 keV, was used to calibrate the time-resolved spectra. The streaked spectrum was integrated in time and compared

with the bremsstrahlung emission. The ratio of these two quantities is the photometric calibration of the streaked spectrum. The calibration, which is applied to each time-resolved spectra, is shown in Fig. 86.5.

**Atomic Physics Modeling**

Time-resolved Ar *K*-shell spectroscopy is a technique that allows the emissivity-averaged electron temperature and density to be inferred. The Stark-broadened Ar *K*-shell spectral line shapes are calculated with the Multi-Electron Radiator Lineshape (MERL) code<sup>27</sup> in the manner described in Ref. 8.

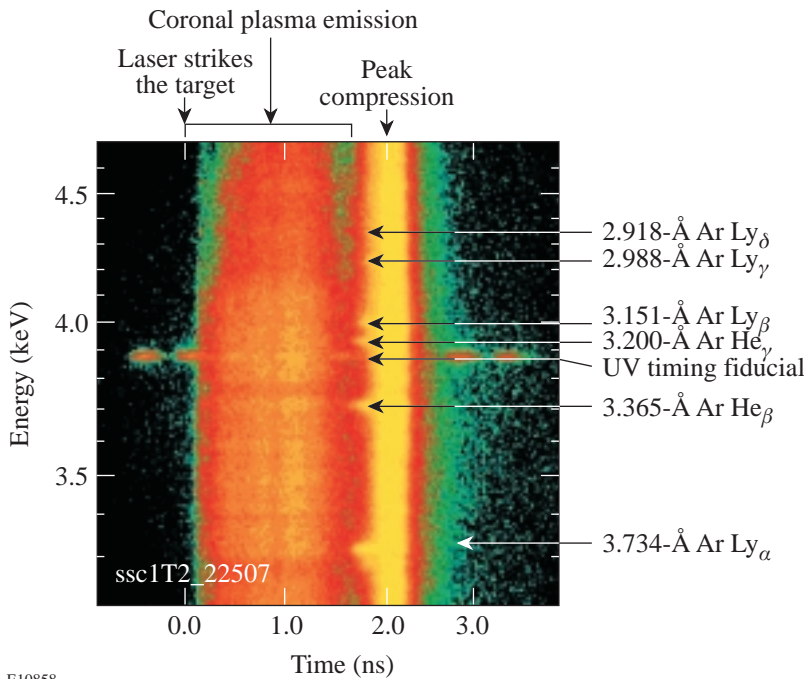


Figure 86.3  
The time-resolved Ar *K*-shell spectral measurement with an ~4-ns temporal window for shot number 22507 with temporal streak distortions removed. The entire evolution of the x-ray emission from the start of the coronal plasma emission when the laser strikes the target to the peak x-ray production at peak compression is recorded. The time axis was established with the temporally modulated ultraviolet fiducial laser pulse, and the exponential rise of the coronal plasma emission was extrapolated back to the beginning of the laser pulse.

E10858

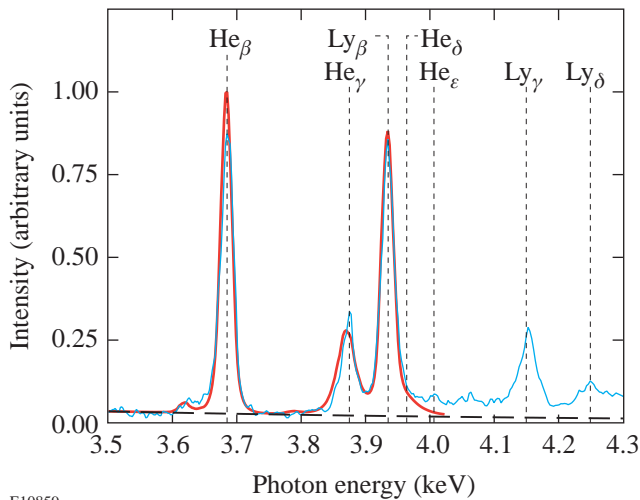
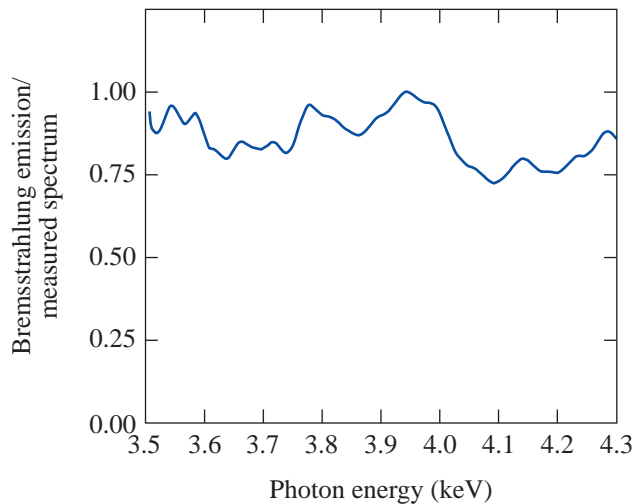


Figure 86.4  
The measured spectrum (blue curve) observed just after the onset of the Ar *K*-shell emission lines at  $t = 1.77$  ns is used to establish the photon-energy scale. The inferred electron density and temperature from the modeled spectrum for the 3.5- to 4.0-keV range (red curve) are  $0.3 (\pm 0.03) \times 10^{24} \text{ cm}^{-3}$  and  $1.3 (\pm 0.07) \text{ keV}$ . The background bremsstrahlung emission spectrum is represented by the dashed curve. The vertical dotted lines represent the unshifted line centers of the Ar *K*-shell resonance lines. At present only the 3.5- to 4.0-keV range is analyzed; however, work is in progress for the spectrum above 4.0 keV, which is more challenging to model due to the presence of the He-like and H-like bound-free edges.

E10859



E10860

Figure 86.5

The photometric calibration of the streaked spectra to correct for variations in x-ray spectral sensitivity and streak camera flat-fielding effects is determined by recording continuum emission from an implosion with no Ar-dopant simultaneously on the time-resolved and time-integrated instruments. The measured time-integrated spectrum was modeled with a bremsstrahlung emission spectrum characteristic of an electron temperature equal to 0.68 keV. The time-resolved measurement was integrated in time and compared with the modeled spectrum. The ratio of the modeled emission to the measurement is the photometric calibration of the streaked measurement.

MERL utilizes the adjustable parameter exponential approximation (APEX)<sup>28</sup> for ion microfield calculation, the theory of Boercker, Iglesias, and Dufty (BID)<sup>29</sup> for the ion dynamics, and a quantum mechanical relaxation approximation for electron broadening.<sup>8</sup>

Ar *K*-shell spectra were calculated for many combinations of electron temperatures and densities. Collisional-radiative-equilibrium population distributions including 1380 levels (1 fully stripped, 25 H-like, 372 He-like, 918 Li-like, 28 Be-like, 15 B-like, 11 C-like, and 10 N-like) are solved using the CRETIN code.<sup>30</sup> The effects on the populations due to radiative transfer of the optically thick  $\text{Ly}_\alpha$  and  $\text{He}_\alpha(1s2l-1s^2)$  emissions are approximated using Mancini's escape factors.<sup>31</sup> The Stark-broadened Ar *K*-shell resonance lines and satellites are calculated with MERL,<sup>27</sup> and opacity broadening is calculated assuming uniform core conditions.

The best fit to the measured spectra in the 3.5- to 4.0-keV range is determined using a least squares fitting routine. A look-up table is generated for 4000 combinations of electron temperature and densities in the range of interest. For each time-resolved measurement, the bremsstrahlung emission in

the 3.5- to 4.0-keV range is fitted in the measured spectra and added to the modeled Ar *K*-shell spectra. Modeled spectra are convolved with the spectral resolution of the streaked measurement, which was determined using the narrow spectral features that are observed when the Ar *K*-shell lines initially light up. The fitting routine searches the look-up table for the best fit for each time-resolved spectrum. At present only the 3.5- to 4.0-keV range is analyzed; however, work is in progress for the spectrum above 4.0 keV, which is more challenging to model due to the presence of the He-like and H-like bound-free edges.

### Experimental Results and Analysis

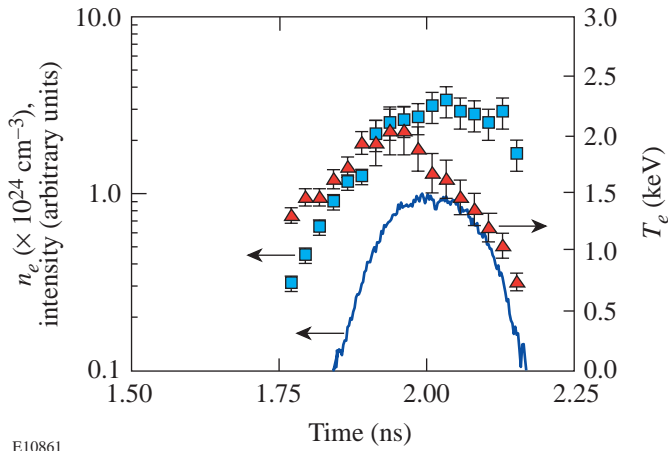
Significant changes in the Stark-broadened line widths and the relative ratios of the Ar *K*-shell emissions occur during the course of the implosion, making this diagnostic sensitive to the core electron temperature and density. A time history of emissivity-averaged core electron temperature (triangles) and density (squares) inferred from the time-resolved Ar *K*-shell spectroscopy is shown in Fig. 86.6. The measured x-ray continuum in the 3.50- to 3.55-keV range (blue line) is also shown for reference. An examination of Fig. 86.6 reveals the electron temperature peaks first, then the electron density peaks around the time of peak x-ray production. The electron temperature inferred from fitting the bremsstrahlung emission in the 3.5- to 4.0-keV spectral range slowly decreases with time from  $\sim 0.8$  keV at  $t = 1.77$  ns to  $\sim 0.5$  keV at 2.15 ns.

As pointed out earlier in the **Experimental Setup** section, the Ar *K*-shell emission lines at early times are used to establish the photon energy scale (see Fig. 86.4). The narrow spectral features that are measured (blue curve) in the 3.5- to 4.0-keV range are modeled (red curve) with the spectral line shapes characteristic of core conditions with electron density and temperature of  $0.3 (\pm 0.03) \times 10^{24} \text{ cm}^{-3}$  and 1.3 ( $\pm 0.07$ ) keV. The error analysis of the inferred electron temperature and density is given below. The level of continuum emission is also shown in Fig. 86.4 (dashed line), and the vertical dotted lines represent the unshifted line centers of the Ar *K*-shell resonance lines. Selected spectra from the hot, dense plasma are examined below.

The spectrum recorded at 1.89 ns is shown in Fig. 86.7 along with the modeled spectrum. The inferred electron density and temperature are  $1.25 (\pm 0.13) \times 10^{24} \text{ cm}^{-3}$  and 1.9 ( $\pm 0.1$ ) keV. Line shifts to lower photon energies<sup>10</sup> can be readily observed in the  $\text{He}_\beta$ ,  $\text{Ly}_\beta$ , and  $\text{Ly}_\gamma$  by comparing the measured profiles with the position of the unshifted lines. The atomic physics model shows good agreement with the mea-

sured line shifts, which are observed throughout the high-density portion of the implosion. Compared with Fig. 86.4, the  $\text{He}_\beta$  is now weaker than the  $\text{Ly}_\beta$ , and the level of continuum emission has increased.

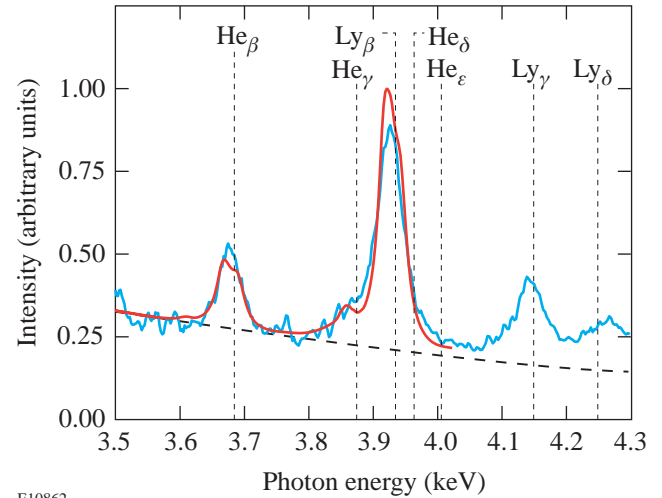
Simulations of the implosion with the 1-D hydrodynamic code *LILAC* indicate that the peak neutron production occurs at the same time as the peak emissivity-averaged electron temperature. Therefore, peak neutron production is assumed to be simultaneous with the peaking of the electron temperature at  $t = 1.93$ . The spectrum recorded at this time is shown in Fig. 86.8. The electron temperature and density at the time of peak neutron production are determined to be  $2.0 (\pm 0.2)$  keV and  $2.5 (\pm 0.5) \times 10^{24} \text{ cm}^{-3}$ . This represents the highest combination of electron temperature and density measured with Ar-doped deuterium gas fill capsules in laser-driven fusion. As the implosion proceeds to peak compression, which occurs at  $t = 2.01$  ns, the inferred electron density continues to increase to  $3.1 (\pm 0.6) \times 10^{24} \text{ cm}^{-3}$ , while the electron temperature decreases to  $1.7 (\pm 0.17)$  keV. The spectrum measured at peak compression is shown in Fig. 86.9. As can be seen in Figs. 86.8 and 86.9, the background bremsstrahlung emission is comparable with the  $\text{Ly}_\beta$  intensity and is stronger than the  $\text{He}_\beta$



E10861

Figure 86.6

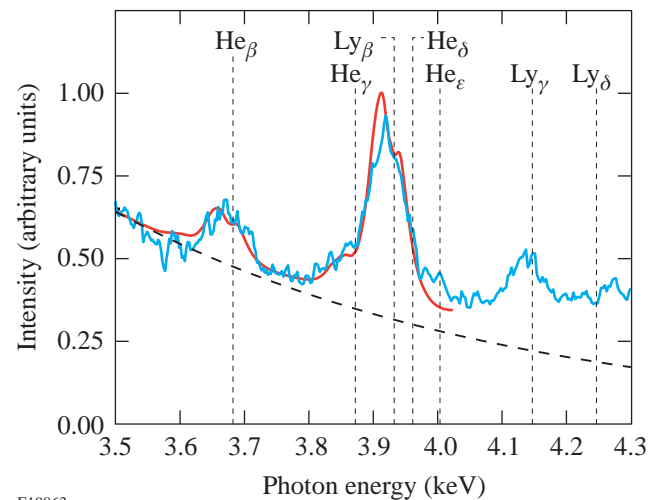
The time history of the emissivity-averaged core electron temperature (triangles) and density (squares) inferred from the time-resolved Ar *K*-shell spectroscopy for shot number 22507 reveals that the electron temperature peaks first, then the electron density peaks around the time the x-ray continuum in the 3.50- to 3.55-keV range (blue line) peaks. As the imploding shell decelerates, the emissivity-averaged electron temperature and density increase to  $2.0 (\pm 0.2)$  keV and  $2.5 (\pm 0.5) \times 10^{24} \text{ cm}^{-3}$  at peak neutron production ( $t = 1.93$  ns), which is assumed to be simultaneous with the peaking of the electron temperature. This is followed by a further increase in the electron density to  $3.1 (\pm 0.6) \times 10^{24} \text{ cm}^{-3}$  and a decrease in the electron temperature to  $1.7 (\pm 0.17)$  keV at peak compression ( $t = 2.01$  ns).



E10862

Figure 86.7

The measured spectrum (blue curve) observed at  $t = 1.89$  ns and the modeled spectrum (red curve) in the 3.5- to 4.0-keV range are presented. The inferred electron density and temperature are  $1.25 (\pm 0.13) \times 10^{24} \text{ cm}^{-3}$  and  $1.9 (\pm 0.1)$  keV. The background bremsstrahlung emission spectrum is represented by the dashed curve, and the unshifted line centers of the Ar *K*-shell resonance lines are represented by the vertical dotted lines. Line shifts are observed in the  $\text{He}_\beta$ ,  $\text{Ly}_\beta$ , and  $\text{Ly}_\gamma$  lines, and an increase in the linewidths is observed.



E10863

Figure 86.8

The measured spectrum (blue curve) observed at  $t = 1.93$  ns and the modeled spectrum (red curve) in the 3.5- to 4.0-keV range are presented. The background bremsstrahlung emission spectrum is represented by the dashed curve, and the unshifted line centers of the Ar *K*-shell resonance lines are represented by vertical dotted lines. The inferred electron temperature and density are  $2.0 (\pm 0.2)$  keV and  $2.5 (\pm 0.5) \times 10^{24} \text{ cm}^{-3}$ . The peak neutron production is estimated to occur at this time with the peaking of the electron temperature.

intensity. Finally, as the compressed core disassembles, the electron temperature and density rapidly decrease. The spectrum recorded at  $t = 2.15$  ns is shown in Fig. 86.10. The inferred electron density and temperature are  $1.7 (\pm 0.3) \times 10^{24} \text{ cm}^{-3}$  and  $0.75 (\pm 0.08)$  keV. The dominant feature of the spectrum is the  $\text{He}_\beta$  and its Li-like satellites around 3.55 to 3.75 keV.

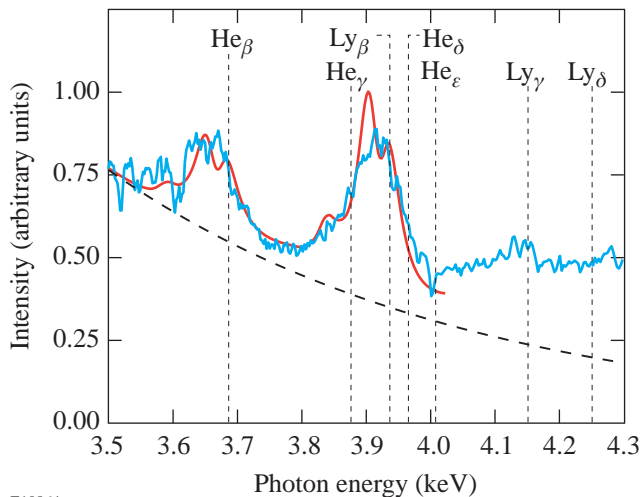
Many factors affect the accuracy of the electron temperature and density measurements. In this experiment strong signals of the spectral lines of interest were recorded throughout the implosion; therefore, the most influential factors affecting the accuracy are the determination of the background bremsstrahlung emission spectrum and the accuracy of the atomic physics model. As shown in the time-resolved spectra, the Stark-broadened spectral lines have a significant continuum emission background, which must be accounted for in the spectral line fitting procedure. Although the spectral fits examined here show good agreement with the measured line shapes and with the background levels between the spectral lines, there is some discrepancy between the measured and modeled line shapes at the peaks of the lines. The accuracy in the electron density is estimated to be  $\pm 10\%$ , and the accuracy in the electron temperature is estimated to be  $\pm 5\%$  for the range of electron densities below  $2 \times 10^{24} \text{ cm}^{-3}$ . Above this density

the accuracy in the electron density is estimated to be  $\pm 20\%$ , and the accuracy in the electron temperature is estimated to be  $\pm 10\%$ . The precision of the least squares spectral line fitting routine is well within the accuracy error.

Work is in progress to compare time-resolved Ar  $K$ -shell spectroscopy measurements with the time-resolved neutron burn history to establish the timing between the peak neutron burn and peak x-ray production. Comparisons will be made between fuel- $\rho R$  measurements, gated x-ray images of the core, and the emissivity-averaged core electron density measurement to estimate the amount of mix in the core of shell material with the fuel. In addition, lower dopant levels of Ar were studied to minimize the impact of the enhanced radiative losses on the target performance, while maintaining detectable signals of the Ar  $K$ -shell emission. These results will be presented in a separate publication for a range of targets with predicted convergence ratios from 13 to 37.

## Conclusion

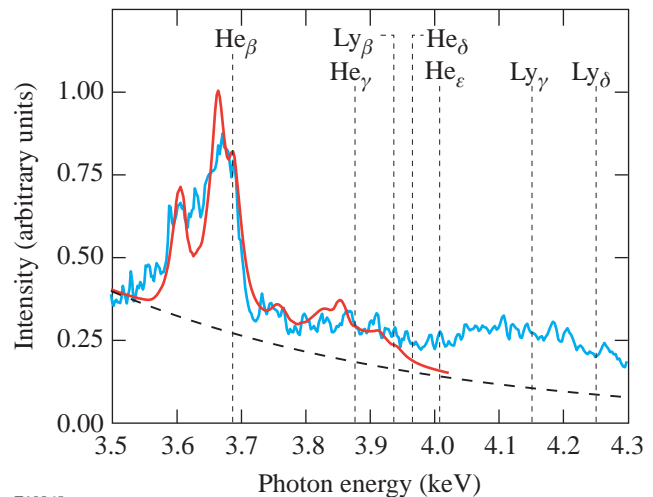
Time-resolved Ar  $K$ -shell spectroscopy has been used to diagnose the core conditions of direct-drive implosions on the 60-beam OMEGA laser system. Plastic shells with an Ar-doped deuterium fill gas were driven with a 23-kJ, 1-ns square laser pulse with a predicted convergence ratio of  $\sim 15$ , and laser



E10864

Figure 86.9

The measured spectrum (blue curve) observed at  $t = 2.01$  ns and the modeled spectrum (red curve) in the 3.5- to 4.0-keV range are presented. The background bremsstrahlung emission spectrum is represented by the dashed curve, and the unshifted line centers of the Ar  $K$ -shell resonance lines are represented by the vertical dotted lines. Peak compression occurs at this time, and the inferred electron temperature and density are  $1.7 (\pm 0.17)$  keV and  $3.1 (\pm 0.6) \times 10^{24} \text{ cm}^{-3}$ .



E10865

Figure 86.10

The measured spectrum (blue curve) observed at  $t = 2.15$  ns and the modeled spectrum (red curve) in the 3.5- to 4.0-keV range are presented. The background bremsstrahlung emission spectrum is represented by the dashed curve, and the unshifted line centers of the Ar  $K$ -shell resonance lines are represented by the vertical dotted lines. The compressed core is disassembling, and the inferred electron temperature and density rapidly decrease to  $0.75 (\pm 0.08)$  keV and  $1.7 (\pm 0.3) \times 10^{24} \text{ cm}^{-3}$ .

beams were smoothed with 1-THz SSD and polarization smoothing using birefringent wedges. The measured time-dependent, Stark-broadened, Ar *K*-shell spectral line shapes were compared with modeled spectra to infer the emissivity-averaged core electron temperature and density. As the imploding shell decelerates, the emissivity-averaged electron temperature and density increase to 2.0 ( $\pm 0.2$ ) keV and 2.5 ( $\pm 0.5$ )  $\times 10^{24}$  cm $^{-3}$  at peak neutron production, which is assumed to occur at the time of the peak emissivity-averaged electron temperature. This is followed by a further increase in the electron density to 3.1 ( $\pm 0.6$ )  $\times 10^{24}$  cm $^{-3}$  and a decrease in the electron temperature to 1.7 ( $\pm 0.17$ ) keV at peak compression.

#### ACKNOWLEDGMENT

This work was supported by the U. S. Department of Energy Office of Inertial Confinement Fusion under Cooperative Agreement No. DE-FC03-92SF19460, the University of Rochester, and the New York State Energy Research and Development Authority. The support of DOE does not constitute an endorsement by DOE of the views expressed in this article.

#### REFERENCES

1. C. P. Verdon, *Bull. Am. Phys. Soc.* **38**, 2010 (1993).
2. S. E. Bodner, D. G. Colombant, J. H. Gardner, R. H. Lehmburg, S. P. Obenschain, L. Phillips, A. J. Schmitt, J. D. Sethian, R. L. McCrory, W. Seka, C. P. Verdon, J. P. Knauer, B. B. Afeyan, and H. T. Powell, *Phys. Plasmas* **5**, 1901 (1998).
3. B. Yaakobi, S. Skupsky, R. L. McCrory, C. F. Hooper, H. Deckman, P. Bourke, and J. M. Soures, *Phys. Rev. Lett.* **44**, 1072 (1980).
4. A. Hauer *et al.*, *Phys. Rev. A* **28**, 963 (1983).
5. C. F. Hooper, Jr., D. P. Kilcrease, R. C. Mancini, L. A. Woltz, D. K. Bradley, P. A. Jaanimagi, and M. C. Richardson, *Phys. Rev. Lett.* **63**, 267 (1989).
6. H. R. Griem, *Phys. Fluids B* **4**, 2346 (1992).
7. C. F. Hooper, Jr., R. C. Mancini, D. A. Haynes, Jr., and D. T. Garber, in *Elementary Processes in Dense Plasmas*, edited by S. Ichimaru and S. Ogata (Addison-Wesley, Reading, MA, 1995), pp. 403–414.
8. D. A. Haynes, Jr., D. T. Garber, C. F. Hooper, Jr., R. C. Mancini, Y. T. Lee, D. K. Bradley, J. Delettrez, R. Epstein, and P. A. Jaanimagi, *Phys. Rev. E* **53**, 1042 (1996).
9. D. K. Bradley, J. A. Delettrez, R. Epstein, R. P. J. Town, C. P. Verdon, B. Yaakobi, S. Regan, F. J. Marshall, T. R. Boehly, J. P. Knauer, D. D. Meyerhofer, V. A. Smalyuk, W. Seka, D. A. Haynes, Jr., M. Gunderson, G. Junkel, C. F. Hooper, Jr., P. M. Bell, T. J. Ognibene, and R. A. Lerche, *Phys. Plasmas* **5**, 1870 (1998).
10. G. C. Junkel *et al.*, *Phys. Rev. E* **62**, 5584 (2000).
11. B. A. Hammel *et al.*, *Phys. Rev. Lett.* **70**, 1263 (1993).
12. C. J. Keane *et al.*, *Phys. Fluids B* **5**, 3328 (1993).
13. B. A. Hammel *et al.*, *J. Quant. Spectrosc. Radiat. Transf.* **51**, 113 (1994).
14. H. Nishimura *et al.*, *Phys. Plasmas* **2**, 2063 (1995).
15. N. C. Woolsey *et al.*, *Phys. Rev. E* **56**, 2314 (1997).
16. N. C. Woolsey *et al.*, *Phys. Rev. E* **57**, 4650 (1998).
17. T. R. Boehly, D. L. Brown, R. S. Craxton, R. L. Keck, J. P. Knauer, J. H. Kelly, T. J. Kessler, S. A. Kumpan, S. J. Loucks, S. A. Letzring, F. J. Marshall, R. L. McCrory, S. F. B. Morse, W. Seka, J. M. Soures, and C. P. Verdon, *Opt. Commun.* **133**, 495 (1997).
18. T. J. Kessler, Y. Lin, J. J. Armstrong, and B. Velazquez, in *Laser Coherence Control: Technology and Applications*, edited by H. T. Powell and T. J. Kessler (SPIE, Bellingham, WA, 1993), Vol. 1870, pp. 95–104; Y. Lin, T. J. Kessler, and G. N. Lawrence, *Opt. Lett.* **21**, 1703 (1996).
19. S. Skupsky, R. W. Short, T. Kessler, R. S. Craxton, S. Letzring, and J. M. Soures, *J. Appl. Phys.* **66**, 3456 (1989).
20. S. Skupsky and R. S. Craxton, *Phys. Plasmas* **6**, 2157 (1999).
21. S. P. Regan, J. A. Marozas, J. H. Kelly, T. R. Boehly, W. R. Donaldson, P. A. Jaanimagi, R. L. Keck, T. J. Kessler, D. D. Meyerhofer, W. Seka, S. Skupsky, and V. A. Smalyuk, *J. Opt. Soc. Am. B* **17**, 1483 (2000).
22. T. R. Boehly, V. A. Smalyuk, D. D. Meyerhofer, J. P. Knauer, D. K. Bradley, R. S. Craxton, M. J. Guardalben, S. Skupsky, and T. J. Kessler, *J. Appl. Phys.* **85**, 3444 (1999).
23. T. R. Boehly, V. N. Goncharov, O. Gotchev, J. P. Knauer, D. D. Meyerhofer, D. Oron, S. P. Regan, Y. Srebro, W. Seka, D. Shvarts, S. Skupsky, and V. A. Smalyuk, *Phys. Plasmas* **8**, 2331 (2001).
24. D. D. Meyerhofer, J. A. Delettrez, R. Epstein, V. Yu. Glebov, V. N. Goncharov, R. L. Keck, R. L. McCrory, P. W. McKenty, F. J. Marshall, P. B. Radha, S. P. Regan, S. Roberts, W. Seka, S. Skupsky, V. A. Smalyuk, C. Sorce, C. Stoeckl, J. M. Soures, R. P. J. Town, B. Yaakobi, J. D. Zuegel, J. Frenje, C. K. Li, R. D. Petrasso, D. G. Hicks, F. H. Séguin, K. Fletcher, S. Padalino, M. R. Freeman, N. Izumi, R. Lerche, T. W. Phillips, and T. C. Sangster, *Phys. Plasmas* **8**, 2251 (2001).
25. D. H. Kalantar *et al.*, in *22nd International Congress on High-Speed Photography and Photonics*, edited by D. L. Paisley and A. M. Frank (SPIE, Bellingham, WA, 1997), Vol. 2869, pp. 680–685.
26. B. L. Henke, E. M. Gullikson, and J. C. Davis, *At. Data Nucl. Data Tables* **54**, 181 (1993).
27. R. C. Mancini *et al.*, *Comput. Phys. Commun.* **63**, 314 (1991).
28. C. A. Iglesias, J. L. Lebowitz, and D. MacGowan, *Phys. Rev. A* **28**, 1667 (1983).
29. D. B. Boercker, C. A. Iglesias, and J. W. Dufty, *Phys. Rev. A* **36**, 2254 (1987).
30. H. A. Scott and R. W. Mayle, *Appl. Phys. B* **B58**, 35 (1994).
31. R. C. Mancini, R. F. Joyce, and C. F. Hooper, Jr., *J. Phys. B: At. Mol. Phys.* **20**, 2975 (1987).

---

# Study of Direct-Drive, DT-Gas-Filled-Plastic-Capsule Implosions Using Nuclear Diagnostics on OMEGA

## Introduction

High-gain inertial confinement fusion (ICF) requires uniform compression of a spherical capsule to a state of high density and temperature;<sup>1–3</sup> current research is aimed at finding ways to achieve this goal. This article describes how a range of traditional and new nuclear diagnostics are used to study the compression performance of deuterium-tritium (DT)-filled target capsules imploded by direct laser drive on LLE’s 60-beam OMEGA laser system.<sup>4</sup> The sensitivity of the implosion performance to the uniformity of laser power deposition is studied by measuring the fuel and shell areal densities ( $\rho R$ ) and the shell electron temperature ( $T_e$ ). These parameters are studied using the first comprehensive set of separate spectral measurements of deuterons, tritons, and protons (“knock-ons”) elastically scattered from the fuel and shell by 14.1-MeV DT fusion neutrons.

To achieve fusion ignition, a DT-filled target needs sufficient compression to form two different regions: a small mass with low density but high temperature in the center (the “hot spot,” with  $T_i \sim 10$  keV) and a large mass of high-density, low-temperature fuel surrounding this hot spot. The 3.5-MeV DT alphas generated in the central hot spot (with  $\rho R \sim 0.3$  g/cm<sup>2</sup>) are stopped in the fuel, thereby propagating a thermonuclear burn. Two approaches to achieving this objective are indirect- and direct-drive implosions. For the indirect-drive approach, where laser beams irradiate the inner wall of a high-Z radiation case (hohlraum), laser energy is first converted to soft x rays, which subsequently compress the capsule. For the direct-drive approach, the laser beams directly irradiate and compress the target. The National Ignition Facility (NIF), which has both indirect- and direct-drive capabilities and is under construction at Lawrence Livermore National Laboratory, is designed to achieve this ignition objective. Experiments on OMEGA are currently investigating many aspects of the implosion physics relevant to future NIF experiments with scaled experimental conditions. For example, the OMEGA cryogenic program will study energy-scaled implosions based on NIF ignition target designs.<sup>5</sup>

OMEGA is a Nd-doped glass laser facility that can deliver 60 beams of frequency-tripled UV light (351 nm) with up to 30 kJ in 1 to 3 ns with a variety of pulse shapes; both direct and indirect drive are possible.<sup>4</sup> Early direct-drive experiments on OMEGA have achieved high temperatures ( $T_i \sim 15$  keV) and high fusion yields (for example, DT neutron yield  $\sim 10^{14}$  and DD neutron yield  $\sim 10^{12}$ ).<sup>6</sup> In particular, a series of implosions of room-temperature capsules with gas fill (0 to 30 atm of either D<sub>2</sub> or D<sup>3</sup>He) and plastic shells (CH, 10 to 35  $\mu$ m thick) have recently been conducted with a variety of laser pulse shapes, irradiation uniformities, etc.<sup>7–11</sup> These implosions generate typical fuel areal densities ( $\rho R_{\text{fuel}}$ ) of  $\sim 5$  to 15 mg/cm<sup>2</sup> and shell areal densities ( $\rho R_{\text{shell}}$ )  $> 50$  mg/cm<sup>2</sup>. Part of their importance lies in their relevance to OMEGA cryogenic-target implosions and the insights they provide into implosion physics of direct-drive ICF.

The OMEGA experiments included in this article involved room-temperature capsules with DT-gas fill and CH shells. The nominal parameters were 20- $\mu$ m shell thickness and 15-atm fill pressure. These types of capsules have total masses similar to those of OMEGA cryogenic targets and are expected to have comparable stability properties under similar experimental conditions.<sup>5,7</sup> An OMEGA cryogenic capsule consists of three parts: a central part with low-pressure (triple-point vapor pressure) D<sub>2</sub> or DT gas (0.2 atm at  $\sim 19$  K), a main fuel layer ( $\sim 90$   $\mu$ m of D<sub>2</sub> or DT ice), and a 1- to 3- $\mu$ m CH overcoat. The CH shell of a room-temperature target simulates the fuel part (DT ice) of a cryogenic target, and the fill gas simulates the hot-spot-forming central DT gas in a cryogenic target.<sup>5</sup> The hydrodynamics are expected to differ in detail, in part due to the difference in the equation of state, ablation rate, and implosion velocity. Nevertheless, many aspects of high-energy-density physics and the target performances of cryogenic targets can be studied with these surrogate targets under current experimental conditions, including the effects of irradiation uniformity. The experiments also provide useful data for the development of advanced diagnostics (such as high-resolution, charged-particle spectroscopy<sup>12</sup>) and for benchmarking computer simulations.<sup>13</sup>

A primary emphasis in this study was the dependence of capsule performance on laser irradiation uniformity; the next section provides motivation by describing the importance of irradiation uniformity to the physics of capsule implosion performance. Subsequent sections (1) describe the experiments under study here, utilizing DT-filled capsules with CH shells and different laser-smoothing techniques; (2) discuss the measurement of knock-on spectra and the relationships between these measurements and the characteristics of imploded capsules; and (3) discuss the performance of imploded core and shell under different conditions, showing that 15-atm-DT capsules with appropriate laser smoothing achieved a moderate convergence ratio ( $Cr \sim 12$  to  $15$ );  $\rho R_{\text{fuel}}$  and  $\rho R_{\text{shell}}$  were determined to be  $\sim 15$  mg/cm<sup>2</sup> and  $\sim 60$  mg/cm<sup>2</sup>, respectively.

### Laser Drive Characteristics and Capsule Performance

Successful direct-drive implosions require control of Rayleigh–Taylor (RT) instability because direct-drive targets are susceptible to this instability during both acceleration and deceleration phases.<sup>5,7</sup> This control requires shell integrity throughout the whole acceleration phase, which can be accomplished by a spherical target being irradiated uniformly. The instability is seeded by laser illumination nonuniformity and also by target imperfections (roughness on the outer ablative surface and/or the inner fuel–shell interface).<sup>7</sup> During the acceleration phase, this instability can occur at the ablation surface and propagate to the fuel–shell interface, adding roughness to the inner shell surface and also feeding back out to the ablation surface; in the worst case, this could lead to shell breakup. During the deceleration phase, the distortions at the fuel–shell interface grow and result in the mixing of fuel and shell materials, which degrades target performance.

For the shots studied here, two approaches were used to control instabilities and improve target performance. The first was the choice of laser pulse shape. A high-shock-strength (high adiabat), 1-ns square laser pulse was used to maximize the ablation rate and reduce RT growth. Though a gradually rising pulse (low adiabat) produces, in principle, a larger target compression than a sharply rising pulse, because of lower fuel and shell isentropes,<sup>1,2</sup> a low-shock-strength pulse generates a lower ablation rate and smaller in-flight shell thickness, leading to more instability for direct-drive implosions. This has been demonstrated in earlier experiments, where better target performance was obtained with a 1-ns square pulse than with other pulse types for room-temperature targets.<sup>8,9</sup> Simulations have predicted that another advantage to using the 1-ns square pulse to implode room-temperature capsules with 20- $\mu\text{m}$ -CH shells is that the target hydrodynamic and stability properties

are similar to those that result from using a shaped pulse with cryogenic targets (for example, the OMEGA  $\alpha = 3$  design<sup>7</sup>).

The second approach is improved laser-irradiation uniformity. In discussing deviations from illumination uniformity, we distinguish two sources: Beam-to-beam energy imbalance causes low-order mode perturbations (mode number  $\ell < 10$ ), while nonuniformities within individual beams generate higher-order perturbations ( $\ell > 10$ ). To achieve a level of 1% or less for on-target irradiation nonuniformity, different beam energies must be matched to within an rms deviation of 5%.<sup>5,7</sup> In the series of implosions studied here, an energy balance within 3% to 25% rms was achieved; however, after taking into account the effect of the laser-beam overlap on the target surface (as shown in Fig. 86.11), low-mode rms uniformity was between 1% and 9%, with an average  $\leq 5\%$ .

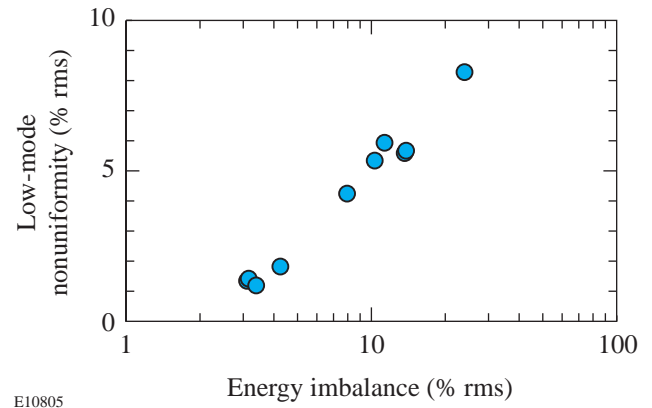


Figure 86.11

The low-mode rms irradiation nonuniformity plotted as a function of the beam energy imbalance. In general, a better energy balance results in better low-mode rms irradiation uniformity.

Single-beam uniformity is improved by two-dimensional smoothing by spectral dispersion (2-D SSD) combined with other smoothing techniques such as distributed phase plates (DPP's) and distributed polarization smoothing (PS).<sup>7</sup> The two smoothing conditions used in this study were 0.35-THz-bandwidth, 3-color-cycle 2-D SSD and 1.0-THz-bandwidth, single-color-cycle 2-D SSD with PS. Theoretical simulations and recent experiments have demonstrated that PS improves irradiation uniformity by a factor of  $\sim \sqrt{2}$  for higher-order perturbations ( $\ell > 10$ ). The combination of PS with high-bandwidth 2-D SSD is expected to result in on-target nonuniformity  $< 1\%$  after 300 ps.<sup>5,7,14</sup>

## Experiments

The OMEGA experiments reported here used 60 beams of frequency-tripled (351-nm) UV light to directly drive the targets. Targets were room-temperature capsules with DT gas enclosed in a CH shell. The actual DT-gas pressure was in the range of 11 to 15 atm. The CH-shell thickness was 19 to 20  $\mu\text{m}$ , and the capsule diameters were 920 to 960  $\mu\text{m}$ . Laser energy ranged from 20 to 23 kJ, with a typical intensity of  $\sim 1 \times 10^{15}$  W/cm<sup>2</sup>, and the laser-beam spot size on target was  $\sim 1$  mm. The laser pulse was approximately square with a 1-ns duration, with rise and decay times of  $\sim 150$  ps. Good pulse-shape repeatability was obtained, and the beam-to-beam laser energy balance was typically  $\sim 5\%$  rms. Two laser configurations were used. In the first, individual beams were smoothed using 3-color-cycle 2-D SSD along two axes with a bandwidth of 0.35 THz. In the second, beams were smoothed by single-color-cycle 2-D SSD, with a 1.0-THz bandwidth, and PS using a birefringent wedge.

The primary DT neutron yields were measured using Cu activation.<sup>15</sup> For this series of experiments, primary DT neutron yields of  $10^{12}$  to  $10^{13}$  were obtained, with an estimated measurement error of  $\sim 10\%$ . Ion temperatures  $T_i$  were measured using neutron time-of-flight (NTOF) Doppler widths.<sup>16–18</sup> Typical values were 3.5 to 5 keV, with a measurement error of  $\sim 0.5$  keV. Fusion burn history was obtained with the neutron temporal detector (NTD),<sup>19</sup> and the typical fusion burn durations here were 140 to 190 ps with bang times occurring at several hundred picoseconds after the end of the laser pulse.

To obtain the areal densities for compressed fuel and shell (a fundamental measure of the implosion dynamics and quality), and to address other issues (such as the measurement of shell  $T_e$ , electrostatic potential due to capsule charging, etc.), spectra of emerging charged particles were measured with two magnet-based charged-particle spectrometers (CPS-1 and CPS-2)<sup>20,21</sup> and several “wedge-range-filter (WRF)” spectrometers.<sup>11,22</sup> The charged particles [knock-on deuterons (KOD), tritons (KOT), and protons (KOP)] are elastically scattered from the fuel and shell by 14.1-MeV DT neutrons.<sup>23,24</sup> This is currently the only technique for studying the fuel and shell areal densities of DT capsule implosions on OMEGA. Other possible methods include neutron activation<sup>25</sup> and measurement of secondary<sup>26,27</sup> and tertiary products (neutrons and protons<sup>27–29</sup>), but these methods are currently impractical because of certain technical limitations.

CPS-1 and CPS-2 are nearly identical, and each uses a 7.6-kG permanent magnet<sup>20,21</sup> constructed of a neodymium-iron-boron alloy with a steel yoke. Incoming particles are collimated by a slit whose width can be varied between 1 and 10 mm (giving an acceptance of  $10^{-6}$  to  $10^{-5}$  of the total yield), as appropriate for expected flux levels. The magnet separates particles into different trajectories according to the ratio of momentum to charge. Pieces of CR-39, used as particle detectors, are positioned throughout the dispersed beam normal to the particle flux. Both the energy and the species of the particle generating a track in CR-39 can be determined through the combined knowledge of its trajectory (determined by its position on the CR-39) and the track diameter. Particles with the same gyro radius, such as 8-MeV tritons and 12-MeV deuterons, are easily distinguished since their very different stopping powers generate measurably different track sizes in the CR-39 (the larger the stopping power, the larger the track). This configuration allows coverage over the proton energy range from 0.1 MeV to 40 MeV. The energy calibration uncertainty varies with particle energy, being about 30 keV at 2 MeV and about 100 keV at 15 MeV. The two spectrometers are  $101^\circ$  apart, thereby enabling studies of implosion symmetry. CPS-2 (CPS-1) is placed inside (outside) the 165-cm-radius OMEGA chamber at 100 cm (235 cm) from the target.

The WRF spectrometers, which are described in detail elsewhere,<sup>11,22</sup> provide proton spectra by analyzing the distributions of proton-track diameters in a piece of CR-39 that is covered during exposure by an aluminum ranging filter with continuously varying thickness. The current energy calibration is accurate to about 0.15 MeV at 15 MeV. These spectrometers are simple and compact, allowing them to be used at multiple positions during a shot for symmetry studies and placed close to the target for good statistics when proton yields are low (down to about  $5 \times 10^5$ ).

To analyze the measurements made during these experiments, the implosions were modeled with the one-dimensional hydrodynamic calculation code *LILAC*.<sup>30</sup> Several important physical models were used in the calculation, such as the tabulated equation of state (*SESAME*), flux-limited electron transport (with a flux limiter of  $f=0.06$ ), local thermodynamic equilibrium (LTE), opacities for multigroup radiation transport, and inverse-bremsstrahlung-absorption energy deposition through a ray-trace algorithm in the underdense plasma. No effect of fuel-shell mix was included.

### Knock-on Particles and Their Spectra

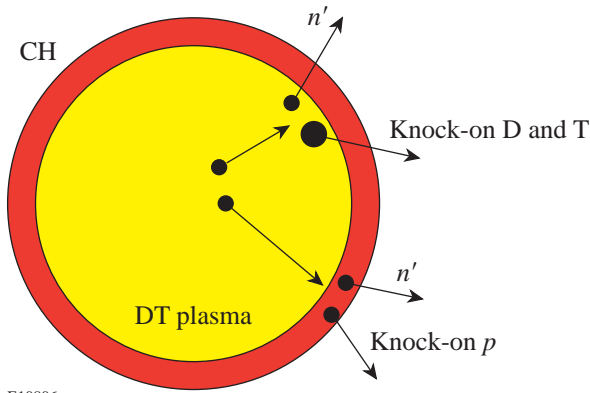
Knock-on particles are generated in a two-step process. A 14.1-MeV neutron is first generated from a DT fusion reaction. These neutrons usually escape the capsule without interacting. A small fraction of them (of the order of  $\sim 0.1\%$ ), however, elastically scatter off either fuel D or T or CH-shell  $p$ , as described in Eqs. (1)–(4) and depicted schematically in Fig. 86.12. Information about the compressed fuel is carried out by these knock-on D and T; information about the compressed shell is carried out by knock-on  $p$  and is also contained in the energy downshifts of knock-on D and T spectra:

$$D + T \rightarrow \alpha(3.5 \text{ MeV}) + n(14.1 \text{ MeV}), \quad (1)$$

$$n(14.1 \text{ MeV}) + T \rightarrow n' + T(\leq 10.6 \text{ MeV}), \quad (2)$$

$$n(14.1 \text{ MeV}) + D \rightarrow n' + D(\leq 12.5 \text{ MeV}), \quad (3)$$

$$n(14.1 \text{ MeV}) + p \rightarrow n' + p(\leq 14.1 \text{ MeV}). \quad (4)$$



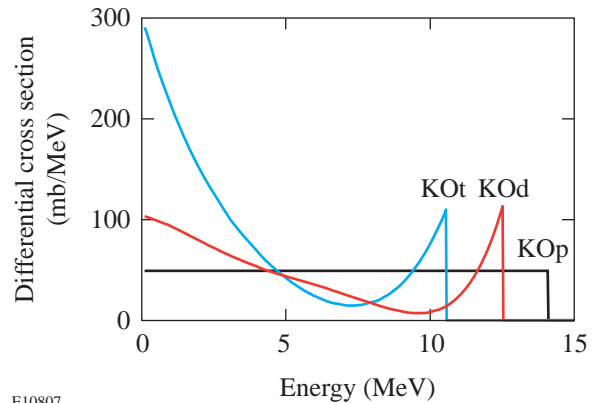
E10806

Figure 86.12

A schematic illustration of the knock-on processes in an imploded capsule. The central fuel part typically has an initial radius of 450 to 475  $\mu\text{m}$  and a DT-gas fill of 15 atm. The initial shell layer is constructed of CH with a thickness of 19.5 to 20  $\mu\text{m}$ . Primary 14.1-MeV DT neutrons, generated in the fuel, elastically scatter deuterons (KOd) and tritons (KOt) out of the fuel and protons (KOp) out of the shell. Consequently, information from the compressed core is carried out by these knock-on deuterons and tritons, and information from the compressed shell is carried out by knock-on protons. The energy downshifts of knock-on D and T spectra also contain information about the shell.

Figure 86.13 illustrates the differential cross sections of knock-on processes. When the collisions are head-on, the characteristic end-point energy for T (D) [ $p$ ] is 10.6 MeV (12.5 MeV) [14.1 MeV]. The well-defined, high-energy peak for a knock-on deuteron (triton) spectrum represents about 15.7% (13.5%) of the total cross section and corresponds to an energy region of 9.6 to 12.5 MeV (7.3 to 10.6 MeV). For a model-independent determination of  $\rho R_{\text{fuel}}$ , the knock-on diagnostic usually uses only these high-energy peaks. For knock-on protons, the cross section is virtually flat from 0 to 14.1 MeV because the neutron and proton masses are nearly identical. Because of a possible time-dependent distortion occurring in the low-energy region, however, only the flat region is used here. Two important parameters for this diagnostic are the number of knock-on particles and the downshifts of the knock-on spectra. The knock-on numbers provide information about the  $\rho R$  of the layer (core or shell) in which they are produced, and the energy loss of these particles provides additional information about the  $\rho R$  traversed.

It has been shown that, for a hot-spot model of the compressed fuel (where all primary neutrons are produced in an infinitesimal, high-temperature region at the center of a uniform-density DT plasma),  $\rho R_{\text{fuel}}$  is related to the knock-on



E10807

Figure 86.13

Differential cross sections for elastic scattering of 14.1-MeV neutrons on deuterons, tritons, and protons, where the energy is the scattered ion energy. When these collisions are head-on, the characteristic end-point (maximum) energy for T (D) [ $p$ ] is 10.6 MeV (12.5 MeV) [14.1 MeV]. The high-energy peak for knock-on deuterons (tritons) contains about 15.7% (13.5%) of the total cross section, which corresponds to an energy region of 9.6 to 12.5 MeV (7.3 to 10.6 MeV). [For deuterons and tritons, the integral under the high-energy peak gives an effective cross section that is used in Eq. (5)]. For knock-on protons, the cross section is flat from 0 to 14.1 MeV, and an integral over a 1-MeV interval gives an effective cross section that is used in Fig. 86.14.

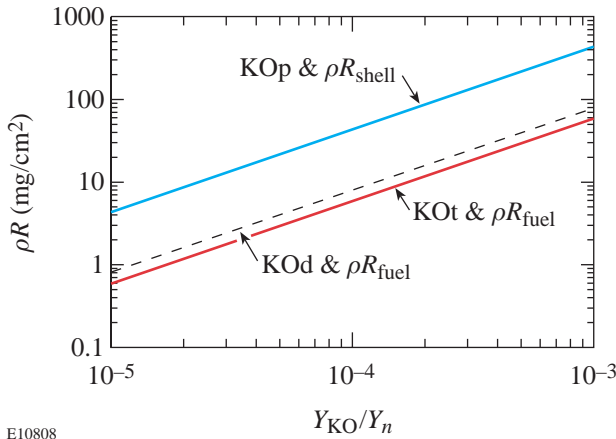
yield by the equation<sup>23,24</sup>

$$\rho R_{\text{fuel}} = \frac{(2\gamma + 3)m_p}{(\gamma\sigma_d^{\text{eff}} + \sigma_t^{\text{eff}})} \frac{Y_{\text{KOd}} + Y_{\text{KOt}}}{Y_n}, \quad (5)$$

where  $Y_n$  is the measured primary neutron yield,  $Y_{\text{KOd}}$  and  $Y_{\text{KOt}}$  are deuteron and triton knock-on yields under the high-energy peak of their spectra (see Fig. 86.13);  $\sigma_t^{\text{eff}}$  ( $\sigma_d^{\text{eff}}$ ) is the effective cross-section of knock-on triton (deuteron) as defined in Fig. 86.13;  $m_p$  is the proton mass; and  $\gamma = n_d/n_t$ . Similarly, the yield of knock-on protons, which are exclusively generated in the CH shell, can be shown to be related to  $\rho R_{\text{shell}}$  by the equation

$$\rho R_{\text{shell}} = \frac{(\gamma + 12)m_p}{\gamma\sigma_p^{\text{eff}}} \frac{Y_{\text{KO}p}}{Y_n}, \quad (6)$$

where  $Y_{\text{KO}p}$  is the measured knock-on- $p$  yield in a 1-MeV range (see Fig. 86.13);  $\sigma_p^{\text{eff}}$  is an effective cross section for knock-on protons; and  $\gamma = n_H/n_C$  (where  $n_H$  and  $n_C$  are the number densities of the hydrogen and carbon atoms, respectively, in the shell). Under some circumstances, it is useful to modify Eq. (5) for use with the “uniform” model, in which primary neutrons are generated throughout the volume containing deuterons and tritons, by multiplying the right-hand side by a factor of 1.33. Figure 86.14 displays inferred values



E10808

Figure 86.14

Areal density versus the ratio of knock-on particle yield to primary neutron yield. For knock-on D and T, a hot-spot model is assumed and the yields under the high-energy peaks are used (as described in Fig. 86.13’s caption). For knock-on  $p$ , a hot-spot model is assumed and the yield per MeV in the flat region is used.

of  $\rho R$  as a function of the measured ratios of knock-on yield to primary neutron yield. The model-independent use of Eq. (5) breaks down when the total areal density exceeds about 100 mg/cm<sup>2</sup> because the knock-on spectra become sufficiently distorted by slowing-down effects that measurements can become ambiguous; the accurate determination of  $\rho R_{\text{fuel}}$  will then have to rely on the guidance of model-dependent simulations.

The potential importance of knock-on particle measurements was realized some years ago, and measurements with both limited spectral resolution and a small number of knock-on particles (around 30) were subsequently obtained.<sup>23,24</sup> Those measurements relied on range-filter data in the form of “coincident” (front-side and back-side) tracks generated in a CR-39 nuclear track detector or in nuclear emulsions. This early work relied on detailed assumptions about the spectra of knock-on particles, which were estimated in indirect ways from other diagnostic data (for example, from the downshifted D<sup>3</sup>He protons).<sup>23</sup> In contrast, charged-particle spectroscopy, as described here, measures the whole spectrum directly for each particle. With hundreds to thousands of knock-on particles being simultaneously detected from an individual implosion, comprehensive and high-resolution knock-on spectra are readily obtained.

Figure 86.15 shows sample spectra obtained by CPS-2 for shot 20231. For this shot, the capsule was filled with 12.3 atm of DT gas and had a 19.1- $\mu\text{m}$ -thick CH shell. The laser energy was 22.1 kJ, and the primary neutron yield was  $7.1(\pm 0.7) \times 10^{12}$ . The bandwidth of the 2-D SSD was 0.35 THz, and no polarization smoothing (PS) was applied. The beam-to-beam energy balance was 13.7% rms, and the on-target, low-mode rms uniformity was 5.6% because of beam overlap on the target surface. An ion temperature of  $T_i \cong 4.0(\pm 0.5)$  keV was obtained. The fusion burn occurred at  $1810(\pm 50)$  ps and lasted for  $180(\pm 25)$  ps. Figure 86.15(a) provides the knock-on T spectrum with a yield of about  $5.7 \times 10^8$  tritons under the high-energy peak (between 3 to 10 MeV). The whole spectrum is downshifted by  $\sim 4$  MeV (as described in the figure caption). Figure 86.15(b) shows the knock-on D spectrum with a yield of about  $4.8 \times 10^8$  deuterons under the high-energy peak (between 3.5 to 12 MeV). An energy loss of about  $\sim 3$  MeV, relative to the birth spectrum, is measured. Figure 86.15(c) displays the knock-on  $p$  spectrum, with a yield of about  $5.7 \times 10^8/\text{MeV}$  protons in the flat region between 8 to 12 MeV. The end point of this spectrum is about 14 MeV because protons scattered from the outer part of the shell lose no energy. We note that CPS yield measurements represent an integral over

the fusion burn duration, so an inferred  $\rho R$  value represents an average over the burn. In addition, the fact that the source of neutrons is distributed over a finite volume of fuel means that inferred  $\rho R$  values represent spatial averages.

The measured knock-on spectra for shot 20698 are shown in Fig. 86.16. The capsule was filled with 15 atm of DT gas and had a 20- $\mu\text{m}$  CH shell. The laser energy was 23.8 kJ, and the primary neutron yield was  $1.4(\pm 0.1) \times 10^{13}$ . In contrast to shot 20231, polarization smoothing was applied for this shot and the 2-D SSD bandwidth was increased to 1.0 THz. The beam-

to-beam energy balance (3.1% rms) and the on-target low-mode rms uniformity (1.3% rms) were thus improved. An ion temperature of  $T_i \cong 4.1(\pm 0.5)$  keV was obtained. The fusion burn occurred at  $1750(\pm 50)$  ps and lasted for  $170(\pm 25)$  ps. Figure 86.16(a) shows the knock-on T spectrum, with a yield of about  $1.2 \times 10^9$  tritons under the high-energy peak (between 2.5 to 10 MeV). The whole spectrum is downshifted by 4.8 MeV. Figure 86.16(b) shows the knock-on D spectrum, with a yield of about  $1.7 \times 10^9$  deuterons under the high-energy peak (between 3.5 to 12 MeV). An energy loss of about 4.1 MeV is measured. Figure 86.16(c) shows the knock-on  $p$

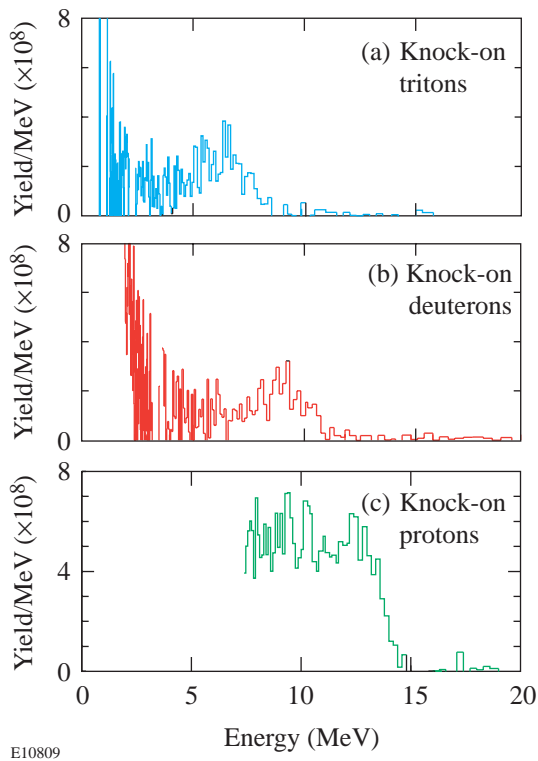


Figure 86.15  
Knock-on spectra measured by CPS-2 for shot 20231. The capsule was filled with 12.3 atm of DT gas and had a 19.1- $\mu\text{m}$ -thick CH shell. The laser energy was 22.1 kJ, and the primary neutron yield was  $7.1 \times 10^{12}$ . The bandwidth of 2-D SSD was 0.35 THz, and no PS was applied. (a) The knock-on T spectrum with a yield of about  $5.7 \times 10^8$  tritons under the high-energy peak (between 3 to 10 MeV). The whole spectrum is downshifted by  $\sim 4$  MeV (determined by the energy at which the yield/MeV reaches half of its peak value on the high-energy end of the spectrum). (b) The knock-on D spectrum with a yield of about  $4.8 \times 10^8$  deuterons under the high-energy peak (between 3.5 to 12 MeV). An energy loss of about  $\sim 3$  MeV is measured. (c) The knock-on  $p$  spectrum with a yield/MeV of about  $5.7 \times 10^8/\text{MeV}$  protons in the flat region between 8 to 12 MeV. The end point of this spectrum is about 14 MeV, reflecting the fact that particles scattered from the outer part of the shell have no energy loss.

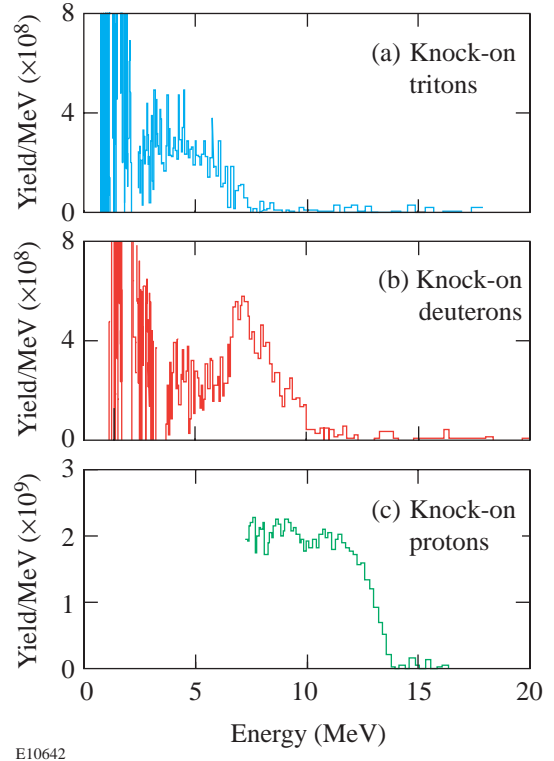


Figure 86.16  
Knock-on spectra for shot 20698, measured by CPS-2. The capsule is filled with 15 atm of DT gas and has a 20- $\mu\text{m}$  CH shell. For this shot, the laser energy was 23.8 kJ, and the primary neutron yield was  $1.4 \times 10^{13}$ . The 2-D SSD bandwidth was 1.0 THz, and polarization smoothing was applied. (a) The knock-on T spectrum, with a yield of about  $1.2 \times 10^9$  tritons under the high-energy peak (between 2.5 to 10 MeV). The whole spectrum is downshifted by 4.8 MeV. (b) The knock-on D spectrum, with a yield of about  $1.7 \times 10^9$  deuterons under the high-energy peak (between 3.5 to 12 MeV). An energy loss of about 4.1 MeV is measured. (c) The knock-on  $p$  spectrum, with a yield of about  $2.0 \times 10^9/\text{MeV}$  protons in the flat region between 8 to 12 MeV. As in Fig. 86.15, the end point of this spectrum is about 14 MeV, reflecting the fact that particles scattered from the outer part of the shell have no energy loss.

spectrum, with a yield of about  $2.0 \times 10^9$ /MeV in the flat region between 8 to 12 MeV. The end point of this spectrum is about 14 MeV, as for shot 20231. Relative to shot 20231, the primary neutron yield in shot 20698 is higher by a factor of  $\approx 1.95$ , and the knock-on particle yields are higher by factors of  $\approx 3.48$  (deuteron) and  $\approx 3.45$  (proton). In addition, because of increased compression, the energy loss of the knock-on particles from the fuel is greater by 15% to 30%.

## Results and Discussions

### 1. Core Performance of Moderate-Convergence Capsule Implosions

In this section we examine the effects of illumination uniformity on core performance for moderate-convergence capsule implosions, as characterized by measurements of primary neutrons and knock-on charged particles. We start with the primary neutron yield, which provides one direct overall measure of core performance because of its strong dependence on ion temperature and density. Next we look at the yields of knock-on deuterons ( $Y_{\text{KOd}}$ ) and tritons ( $Y_{\text{KOt}}$ ), which provide a measure of  $\rho R_{\text{fuel}}$ , and thus the amount of compression (which is quantified by the convergence ratio Cr, defined as a ratio of the initial fuel radius to the final compressed fuel radius). After showing that the data demonstrate an improvement in performance with improved laser smoothing, we examine comparisons of the data with numerical simulations. These comparisons suggest that the poorer performance observed with less smoothing is due to intrinsically 2-D or 3-D effects such as instabilities and mix.

Primary neutron yields between  $3 \times 10^{12}$  and  $1.4 \times 10^{13}$  were obtained, and, in general, better energy balance resulted in higher primary neutron yield. The highest yield was obtained for the shot with a low-mode rms nonuniformity of  $\sim 1.3\%$  (energy balance to within 3.1%). Once on-target, low-mode nonuniformity due to beam imbalance has been decreased to the 5% rms range, single-beam nonuniformity becomes more important for capsule performance through its effects on high-order-mode perturbations. This is illustrated in Fig. 86.17(a), which indicates that beam smoothing with 1-THz, 2-D SSD + PS results in a primary yield ( $Y_n \sim 1.1 \times 10^{13}$ ) about 80% higher than that obtained with 0.35-THz, 2-D SSD and no PS ( $Y_n \sim 6.2 \times 10^{12}$ ). Since the ion temperature is found to be relatively insensitive to rms uniformity improvement, as shown in Fig. 86.17(b), higher  $Y_n$  must result from a higher ion density due to improved fuel compression.

While determining the  $\rho R_{\text{fuel}}$  from knock-on yields, efforts to match the experimental primary yields by assuming differ-

ent temperature profiles led to a preference of the uniform model over the hot-spot model because highly peaked temperature profiles led to yields that were too low, so the  $\rho R_{\text{fuel}}$  versus yield relationships shown in Fig. 86.14 must be modified. The corresponding inferred convergence ratio is

$$\text{Cr} = \sqrt{\rho R_{\text{fuel}} / \rho R_{\text{fuel}0}},$$

where  $\rho R_{\text{fuel}0}$  is the fuel  $\rho R$  before compression. As shown in Fig. 86.18, the data led to average values of  $\rho R_{\text{fuel}} \sim 9.3 \text{ mg/cm}^2$  (Cr  $\sim 12$ ) for the shots using 0.35-THz, 2-D SSD and  $\rho R_{\text{fuel}} \sim 15 \text{ mg/cm}^2$  (Cr  $\sim 15$ ) for 1-THz, 2-D SSD + PS. Increasing the smoothing rate increased  $\rho R_{\text{fuel}}$  by  $\sim 60\%$  and Cr by  $\sim 25\%$ .

One-dimensional (1-D) simulations were carried out for the studied shots. Figure 86.19 shows an example of how a measured knock-on deuteron spectrum compares with a prediction for shot 20698. Relative to the data, the simulation has a similar spectral shape, a similar energy downshift, and a similar, if somewhat higher, yield. Figures 86.20 to 86.23 provide an overview of data-to-simulation comparisons. Since the effects of beam smoothing are intrinsically 2-D or 3-D, the 1-D code predicts no difference due to smoothing; this can be seen in Figs. 86.20 and 86.21, which show that nearly all the shots are predicted to have the same values of  $\rho R_{\text{fuel}}$ , Cr, and  $T_i$ , with small differences due only to the small differences in capsule parameters and total laser energy. On the other hand,

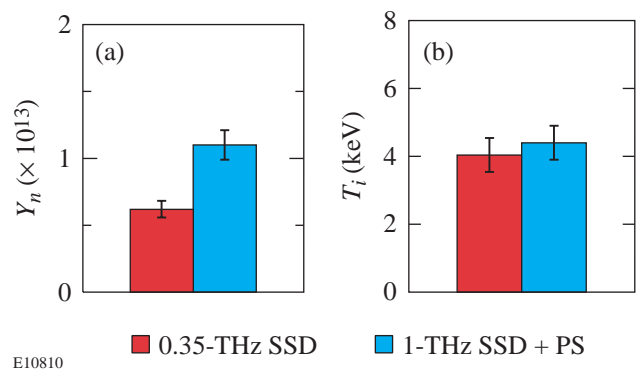


Figure 86.17

(a) Average primary yields achieved for two different single-beam smoothing conditions. The yield increases by about 80% when uniformity is improved using 1-THz, 2-D SSD + PS. (b) The yield-averaged ion temperature is insensitive to the improvement in uniformity. Consequently, the significant increase of primary yields cannot be attributed to the ion temperatures and is instead probably a consequence of an increase in ion density due to better fuel compression. The error bars display statistical uncertainties.

the measured values of  $\rho R_{\text{fuel}}$  (or Cr) improve significantly for increased laser smoothing and approach the predicted values with 1-THz, 2-D SSD + PS. Other parameters also increase when smoothing is improved, including  $Y_n$  and  $Y_{\text{KOd}}$ , whose ratios to predicted values (YOC and  $Y_{\text{KOd}}/Y_{1\text{-D}}$ , respectively) are shown in Fig. 86.22. Plotting the ratio of measured to predicted values of  $Y_{\text{KOd}}/Y_n$  against measured Cr, in Fig. 86.23, shows that it approaches unity for full beam smoothing. This suggests that the improvement of single-beam irradiation uniformity results in increased compression through the reduction of 2-D phenomena such as instabilities and mix.

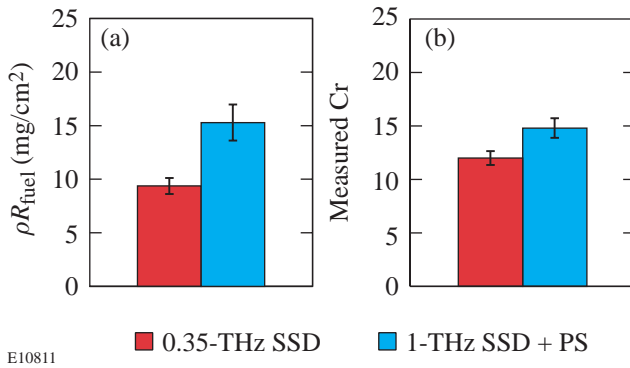


Figure 86.18 (a) Average fuel areal densities measured in experiments using 0.35-THz, 2-D SSD ( $\rho R_{\text{fuel}} \sim 9.3$  mg/cm<sup>2</sup>) and 1-THz, 2-D SSD + PS ( $\rho R_{\text{fuel}} \sim 15$  mg/cm<sup>2</sup>). A significant increase of the  $\rho R_{\text{fuel}}$  (~60%) is obtained using 1.0-THz, 2-D SSD + PS. (b) Experimentally measured convergence ratios. Cr ~ 12 for shots using 0.35-THz, 2-D SSD, and Cr ~ 15 for shots using 1-THz, 2-D SSD + PS. The error bars display statistical uncertainties.

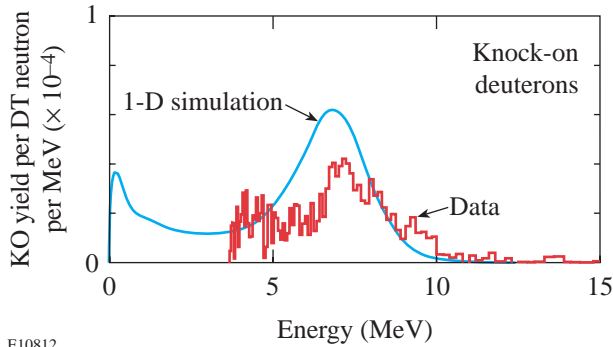


Figure 86.19 A comparison of the experimentally measured knock-on deuteron spectrum and the 1-D LILAC-predicted spectrum for shot 20698.

The credibility of this hypothesis is increased by more elaborate simulations that incorporate effects of Rayleigh–Taylor, Richtmyer–Meshkov, and Bell–Plesset instabilities, and 3-D Haan saturation<sup>5,7</sup> in the postprocessing of 1-D calculation results. It was shown that using 0.35-THz, 2-D SSD without PS can result in a mix width that exceeds the in-flight shell thickness.<sup>5,7</sup> The shell integrity is thus reduced, and the capsule compression is degraded. In contrast, the calculations show that with full beam smoothing (on-target beam nonuniformity less than 1% after 300 ps), the mix width is significantly smaller than the in-flight shell thickness.

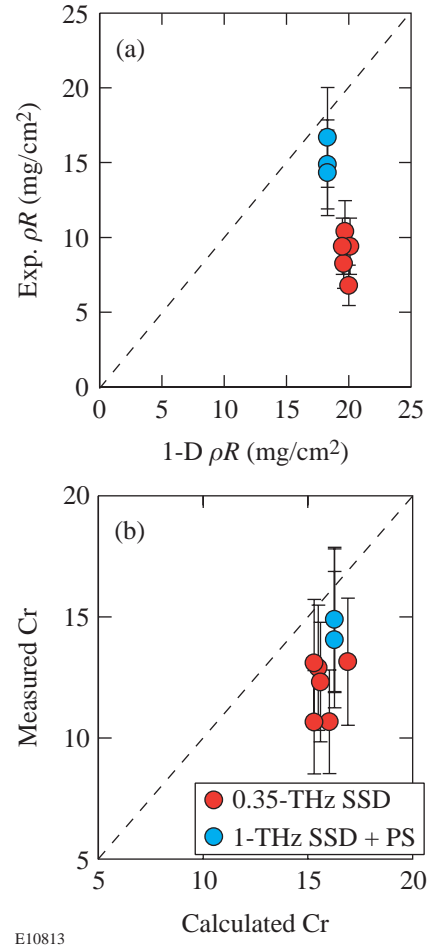
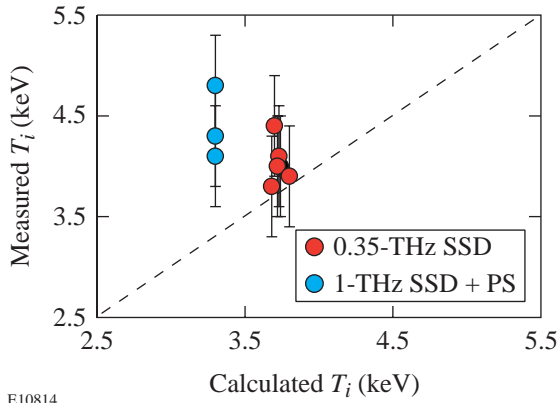
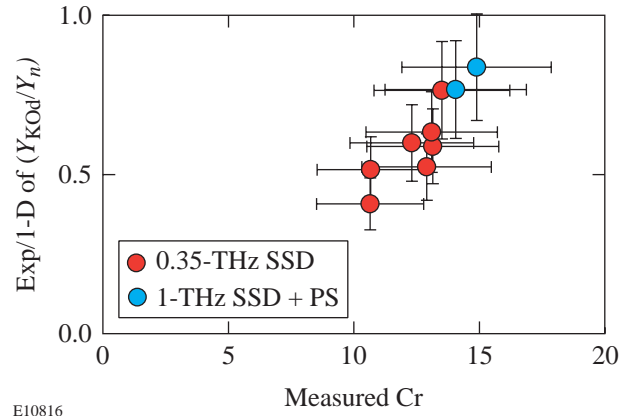


Figure 86.20 (a) Measured  $\rho R_{\text{fuel}}$  versus 1-D simulation prediction. For the shots with 0.35-THz, 2-D SSD, the average measured  $\rho R_{\text{fuel}}$  is about 60% of the prediction. For the shots with 1-THz, 2-D SSD + PS, an average of ~80% of the predicted  $\rho R_{\text{fuel}}$  is measured. This comparison suggests that the improvement in irradiation uniformity makes implosions more 1-D-like. (b) The measured convergence ratio plotted against the calculation. The experimental data are slightly but consistently lower than those of 1-D predictions. The error bars display experimental uncertainties (~10% for neutrons, ~20% for charged particles).



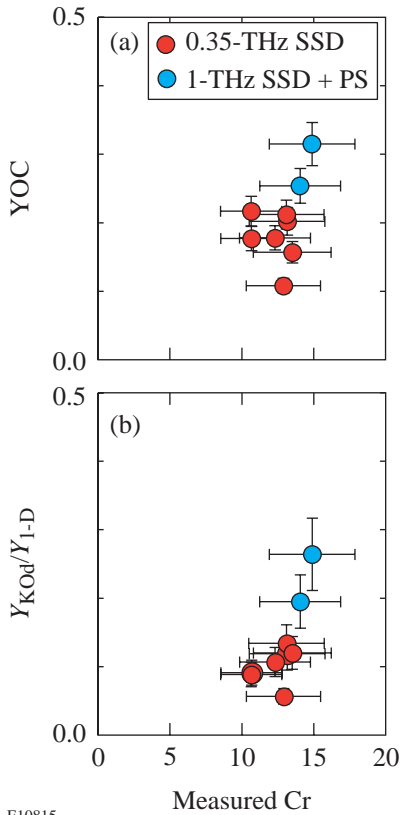
E10814

Figure 86.21  
A comparison of measured ion temperatures to the 1-D LILAC predictions, showing that measured values are consistently higher than predictions. The error bars display experimental uncertainty ( $\pm 0.5$  keV).



E10816

Figure 86.23  
The ratio of the experimentally measured value of  $Y_{KOd}/Y_n$  to the 1-D prediction for different measured Cr. About ~60% is obtained for the shots using 0.35-THz, 2-D SSD, and ~80% is obtained for the shots using 1-THz, 2-D SSD + PS. This ratio approaches unity, while YOC is considerably smaller ( $\leq 30\%$ ). The error bars indicate experimental uncertainties (~10% for neutrons, ~20% for charged particles).



E10815

Figure 86.22  
(a) The ratio of measured primary neutron yield to clean 1-D prediction (YOC) plotted against the measured convergence ratio. An average of ~18% is obtained for the shots using 0.35-THz, 2-D SSD, while an average of ~30% is obtained for the shots using 1-THz, 2-D SSD + PS. (b) The ratio of measured KO deuteron yield to 1-D prediction ( $Y_{KOd}/Y_{1-D}$ ) has an average of ~10% for the shots using 0.35-THz, 2-D SSD and of ~24% for the shots using 1-THz, 2-D SSD + PS. The error bars indicate experimental uncertainties (~10% for neutrons, ~20% for charged particles).

## 2. Shell Performance of Moderate-Convergence Capsule Implosions

The shell performance discussed in this section is based on measurements of  $\rho R_{\text{shell}}$  and shell electron temperature  $T_e$ . The  $\rho R_{\text{shell}}$  can be determined directly from the yield of knock-on protons (this is a temperature-independent method). Once  $\rho R_{\text{shell}}$  is known and  $\rho R_{\text{fuel}}$  has been determined as described in the previous section, the shell  $T_e$  can be estimated from the energy downshift of the deuteron and/or triton spectrum (slowing down of these particles is sensitive to  $T_e$ ). Alternatively, if the shell  $T_e$  is already known from other measurements, then the deuteron and/or triton downshifts can be used in an independent estimation of  $\rho R_{\text{shell}}$ .

Knock-on protons are generated only in the CH shell, and typical proton spectra are shown in Figs. 86.15(c) and 86.16(c). Values of  $\rho R_{\text{shell}}$  can be calculated from the proton yields with Fig. 86.14. As displayed in Fig. 86.24, an average  $\rho R_{\text{shell}}$  of ~45 mg/cm<sup>2</sup> is obtained for shots using 0.35-THz, 2-D SSD without PS, while an average  $\rho R_{\text{shell}}$  of ~60 mg/cm<sup>2</sup> is obtained for 1-THz, 2-D SSD + PS. A 35% increase of the  $\rho R_{\text{shell}}$  is thus obtained due to the improvement of single-beam uniformity. Figure 86.25 displays a 1-D calculated knock-on proton spectrum overlaid on an experimentally measured proton spectrum for shot 20698. The agreement between these two spectra suggests that, with full beam smoothing, shell performance of a moderate-convergence implosion is close to the 1-D prediction.

The directly determined value of  $\rho R_{\text{fuel}}$  (described in the previous section), together with the measured energy loss of the deuteron and/or triton knock-ons, can also be used to determine shell  $T_e$  (if  $\rho R_{\text{shell}}$  has been determined as described in the previous paragraph) or to study  $\rho R_{\text{shell}}$  (if the shell  $T_e$  is known). As deuteron and/or triton knock-ons from the fuel travel through fuel and shell, they lose an amount of energy directly proportional to the areal density of the materials they pass through (assuming there is no particle acceleration, as discussed below in Subsection 4). Because these particles are not so energetic, their stopping power is not characterized as “cold plasma stopping,” where there is no temperature dependence, but “warm plasma stopping,” where there is a temperature dependence. The energy loss can be calculated from the stopping power in a fully ionized plasma:<sup>31,32</sup>

$$\frac{dE}{dx} = - \left( \frac{Z^2 \omega_p e}{v_t} \right)^2 \times \left[ G(x^{t/f}) \ell n \Lambda + \theta(x^{t/f}) \ell n \left( 1.123 \sqrt{x^{t/f}} \right) \right], \quad (7)$$

where  $\theta(x^{t/f})$  is a step function and equals 0 (1) when  $x^{t/f} < 1$  ( $> 1$ );  $\omega_p = (4\pi n_e e^2 / m_e)^{1/2}$  is the electron plasma frequency;  $Z$  is the charge of the incident charged particle;  $v_t$  ( $v_f$ ) is the velocity of a test (field) charged particle;  $x^{t/f} = v_t^2 / v_f^2$ ; and  $\ell n \Lambda$  is the Coulomb logarithm.  $G(x^{t/f})$  is defined as

$$G(x^{t/f}) = \mu(x^{t/f}) - \frac{m_f}{m_t} \left\{ \frac{d\mu(x^{t/f})}{dx^{t/f}} - \frac{1}{\ell n \Lambda} \left[ \mu(x^{t/f}) + \frac{d\mu(x^{t/f})}{dx^{t/f}} \right] \right\}, \quad (8)$$

where

$$\mu(x^{t/f}) = 2 \int_0^{x^{t/f}} e^{-\xi} \sqrt{\xi} d\xi / \sqrt{\pi}$$

is the Maxwell integral and  $m_t$  ( $m_f$ ) is the mass of the test (field) particle. Since the effects of large-angle scattering are negligible for charged particles traveling in plasmas of interest,<sup>32</sup> the areal density through which a charged particle travels with an energy loss ( $\Delta E \approx E_0 - E$ ) can be approximately determined as

$$\rho R = \int_E^{E_0} \rho \left( \frac{dE}{dx} \right)^{-1} dx. \quad (9)$$

Because of the relatively high temperature and low density of the fuel plasma, the energy loss is dominated by the lower-temperature but higher-density shell plasma. The total areal density is defined as  $\rho R_{\text{total}} = \rho R_{\text{fuel}} + \rho R_{\text{shell}}$ .

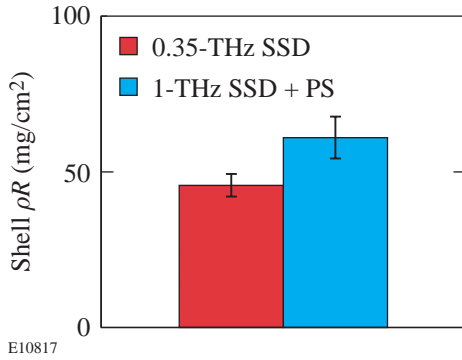


Figure 86.24  
An average measured  $\rho R_{\text{shell}}$  of  $\sim 45$  mg/cm<sup>2</sup> is obtained for the shots using 0.35-THz, 2-D SSD, and a  $\rho R_{\text{shell}}$  of  $\sim 60$  mg/cm<sup>2</sup> is obtained for the shots using 1-THz, 2-D SSD + PS. The error bars display statistical uncertainties.

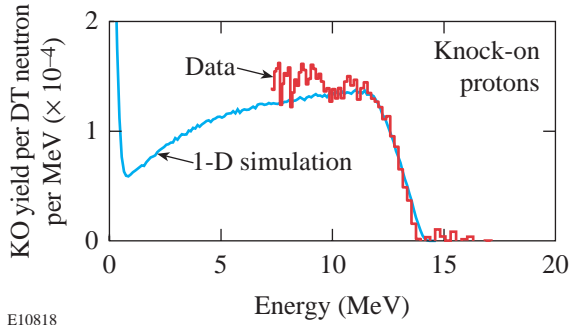


Figure 86.25  
A comparison of the measured knock-on proton spectrum (red line) to the 1-D *LILAC* prediction (blue line) for shot 20698. The agreement between these two spectra suggests the compressed shell has nearly 1-D performance. (The fact that the predicted spectrum is not flat, and decays in the region between 0 to 8 MeV, is due to the fact that low-energy protons generated during the stagnation phase of the implosion may experience a large  $\rho R_{\text{shell}}$  and be ranged out.)

The downshifts of the spectra shown in Figs. 86.16(a) and 86.16(b) (for shot 20698) are about 5 MeV for tritons and 4 MeV for deuterons. To be consistent with the temperature-independent, knock-on-derived values of  $\rho R_{\text{fuel}} \sim 14 \text{ mg/cm}^2$  and  $\rho R_{\text{shell}} \sim 64 \text{ mg/cm}^2$  calculated as described above for this shot, the value of shell  $T_e$  must be about 0.6 keV. A summary of calculated shell  $T_e$  values for different shots is given in Fig. 86.26. Shell  $T_e$  appears insensitive to single-beam irradiation uniformity, to first order, although some subtle issues such as time and spatial dependence of the knock-on spectra are involved in this determination. This topic is a subject for future study.

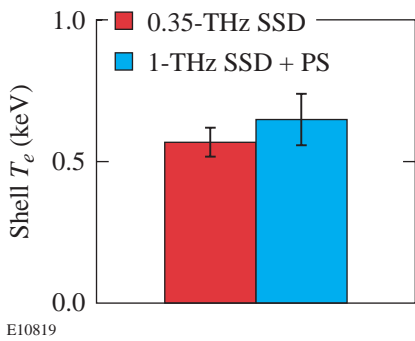


Figure 86.26 Average electron temperatures inferred from the knock-on spectra. Values of ~0.58 keV and ~0.65 keV are obtained for the shots using 0.35-THz, 2-D SSD and 1 THz, 2-D SSD + PS, respectively. The error bars display statistical uncertainties.

### 3. Similarity to D<sub>2</sub>-Filled-Capsule Implosions

With similar experimental conditions, implosions of DT- and D<sub>2</sub>-gas-filled plastic capsules are “hydrodynamically” equivalent. While some subtle differences, such as the mass, fusion cross section, equation of the state, etc., still exist, the basic capsule performance is expected to be similar. Recent work<sup>11</sup> has resulted in the study of fuel and shell parameters for D<sub>2</sub> shots on OMEGA by measuring spectra of secondary D<sup>3</sup>He protons. Those numbers are very similar to the knock-on-inferred numbers for related DT shots, as shown in Table 86.I. In general, the inferred and estimated  $\rho R_{\text{fuel}}$  and  $\rho R_{\text{shell}}$  along with  $\rho R_{\text{total}}$  are very similar for both DT- and D<sub>2</sub>-capsule implosions under similar experimental conditions. While the corresponding values of YOC are similar, DT implosions result in higher ion temperatures than D<sub>2</sub> implosions. The improvement of the single-beam irradiation uniformity enhances the target performance of both DT and D<sub>2</sub> implosions:  $\rho R_{\text{fuel}}$  ( $\rho R_{\text{shell}}$ ) increases ~60% (~35%) for DT implosions and ~65% (~40%) for D<sub>2</sub> implosions;  $Y_n$  increases ~80% for both DT and D<sub>2</sub> implosions; YOC increases ~60% for DT and ~80% for D<sub>2</sub> implosions. Ion temperatures are not so sensitive to the uniformity improvement ( $\leq 10\%$ ).

### 4. Capsule Charging and Particle Acceleration

Time-dependent capsule charging is an essential issue in a spherical implosion. This charging may result in a strong electric field surrounding the capsule and an acceleration of emitted charged particles. Since the measurement of areal densities of imploded capsules through charged-particle spectroscopy relies on accurate determination of particle-energy downshift due to slowing in the capsule, any particle acceleration could introduce serious errors.

Table 86.I: Comparison of DT- and D<sub>2</sub>-gas-filled-plastic-shell implosions (the D<sub>2</sub> numbers are from Ref. 11).

Capsules	Single-beam smoothing	$T_i$ (keV)	$Y_n$	YOC	$Y_{\text{Kod}}/Y_{1-D}$	$Y_{2p}/Y_{1-D}$	$\rho R_{\text{fuel}}$ (mg/cm <sup>2</sup> )	$\rho R_{\text{shell}}$ (mg/cm <sup>2</sup> )	$\rho R_{\text{total}}$ (mg/cm <sup>2</sup> )
DT (15) CH(20)	0.3-THz, 2-D SSD	4.1±0.5	(6.2±1.4)×10 <sup>12</sup>	0.18	0.10	—	9.3±1.9	46.8±7.6	~56*
	1-THz, 2-D SSD + PS	4.4±0.5	(1.1±0.3)×10 <sup>13</sup>	0.30	0.24	—	15.3±2.1	61.4±6.9	~76*
D <sub>2</sub> (15) CH(20)	0.3-THz, 2-D SSD	3.4±0.5	(8.8±0.8)×10 <sup>10</sup>	0.18	—	0.13	10.0±2.0	~43**	52
	1-THz, 2-D SSD + PS	3.7±0.5	(1.6±0.5)×10 <sup>10</sup>	0.33	—	0.21	14.0±7.4	~57**	72
*Estimated based on measured $\rho R_{\text{fuel}}$ and $\rho R_{\text{shell}}$ .									
**Estimated based on measured $\rho R_{\text{fuel}}$ and $\rho R_{\text{total}}$ .									

Many previous experiments have demonstrated the existence of capsule charging and particle acceleration, even (unexpectedly) on OMEGA with laser intensities of  $\sim 10^{15}$  W/cm<sup>2</sup> and 351-nm wavelength (where energy upshifts of  $\sim 1$  MeV have been observed for charged-fusion products and ablator protons<sup>10,33,34</sup>). The hot electrons generated by laser-plasma instabilities in the corona are thought to cause this capsule charging. Earlier experiments also suggest that the charge is time dependent.

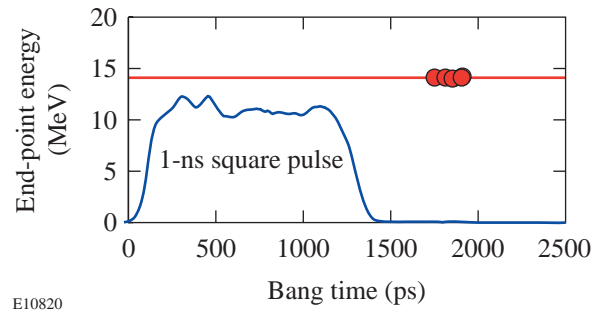
For estimating the effects of the electric fields on charged-fusion products, it has previously been assumed that such effects are important only when the bang time occurs while the laser is on (for example, for a thin-glass-shell capsule driven by 1-ns square pulse).<sup>35,36</sup> Such effects are assumed unimportant when the bang time occurs several hundreds of picoseconds after the laser turns off, when the electric field has largely decayed away (for example, a thick-plastic-shell capsule driven by a 1-ns square pulse<sup>10,33</sup>). For the latter case, possible energy upshifts, if any, have been assumed to be completely negligible. Although widely used when determining the spectral downshifts of charged particles,<sup>10,33</sup> these assumptions have never been directly proven by experiments because the effects of particle acceleration and slowing down are always mixed in an implosion for charged-fusion products.

The knock-on proton data described in this article provide direct proof of this assumption for thick-plastic-shell capsules driven by 1-ns square laser pulses. Any acceleration would cause the upper end points of the knock-on proton spectra to be up-shifted relative to the 14-MeV end point of the birth spectrum. In Figs. 86.15(c) and 86.16(c), the end points of the knock-on proton spectra are precisely (within statistical errors) at 14 MeV, which indicates that the protons are subject to no accelerations. Figure 86.27 shows the measured end points of these and other knock-on proton spectra for a number of shots, plotted against the bang time (a typical 1-ns square pulse on OMEGA is also displayed for reference). The laser pulse has completely ended at  $\sim 1400$  ps, while the bang time occurs several hundreds of picoseconds later. No energy upshifts are observed.

### 5. Relevance to OMEGA Cryogenic-Capsule Implosions

Plans exist to implode on OMEGA cryogenic DT capsules that typically have low-pressure DT-gas fill in the center surrounded by about 90  $\mu\text{m}$  of DT ice with  $\sim 2$   $\mu\text{m}$  of CH as an ablator. These implosions are predicted to generate DT primary yields  $>10^{13}$ , with an ion temperature between 1 to 4 keV and areal densities up to  $\sim 300$  mg/cm<sup>2</sup>. Nuclear diagnos-

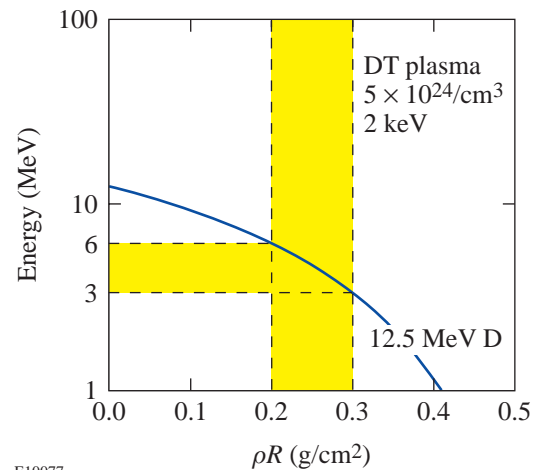
tics will play an important role in the OMEGA cryogenic program. Figure 86.28 shows the energy of knock-on deuterons plotted against their range ( $\rho R$ ) in a DT plasma (an electron temperature of 2 keV and an ion density of  $5 \times 10^{24}$  are assumed, although the density effects on these calculations are weak<sup>31,32</sup>). For a typical areal density of 200 to 300 mg/cm<sup>2</sup>, a knock-on deuteron will lose about 6 to 9 MeV as it traverses the capsule, and the remaining energy of 3 to 6 MeV is readily detectable using CPS.<sup>12</sup>



E10820

Figure 86.27

The measured upper-energy end points of the knock-on proton spectra for a number of shots in this study are plotted against the bang time (a typical 1-ns square pulse with an arbitrary unit for laser intensity on OMEGA is also displayed for reference). As seen, the laser pulse has completely ended at  $\sim 1400$  ps, while the bang times occur at 1750 to 1950 ps. The energies match the maximum scattered-proton energy, indicating that there are no energy upshifts.



E10077

Figure 86.28

The energy of knock-on deuterons versus their range ( $\rho R$ ) in a DT plasma. In this calculation, an electron temperature of 2 keV and an ion density of  $5 \times 10^{24}$  have been assumed. For a typical predicted areal density of 200 to 300 mg/cm<sup>2</sup> for a cryogenic-capsule implosion, a knock-on deuteron will lose about 6 to 9 MeV of energy, and the residual energy (3 to 6 MeV) left after leaving the target is readily detectable using charged-particle spectrometry.

## Summary and Conclusions

Direct-drive implosions of DT-gas-filled plastic capsules were studied using nuclear diagnostics on OMEGA. In addition to the traditional neutron measurements, comprehensive and high-resolution spectra of knock-on deuterons, tritons, and protons were obtained for the first time in ICF experiments and used to characterize target performance.

Target performance is improved, for moderate-convergence implosions ( $Cr \sim 10$  to  $20$ ), with the reduction of on-target irradiation nonuniformity that results from an improvement in beam-to-beam laser energy balance and an enhancement of single-beam uniformity. With the use of a 1-THz bandwidth of smoothing by spectral dispersion and polarization smoothing,  $Y_n \sim 1.1 \times 10^{13}$ ,  $YOC \sim 0.3$ ,  $\rho R_{\text{fuel}} \sim 15 \text{ mg/cm}^2$ , and  $\rho R_{\text{shell}} \sim 60 \text{ mg/cm}^2$ , which are, respectively, approximately 80%, 60%, 60%, and 35% higher than those determined when using a 0.35-THz bandwidth of smoothing by spectral dispersion. Polarization smoothing of individual laser beams is believed to play an important role.

With full beam smoothing, these implosions have some performance parameters close to one-dimensional-code predictions (e.g., a measured ratio of  $Y_{\text{KOd}}/Y_n$  achieves  $\sim 80\%$  of 1-D predictions). Data suggest that high irradiation uniformity results in reduced Rayleigh–Taylor growth and improved shell integrity. In addition, a brief comparison demonstrates the hydrodynamic “equivalence” of DT-filled capsules and  $D_2$ -filled capsules for moderate-convergence implosions.

## ACKNOWLEDGMENT

We express our appreciation to the OMEGA Laser and Experimental Operations and Target Fabrication crews for their excellent work and continuous support. This work has been supported in part by LLE (subcontract P0410025G) and LLNL (subcontract B313975), and by the U.S. Department of Energy Office of Inertial Confinement Fusion under Cooperative Agreement NO. DE-FC03-92SF19460, the University of Rochester, and New York State Energy Research and Development Authority. The support of DOE does not constitute an endorsement by DOE of the views expressed in this work.

## REFERENCES

1. J. D. Lindl, R. L. McCrory, and E. M. Campbell, *Phys. Today* **45**, 32 (1992).
2. J. D. Lindl, *Inertial Confinement Fusion: The Quest for Ignition and Energy Gain Using Indirect Drive* (Springer-Verlag, New York, 1998).
3. S. W. Haan *et al.*, *Phys. Plasmas* **2**, 2480 (1995).
4. T. R. Boehly, D. L. Brown, R. S. Craxton, R. L. Keck, J. P. Knauer, J. H. Kelly, T. J. Kessler, S. A. Kumpan, S. J. Loucks, S. A. Letzring, F. J. Marshall, R. L. McCrory, S. F. B. Morse, W. Seka, J. M. Soures, and C. P. Verdon, *Opt. Commun.* **133**, 495 (1997).
5. R. L. McCrory, R. E. Bahr, R. Betti, T. R. Boehly, T. J. B. Collins, R. S. Craxton, J. A. Delettrez, W. R. Donaldson, R. Epstein, J. Frenje, V. Yu. Glebov, V. N. Goncharov, O. V. Gotchev, R. Q. Gram, D. R. Harding, D. G. Hicks, P. A. Jaanimagi, R. L. Keck, J. Kelly, J. P. Knauer, C. K. Li, S. J. Loucks, L. D. Lund, F. J. Marshall, P. W. McKenty, D. D. Meyerhofer, S. F. B. Morse, R. D. Petrasso, P. B. Radha, S. P. Regan, S. Roberts, F. Séguin, W. Seka, S. Skupsky, V. A. Smalyuk, C. Sorce, J. M. Soures, C. Stoeckl, R. P. J. Town, M. D. Wittman, B. Yaakobi, and J. D. Zuegel, “OMEGA ICF Experiments and Preparation for Direct-Drive Ignition on NIF,” to be published in the *Proceedings of the 18th IAEA Fusion Energy Conference*.
6. J. M. Soures, R. L. McCrory, C. P. Verdon, A. Babushkin, R. E. Bahr, T. R. Boehly, R. Boni, D. K. Bradley, D. L. Brown, R. S. Craxton, J. A. Delettrez, W. R. Donaldson, R. Epstein, P. A. Jaanimagi, S. D. Jacobs, K. Kearney, R. L. Keck, J. H. Kelly, T. J. Kessler, R. L. Kremens, J. P. Knauer, S. A. Kumpan, S. A. Letzring, D. J. Lonobile, S. J. Loucks, L. D. Lund, F. J. Marshall, P. W. McKenty, D. D. Meyerhofer, S. F. B. Morse, A. Okishev, S. Papernov, G. Pien, W. Seka, R. Short, M. J. Shoup III, M. Skeldon, S. Skupsky, A. W. Schmid, D. J. Smith, S. Swales, M. Wittman, and B. Yaakobi, *Phys. Plasmas* **3**, 2108 (1996).
7. D. D. Meyerhofer, J. A. Delettrez, R. Epstein, V. Yu. Glebov, V. N. Goncharov, R. L. Keck, R. L. McCrory, P. W. McKenty, F. J. Marshall, P. B. Radha, S. P. Regan, S. Roberts, W. Seka, S. Skupsky, V. A. Smalyuk, C. Sorce, C. Stoeckl, J. M. Soures, R. P. J. Town, B. Yaakobi, J. D. Zuegel, J. Frenje, C. K. Li, R. D. Petrasso, D. G. Hicks, F. H. Séguin, K. Fletcher, S. Padalino, M. R. Freeman, N. Izumi, R. Lerche, T. W. Phillips, and T. C. Sangster, *Phys. Plasmas* **8**, 2251 (2001).
8. F. J. Marshall, J. A. Delettrez, V. Yu. Glebov, R. P. J. Town, B. Yaakobi, R. L. Kremens, and M. Cable, *Phys. Plasmas* **7**, 1006 (2000).
9. F. J. Marshall, J. A. Delettrez, R. Epstein, V. Yu. Glebov, D. R. Harding, P. W. McKenty, D. D. Meyerhofer, P. B. Radha, W. Seka, S. Skupsky, V. A. Smalyuk, J. M. Soures, C. Stoeckl, R. P. Town, B. Yaakobi, C. K. Li, F. H. Séguin, D. G. Hicks, and R. D. Petrasso, *Phys. Plasmas* **7**, 2108 (2000).
10. C. K. Li, D. G. Hicks, F. H. Séguin, J. A. Frenje, R. D. Petrasso, J. M. Soures, P. B. Radha, V. Yu. Glebov, C. Stoeckl, D. R. Harding, J. P. Knauer, R. L. Kremens, F. J. Marshall, D. D. Meyerhofer, S. Skupsky, S. Roberts, C. Sorce, T. C. Sangster, T. W. Phillips, M. D. Cable, and R. J. Leeper, *Phys. Plasmas* **7**, 2578 (2000).
11. F. H. Séguin, C. K. Li, D. G. Hicks, J. A. Frenje, K. M. Green, R. D. Petrasso, J. M. Soures, D. D. Meyerhofer, V. Yu. Glebov, C. Stoeckl, P. B. Radha, S. Roberts, C. Sorce, T. C. Sangster, M. D. Cable, S. Padalino, and K. Fletcher, “Using Secondary Proton Spectra to Study Imploded  $D_2$ -Filled Capsules at the OMEGA Laser Facility,” submitted to *Physics of Plasmas*.

12. J. A. Frenje, K. M. Green, C. K. Li, F. H. Séguin, R. D. Petrasso, S. Roberts, V. Yu. Glebov, D. D. Meyerhofer, J. M. Soures, D. G. Hicks, T. W. Phillips, T. C. Sangster, K. Fletcher, L. Baumgart, H. Olliver, S. Padalino, S. Thompson, and B. White, "Diagnostic Measurements of Charged Particles from DD, D<sup>3</sup>He, and DT Implosions at the OMEGA Laser Facility Using CR-39 Particle Detectors," to be submitted to Review of Scientific Instruments.
13. P. B. Radha, S. Skupsky, R. D. Petrasso, and J. M. Soures, *Phys. Plasmas* **7**, 1531 (2000).
14. S. Skupsky and R. S. Craxton, *Phys. Plasmas* **6**, 2157 (1999).
15. V. Yu. Glebov, D. D. Meyerhofer, and C. Stoeckl, *Bull. Am. Phys. Soc.* **45**, 144 (2000).
16. M. A. Russotto and R. L. Kremens, *Rev. Sci. Instrum.* **61**, 3125 (1990).
17. J. D. Kilkenny, M. D. Cable, C. A. Clower, B. A. Hammer, V. P. Karpenko, R. L. Kauffman, H. N. Kornblum, B. J. MacGowan, W. Olson, T. J. Orzechowski, D. W. Phillion, G. L. Tietbohl, J. E. Trebes, B. Chrien, B. Failor, A. Hauer, R. Hockaday, J. Oertel, R. Watt, C. Ruiz, G. Cooper, D. Hebron, L. Leeper, J. Porter, and J. Knauer, *Rev. Sci. Instrum.* **66**, 288 (1995).
18. R. J. Leeper, G. A. Chandler, G. W. Cooper, M. S. Derzon, D. L. Fehl, D. L. Hebron, A. R. Moats, D. D. Noack, J. L. Porter, L. E. Ruggles, J. A. Torres, M. D. Cable, P. M. Bell, C. A. Clower, B. A. Hammel, D. H. Kalantar, V. P. Karpenko, R. L. Kauffman, J. D. Kilkenny, F. D. Lee, R. A. Lerche, B. J. MacGowan, M. J. Moran, M. B. Nelson, W. Olson, T. J. Orzechowski, T. W. Phillips, D. Ress, G. L. Tietbohl, J. E. Trebes, R. J. Bartlett, R. Berggren, S. E. Caldwell, R. E. Chrien, B. H. Failor, J. C. Fernandez, A. Hauer, G. Idzorek, R. G. Hockaday, T. J. Murphy, J. Oertel, R. Watt, M. Wilke, D. K. Bradley, J. Knauer, R. D. Petrasso, and C. K. Li, *Rev. Sci. Instrum.* **68**, 868 (1997).
19. R. A. Lerche, D. W. Phillion, and G. L. Tietbohl, *Rev. Sci. Instrum.* **66**, 933 (1995).
20. D. G. Hicks, C. K. Li, R. D. Petrasso, F. H. Séguin, B. E. Burke, J. P. Knauer, S. Cremer, R. L. Kremens, M. D. Cable, and T. W. Phillips, *Rev. Sci. Instrum.* **68**, 589 (1997).
21. D. G. Hicks, "Charged Particle Spectroscopy: A New Window on Inertial Confinement Fusion," Ph.D. thesis, Massachusetts Institute of Technology, 1999.
22. F. H. Séguin *et al.*, "A Proton Spectrometer Based on a Wedge-Shaped Range Filter and CR39 Nuclear Track Detectors," to be submitted to Review of Scientific Instruments.
23. S. Skupsky and S. Kacenjar, *J. Appl. Phys.* **52**, 2608 (1981).
24. S. Kacenjar, S. Skupsky, A. Entenberg, L. Goldman, and M. Richardson, *Phys. Rev. Lett.* **49**, 463 (1982).
25. E. M. Campbell *et al.*, *J. Appl. Phys.* **51**, 6062 (1980).
26. M. D. Cable and S. P. Hatchett, *J. Appl. Phys.* **62**, 2233 (1987).
27. H. Azechi, M. D. Cable, and R. O. Stapf, *Laser Part. Beams* **9**, 119 (1991).
28. R. D. Petrasso, C. K. Li, M. D. Cable, S. M. Pollaine, S. W. Haan, T. P. Bernat, J. D. Kilkenny, S. Cremer, J. P. Knauer, C. P. Verdon, and R. L. Kremens, *Phys. Rev. Lett.* **77**, 2718 (1996).
29. S. Cremer, C. P. Verdon, and R. D. Petrasso, *Phys. Plasmas* **5**, 4009 (1998).
30. E. Goldman, Laboratory for Laser Energetics Report No. 16, University of Rochester (1973).
31. C. K. Li and R. D. Petrasso, *Phys. Rev. Lett.* **70**, 3059 (1993).
32. C. K. Li and R. D. Petrasso, *Phys. Plasmas* **2**, 2460 (1995).
33. D. G. Hicks, C. K. Li, F. H. Séguin, A. K. Ram, J. A. Frenje, R. D. Petrasso, J. M. Soures, V. Yu. Glebov, D. D. Meyerhofer, S. Roberts, C. Sorce, C. Stockl, T. C. Sangster, and T. W. Phillips, *Phys. Plasmas* **7**, 5106 (2000).
34. D. G. Hicks, C. K. Li, F. H. Séguin, J. D. Schnittman, A. K. Ram, J. A. Frenje, R. D. Petrasso, J. M. Soures, D. D. Meyerhofer, S. Roberts, C. Sorce, C. Stoeckl, T. C. Sangster, and T. W. Phillips, *Phys. Plasmas* **8**, 606 (2001).
35. Y. Gazit, J. Delettrez, T. C. Bristow, A. Entenberg, and J. Soures, *Phys. Rev. Lett.* **43**, 1943 (1979).
36. J. Delettrez, A. Entenberg, Y. Gazit, D. Shvarts, J. Virmont, T. Bristow, J. M. Soures, and A. Bennish, *Nucl. Fusion* **23**, 1135 (1983).

---

# A Consistent Measurement-Based Picture of Core-Mix in Direct-Drive Implosions on OMEGA

## Introduction

The central goal of direct-drive implosions on the OMEGA laser<sup>1</sup> is to validate the performance of the high-gain, direct-drive ignition designs<sup>2</sup> planned for use on the National Ignition Facility. Inferring the density, temperature, and fuel–shell mix of ignition-relevant capsule implosions is important in validating models of implosions. To this end, diagnostic information from sets of implosions that differ in their hydrodynamic properties has been obtained in direct-drive spherical-capsule implosions on OMEGA. In this article, we report on an analysis of the experimental charged-particle and neutron data that provide consistent information on densities and temperatures of one set of similar experiments.

In direct-drive implosions, a spherical target is illuminated uniformly with a laser. Any degradation in target performance is believed to occur primarily through the Rayleigh–Taylor instability,<sup>3</sup> which is seeded by either target imperfections or laser nonuniformity. This instability, occurring at the ablation surface during the acceleration phase of the implosion, can then feed through to the fuel–shell interface and add to any pre-existing roughness on the inner surface. During the deceleration phase, these distortions at the fuel–shell interface grow, resulting in a mixing of the fuel and shell material. Neutron and charged-particle diagnostics carry direct information about this phase of the implosion, when fuel densities and temperatures are high enough for their production.

Several complementary approaches can be used to analyze the implosion observables. One route is to infer, from individual diagnostics, parameters such as the fuel areal density, which is a measure of compression. Comparisons of inferred quantities with those from simulations indicate the closeness of the actual implosions to the simulations. The problem with this technique is usually that simple models used to infer key quantities from individual diagnostics (such as “ice-block” models) may not apply to the actual implosion. Further, this technique ignores complementary information from other diagnostics that may be critical to devising the correct model. Another possible technique is to directly simulate the experi-

ment and post-process the simulation for the relevant diagnostic. Again, the comparison is very model dependent, and further light on any disagreement between simulations and experiment is difficult to obtain through this route. The third method, described in this article, is to use all observables from a set of hydrodynamically similar implosions and infer a picture that is consistent across all diagnostics. This picture would correspond to a neutron-weighted, “1-D” description of temperature and density profiles in the core and mix region of the imploding target. The advantage of such a scheme is that it provides a picture using all available information and allows for more detailed comparisons between simulation and experiment through a sensitivity analysis of the model parameters.

In this article, we describe a consistent picture, inferred from different diagnostics, of conditions in the fuel core and mix region for 20- $\mu\text{m}$ -thick-plastic-shell implosions. These targets are of interest because their stability during the acceleration phase is calculated to be similar to those predicted for OMEGA cryogenic implosions,<sup>4</sup> which, in turn, are energy-scaled surrogates<sup>5</sup> for direct-drive ignition targets.<sup>2</sup> Studies on these targets should then be applicable to both OMEGA cryogenic and NIF ignition targets. Experiments with plastic targets also offer a larger array of diagnostic techniques, allowing for more information on target behavior.

The following sections (1) describe the targets modeled and the diagnostics used to probe these targets, (2) present evidence for mixing and the mix model, and (3) present our conclusions.

## Targets and Diagnostics

The experiments chosen for this analysis had nominally identical laser pulse shapes, smoothing conditions, target-shell thickness, and gas pressure. The makeup of the fill gas or details of the shell layers were then varied so that complementary diagnostics could be applied to hydrodynamically similar implosions. Since implosions on OMEGA show excellent reproducibility,<sup>4</sup> variation between different shots is relatively small, allowing for such an analysis. We consider targets with 20- $\mu\text{m}$ -thick plastic shells (pure CH or with CD layers) with

different gas fills ( $D_2$ , DT,  $^3He$ ) at 15 atm (see Fig. 86.29 for a description of targets and corresponding observables). These targets were irradiated with a 1-ns square laser pulse with 23-kJ energy and used full-beam smoothing (2-D smoothing by spectral dispersion with 1-THz bandwidth and polarization smoothing using birefringent wedges).

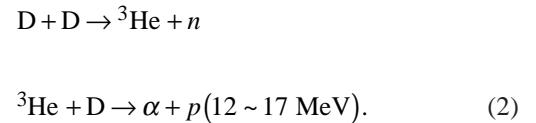
For the  $D_2$ -filled targets, the neutron diagnostics involved measurements of primary neutron yields from the DD reactions and neutron-averaged ion temperatures, measured using neutron time-of-flight detectors.<sup>4</sup> In addition, secondary neutron yields,<sup>6</sup> which are produced by the following sequence of reactions,



are also measured using current-mode detectors.<sup>7</sup> Tritons in the primary DD reaction produced at energies of about 1 MeV cause secondary reactions with the fuel deuterons as they move through the target. The ratio of the secondary neutron yields to the primary DD neutron yields depends on the fuel areal

density. Secondary neutron yields can also depend sensitively, however, on the temperatures in the target, through the slowing down of the triton and the energy-dependent cross section of the reaction. With the cross section increasing significantly with decreasing energy of the triton (the cross section increases by nearly a factor of 5 between the triton birth energy and about 0.1 MeV), this diagnostic is particularly sensitive to the effects of mix; the shell material mixed in with the fuel could contribute to the greater slowing down of the triton and consequently an increased secondary neutron yield.

Secondary protons,<sup>8</sup> in an analogous reaction to that of the secondary neutrons, are produced in  $D_2$ -filled targets. Here, the second main branch of the DD reaction produces primary  $^3He$  particles, which in turn fuse with the background deuterons as they traverse the fuel region:



Again, this reaction is dependent on the areal density of the fuel and the slowing down of the primary  $^3He$  particles. In this case, however, the cross section of the reaction decreases significantly with increasing slowing down of the  $^3He$  particle. Therefore, when slowing down is significant, the areal density local to the primary  $^3He$  production essentially determines the secondary proton yield. Measurements of secondary proton spectra are carried out using a magnet-based charged-particle spectrometer (CPS) as well as “wedge-range-filter”-based spectrometers using CR-39 track detectors.<sup>8</sup>

The number of elastically scattered deuterons and tritons (“knock-ons”) is directly proportional to the fuel areal density for DT-filled targets.<sup>9</sup> Since the elastic scattering of the 14-MeV DT neutrons off the background fuel ions produces these particles, these diagnostics are relatively insensitive to the location of the fuel and therefore mix. A forward-scattered peak in the particle spectrum characterizes this diagnostic. The number of knock-on particles in this forward-scattered peak is expected to be a constant fraction of the total produced and therefore provides a measure of the total fuel areal density. Detailed knock-on particle spectra have been measured using the CPS and used to infer areal density in DT-filled targets.<sup>10</sup>

In addition to the plastic shells mentioned above, direct information regarding the clean core of fuel and the mixing of the fuel and shell can be obtained from plastic-shell implosions

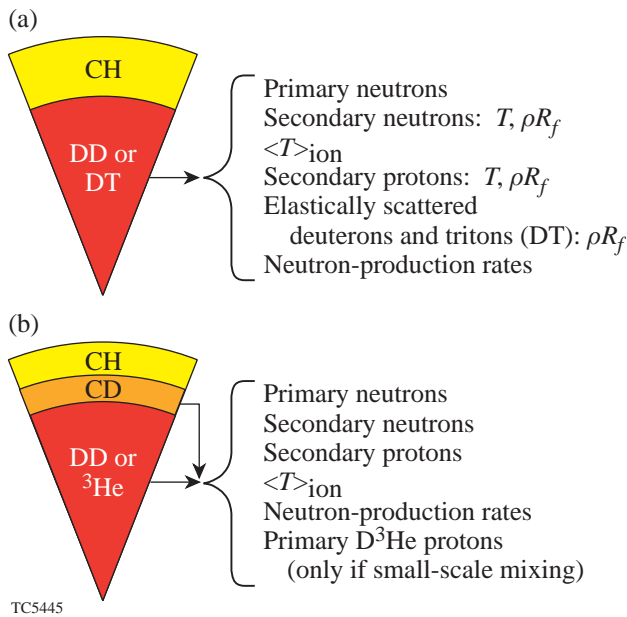


Figure 86.29 A large suite of diagnostics has been brought to bear on plastic shells with and without CD layers and with different gas fills. The different targets and the observables that are characteristic of the targets are shown.

with an embedded CD layer and with  $^3\text{He}$  fill [Fig. 86.29(b)]. With a CD layer an observable signal of primary  $\text{D}^3\text{He}$  protons is produced when a significant number of deuterons from the CD layer come into contact with the  $^3\text{He}$  in the fuel. Again, the proton yield is measured using the CPS. Preliminary experiments have used targets with the CD layer at both the fuel-shell interface and a distance of  $1\ \mu\text{m}$  displaced from this interface.

**Evidence of Mixing and the Mix Model**

A comparison of particle yields with those from 1-D simulations using *LILAC*<sup>11</sup> suggests mixing of the fuel and shell. Figure 86.30 shows experimental observables and results from the corresponding 1-D simulations that contain no effects of mixing. The relatively model independent knock-ons indicate fuel areal densities of  $15\ \text{mg}/\text{cm}^2$ , nearly 93% of 1-D values. Figure 86.30 also indicates, however, that the neutron yields from the DD reaction are only about 33% of 1-D. One explanation for this reduction in the yield is the mixing of cold shell material into the hot fuel. The fuel consequently cools, quenching the yield. In the unmixed 1-D simulations, most of the neutron yield is produced at a radius that is about two-thirds the distance from the fuel-shell interface. Therefore, a small amount of mixing can considerably lower temperatures in this region and consequently quench the yield. Secondary neutron ratios that are higher in the experiment than in the simulations can also be explained using the same mixing scenario. In this case, the lower temperatures result in a larger slowing down of the intermediate tritons, and the resultant higher cross section

enhances the secondary neutron yield relative to unmixed 1-D simulations. Finally, direct evidence from experiment for small-scale mixing has been obtained from plastic shells with a  $1\text{-}\mu\text{m}$  CD layer at the fuel-shell interface. With a  $^3\text{He}$  fill, proton yields from the  $\text{D}^3\text{He}$  reaction are produced only if the  $^3\text{He}$  is mixed with the deuterium from the CD layer. *LILAC* simulations with a  $^3\text{He}$  gas fill, in principle, give zero yields for these protons. A conservative estimate of the proton yield can be obtained by assuming that the  $^3\text{He}$  gas is isobarically diffused throughout the shell. The measured yields are nearly 50,000% higher than the simulation values, indicating the occurrence of small-scale mix.

The model used to describe the results presented above assumes a clean fuel region and a mixed region consisting of both fuel and shell material (Fig. 86.31). The mass of the fuel is fixed and corresponds to that of 15 atm of gas fill. Density and temperature are assumed to be constant in the clean fuel region and vary linearly in the mixed region. Further, the temperatures of the electrons and ions are assumed to be the same. This approximation can be justified since the equilibration time for electron and ion temperatures at these conditions is typically less than 5 ps. The model (Fig. 86.31) is described by six parameters (five free parameters since the mass of the fuel is known): the radius of the clean fuel region, the density of the clean region, the radius of the mixed region, the density of the shell material at the outer edge of the mix region, the temperature of the fuel in the clean region, and the temperature

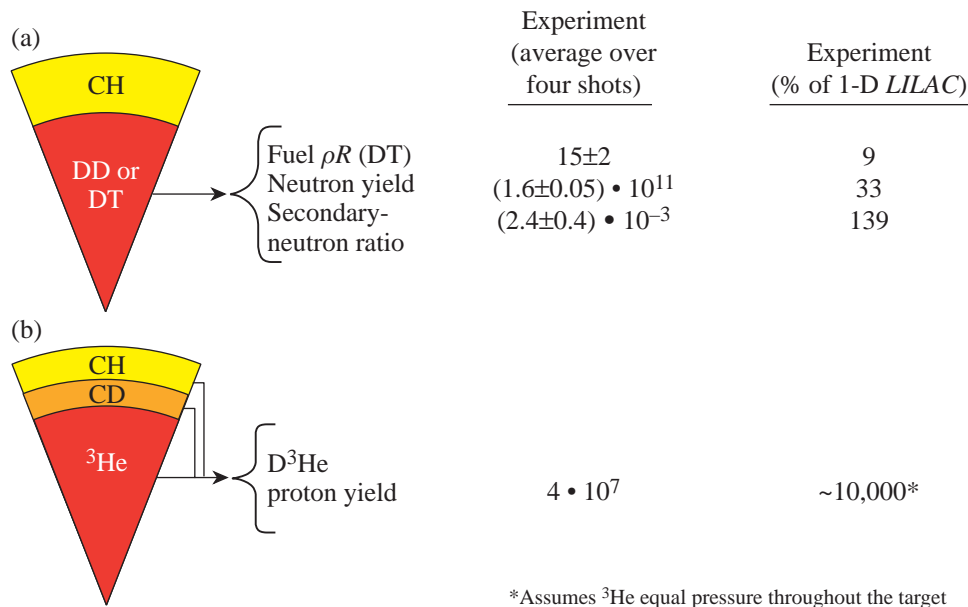


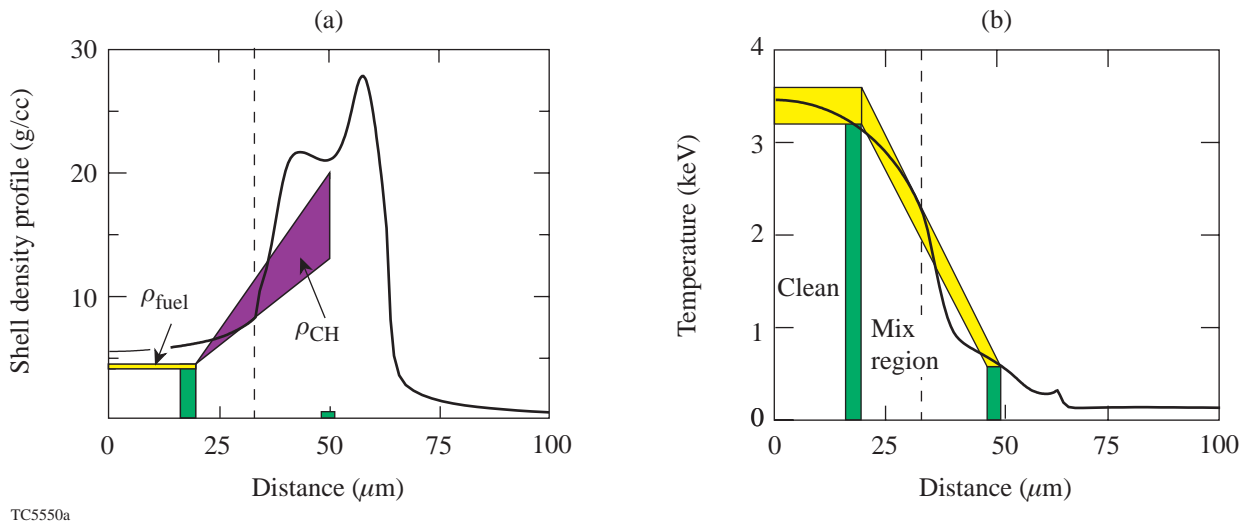
Figure 86.30  
Evidence for mixing: primary yields and secondary ratios suggest mixing of the fuel and the shell. Despite a smaller inferred fuel areal density in the experiment, the secondary neutron yield ratio is higher than in 1-D simulations. Direct evidence for mixing comes from the enhanced  $\text{D}^3\text{He}$  proton yield relative to 1-D simulations for the  $^3\text{He}$ -filled targets.

of the shell material at the outer edge of the mixed region. Operationally, using the mass and a guess for the total and clean fuel areal density, one uniquely solves for the two radii and fuel density. A guess for the shell mass in the mixed region is made, which uniquely determines the shell-density profile. The guesses for the two fuel areal densities, the shell mass, and the temperatures are varied, and for each static model the yields for the secondary neutron and proton reactions, the neutron-production rates, and the neutron-averaged ion temperatures are calculated. This is repeated until good agreement with experimental data is obtained. The yields from the  $^3\text{He}$ -filled targets are calculated using the optimal profiles and by replacing the DD or DT fuel with  $^3\text{He}$ .

Particle yields are calculated using the Monte Carlo particle-tracking code *IRIS*. *IRIS* tracks particles in straight-line trajectories on a spherically symmetric mesh. Products of primary reactions are launched based on the location of the fuel and temperature and density distributions in the target. Secondary reactions are produced along primary trajectories, and secondary trajectories in turn are launched according to the differential cross section of the reaction. The energy loss of charged particles is continuous; the trajectory is divided into smaller sections, and at the end of each section the energy of the particle is updated, accounting for its energy loss over that

section. *IRIS* runs in the so-called “embarrassingly parallel” mode on an SGI Origin 2000 machine using MPI.<sup>12</sup> In this mode an identical copy of *IRIS* is placed on each processor, and, at the end of the simulation, yields and spectra are tallied.

The optimal profiles from this parameter variation are shown in Fig. 86.31. The profiles from the corresponding *LILAC* simulation at peak particle production are also overlaid on the figure. The narrow ranges on the figure indicate the tight constraints on the model parameters. For this set of parameters, which reproduces experimental data, the fuel areal density is distributed approximately equally between the clean and mixed regions. The shell mass in the mixing region [Fig. 86.31(a)] corresponds to a 0.5- to 1- $\mu\text{m}$ -thick layer of the initial shell material mixing into the fuel region; the optimum fit occurs with about 1  $\mu\text{m}$  of mixing. This shell areal density in the mixed region is about 20% of the compressed shell areal density inferred from other diagnostics such as the energy loss of the  $\text{D}^3\text{He}$  proton from the  $\text{D}^3\text{He}$ -filled targets.<sup>4</sup> The density and temperature profiles compare very well with those from simulation, suggesting that these implosions are nearly 1-D in their compression; a small amount of mixing redistributes material near the fuel-shell interface without significantly altering the hydrodynamics of the implosion.



TC5550a

Figure 86.31

Core and fuel-shell mix density (a) and temperature (b) profiles inferred from the mix model. The range of the parameters, which is consistent with experimental observables, is shown by the width of the various parameter bands. The fuel-shell interface predicted by *LILAC* is shown as a dotted line in both. The dark solid lines represent the *LILAC*-predicted density and temperature profiles at peak neutron production.

The yields from the optimal profile are compared to experimental observables in Table 86.II. The model reproduces the experimental fuel areal densities, secondary neutron, proton ratio, and the neutron-averaged ion temperature. The time-dependent burn rate is also measured using the neutron temporal diagnostic (NTD)<sup>13</sup> in the experiment. The burn rate in this static model is less than the maximum measured burn rate. A burn width for DD-filled targets can be calculated using the experimental DD yield and the burn rate in the static model for different fills. For instance, for the <sup>3</sup>He fill in CD layer targets, this calculated burn width from DD targets is used to obtain yields from the static model. These yields are also in good agreement with the data.

Further evidence supporting this model has been obtained from recent implosion experiments on a 20- $\mu$ m CH shell with a <sup>3</sup>He gas fill and with a 1- $\mu$ m CD layer offset from the fuel-shell interface by 1  $\mu$ m. The D<sup>3</sup>He proton yields measured from this implosion are reduced significantly relative to the zero-offset CD layer implosion (preliminary proton yield  $\sim 7 \times 10^5$  compared to  $1 \times 10^7$  for the zero-offset case). The significantly lower number suggests that more than 90% of the mix-related yield is due to approximately 1  $\mu$ m of the initial shell mixing into the fuel.

Pre-existing modes at the inner surface of the plastic shell and/or feedthrough of these modes have been considered earlier as possible sources of nonuniformities during the deceleration phase of ICF implosions.<sup>14</sup> Multidimensional simulations, currently being pursued, are necessary to determine if feedthrough of the higher-order modes is significant for implosions on OMEGA and if the subsequent RT growth can account for the relatively small scales inferred from the experiments.

### Conclusions

A large set of direct-drive implosions on OMEGA has been devoted to imploding hydrodynamically similar implosions with different gas fills and shell compositions. A complementary set of diagnostics has been obtained from such implosions, allowing for a more detailed analysis of the core and mix region of these targets. A static picture of 20- $\mu$ m-thick-shell, direct-drive implosions on OMEGA has been presented. This model assumes a clean fuel region and a “mix” region where the shell material is mixed into the fuel. Excellent agreement with the suite of neutron and particle diagnostics is obtained through such a model. The model suggests that about 1  $\mu$ m of the initial shell material is mixed into the fuel during nuclear-particle production and is responsible for the observed yield ratios. The model also suggests that the fuel areal density is distributed

Table 86.II: The model reproduces many experimental observables with 1  $\mu$ m of shell material mixed into the fuel.

Fill	Shell	Parameter	Measurement	Model (% of expt)
DT	CH	Fuel $\rho R$ (mg/cm <sup>2</sup> ) (DT fill)	15 $\pm$ 2	100
		$T_{ion}$ (DT) (keV)	4.4 $\pm$ 0.4 $\pm$ 0.5 (sys)	86
D <sub>2</sub>	CH	Max: neutron burn rate (n/s)	(9 $\pm$ 1) $\times$ 10 <sup>20</sup>	110
		$T_{ion}$ (D <sub>2</sub> ) (keV)	3.7 $\pm$ 0.2 $\pm$ 0.5 (sys)	89
		Secondary neutron ratio (DD fill)	(2.4 $\pm$ 0.4) $\times$ 10 <sup>-3</sup>	100
		Secondary proton ratio (DD fill)	(1.8 $\pm$ 0.3) $\times$ 10 <sup>-3</sup>	78
<sup>3</sup> He or D <sub>2</sub>	CD CH	Secondary neutron ratio (D <sub>2</sub> fill)	(3.1 $\pm$ 0.5) $\times$ 10 <sup>-3</sup>	94
		D <sup>3</sup> He proton yield ( <sup>3</sup> He fill)	(1.3 $\pm$ 0.2) $\times$ 10 <sup>7</sup>	66
		D <sub>2</sub> neutron yield ( <sup>3</sup> He fill)	(8.5 $\pm$ 0.4) $\times$ 10 <sup>8</sup>	97

equally between the clean core and the fuel–shell mix region. The density and temperature profiles of the core and the mix region obtained from this model compare very well with those from 1-D simulations without any mixing, suggesting that the mixing in these implosions does not significantly alter the 1-D, unmixed hydrodynamics of the implosion. This work will be extended to targets with different stability characteristics such as those with thicker shells, lower fill pressures, and different laser pulse shapes. Comparisons of this model with x-ray observables will also be performed in the future.

#### ACKNOWLEDGMENT

This work was supported by the U.S. Department of Energy Office of Inertial Confinement Fusion under Cooperative Agreement No. DE-FC03-92SF19460, the University of Rochester, and the New York State Energy Research and Development Authority. The support of DOE does not constitute an endorsement by DOE of the views expressed in this article.

#### REFERENCES

1. T. R. Boehly, D. L. Brown, R. S. Craxton, R. L. Keck, J. P. Knauer, J. H. Kelly, T. J. Kessler, S. A. Kumpan, S. J. Loucks, S. A. Letzring, F. J. Marshall, R. L. McCrory, S. F. B. Morse, W. Seka, J. M. Soures, and C. P. Verdon, *Opt. Commun.* **133**, 495 (1997).
2. P. W. McKenty, V. N. Goncharov, R. P. J. Town, S. Skupsky, R. Betti, and R. L. McCrory, *Phys. Plasmas* **8**, 2315 (2001).
3. Lord Rayleigh, *Proc. London Math Soc.* **XIV**, 170 (1883); G. Taylor, *Proc. R. Soc. London Ser. A* **201**, 192 (1950); R. Betti, V. N. Goncharov, R. L. McCrory, P. Sorotokin, and C. P. Verdon, *Phys. Plasmas* **3**, 2122 (1996) (and references therein).
4. D. D. Meyerhofer, J. A. Delettrez, R. Epstein, V. Yu. Glebov, V. N. Goncharov, R. L. Keck, R. L. McCrory, P. W. McKenty, F. J. Marshall, P. B. Radha, S. P. Regan, S. Roberts, W. Seka, S. Skupsky, V. A. Smalyuk, C. Sorce, C. Stoeckl, J. M. Soures, R. P. J. Town, B. Yaakobi, J. D. Zuegel, J. Frenje, C. K. Li, R. D. Petrasso, D. G. Hicks, F. H. Séguin, K. Fletcher, S. Padalino, M. R. Freeman, N. Izumi, R. Lerche, T. W. Phillips, and T. C. Sangster, *Phys. Plasmas* **8**, 2251 (2001); see also Laboratory for Laser Energetics LLE Review **84**, 191, NTIS document No. DOE/SF/19460-371 (2000). Copies may be obtained from the National Technical Information Service, Springfield, VA 22161.
5. Laboratory for Laser Energetics LLE Review **82**, 49, NTIS document No. DOE/SF/19460-344 (2000). Copies may be obtained from the National Technical Information Service, Springfield, VA 22161.
6. E. G. Gamalii *et al.*, *JETP Lett.* **21**, 70 (1975); T. E. Blue and D. B. Harris, *Nucl. Sci. Eng.* **77**, 463 (1981); T. E. Blue *et al.*, *J. Appl. Phys.* **54**, 615 (1983).
7. V. Yu. Glebov, D. D. Meyerhofer, C. Stoeckl, and J. D. Zuegel, *Rev. Sci. Instrum.* **72**, 824 (2001).
8. F. H. Séguin, C. K. Li, D. G. Hicks, J. A. Frenje, K. M. Green, R. D. Petrasso, J. M. Soures, D. D. Meyerhofer, V. Yu. Glebov, C. Stoeckl, P. B. Radha, S. Roberts, C. Sorce, T. C. Sangster, M. D. Cable, S. Padalino, and K. Fletcher, "Using Secondary Proton Spectra to Study Imploded D<sub>2</sub>-Filled Capsules at the OMEGA Laser Facility," submitted to *Physics of Plasmas*.
9. S. Skupsky and S. Kacenjar, *J. Appl. Phys.* **52**, 2608 (1981); P. B. Radha, S. Skupsky, R. D. Petrasso, and J. M. Soures, *Phys. Plasmas* **7**, 1531 (2000).
10. C. K. Li, D. G. Hicks, F. H. Séguin, J. A. Frenje, K. Green, R. D. Petrasso, D. D. Meyerhofer, J. M. Soures, V. Yu. Glebov, P. B. Radha, S. Skupsky, C. Stoeckl, S. Roberts, and T. C. Sangster, "Study of Direct-Drive, DT-Gas-Filled-Plastic-Capsule Implosions Using Nuclear Diagnostics on OMEGA," submitted to *Physics of Plasmas*.
11. M. C. Richardson, P. W. McKenty, F. J. Marshall, C. P. Verdon, J. M. Soures, R. L. McCrory, O. Barnouin, R. S. Craxton, J. Delettrez, R. L. Hutchison, P. A. Jaanimagi, R. Keck, T. Kessler, H. Kim, S. A. Letzring, D. M. Roback, W. Seka, S. Skupsky, B. Yaakobi, S. M. Lane, and S. Prussin, in *Laser Interaction and Related Plasma Phenomena*, edited by H. Hora and G. H. Miley (Plenum Publishing, New York, 1986), Vol. 7, pp. 421–448.
12. MPI Version 1.2 Standard for IRIX—a communication language for parallel processing (Internet address: <http://www.mpi-forum.org>) (2001).
13. R. A. Lerche, D. W. Phillion, and G. L. Tietbohl, *Rev. Sci. Instrum.* **66**, 933 (1995).
14. J. Lindl, *Phys. Plasmas* **2**, 3933 (1995).

---

## High-Resolution Neutron Imaging of Laser-Imploded DT Targets

Imaging the neutrons produced by implosions at the National Ignition Facility<sup>1</sup> or the Laser Mega Joule<sup>2</sup> will require spatial resolution as good as  $5\ \mu\text{m}$  (Ref. 3) to identify failure mechanisms such as poor implosion symmetry or improper laser pulse shaping. An important step to achieving this goal is reported in this article. Neutron images were obtained from OMEGA implosions with both high resolution and narrow diameters that confirm the resolution and agree with calculations. Ress *et al.*<sup>4</sup> obtained the first neutron images of ICF capsules with a geometric resolution of  $80\ \mu\text{m}$  and a full width at half-maximum (FWHM) of  $150\ \mu\text{m}$ . Delage *et al.*<sup>5</sup> reported geometrical resolution of  $56\ \mu\text{m}$  and overall resolutions of 100 to  $180\ \mu\text{m}$  with FWHM's of 150 to  $250\ \mu\text{m}$ . The measurements reported in this article [carried out on LLE's OMEGA laser by a team of scientists from Commissariat à l'Énergie Atomique (CEA), LLE, and LANL] achieved a geometrical resolution of  $30\ \mu\text{m}$  and an overall resolution of  $45\ \mu\text{m}$  with a FWHM of  $62\ \mu\text{m}$ .

Imaging neutrons at high resolution is a challenging task being carried out at several laboratories using pinhole<sup>6</sup> or penumbral apertures. CEA's experimental system using the penumbral technique,<sup>7</sup> as well as a new analytical approach for estimating the overall resolution, was successfully tested on OMEGA in a direct-drive experiment. The basis of the design is to use an aperture whose diameter is large compared to the size of the neutron source. The shape of the aperture is biconical and is optimized in order to amplify the penumbra of the source in the image plane. The aperture is larger than that for a pinhole, allowing easier fabrication and stronger signals, especially important when signal levels are low. An unfolding process is needed, however, to recover an image; this process includes low bandpass filtering, which affects the resolution. This article reviews the main mechanisms that limit the spatial resolution of a penumbral imaging system: the spatial resolution of the detector, the shape of the aperture, and the process of unfolding the image.

After propagating through the experimental chamber and target area and scattering from various experimental hardware

and structures, the 14-MeV neutrons arriving at the detector are spread in time and angle. Moreover, these neutrons create a large number of gamma rays in the 0- to 10-MeV range by  $(n, \gamma)$  reactions on the experimental hardware. The direct neutrons that form the image need to be discriminated from the scattered neutrons and the gamma rays. Bubble detectors<sup>8</sup> can discriminate among gamma rays, low-energy neutrons, and 14-MeV neutrons. They offer potentially high spatial resolution, but their efficiency is still very low ( $1.4 \times 10^{-5}$ ) and they require a sophisticated readout system.

Plastic scintillators with response times of the order of 10 ns can discriminate particles by arrival time. The detector contains 8000 scintillating fibers, each with a length of 10 cm, a square section of  $1.5\ \text{mm}^2$ , and an  $e$ -fold decay time of 12 ns. The intrinsic detection efficiency  $\varepsilon$  is 27%. The sampling theorem limits the spatial resolution of the instrument to a geometrical resolution of  $2\delta_{\text{pix}}/G$ , where  $G$  is the magnification ratio of the system and  $\delta_{\text{pix}}$  is the pixel size.

In a plastic scintillator, fast neutrons interact mainly by elastic scattering on hydrogen. The high-energy protons lose energy in the medium (calculated with the Birks model<sup>9</sup>) and produce light about the scattering point with a FWHM of  $0.910\ \text{mm}$  ( $\delta_{\text{rec}}$ ).<sup>10</sup> This limits the resolution of the system to  $\delta_{\text{rec}}/G$ . This intrinsic limitation required a high magnification ratio to achieve a high-resolution design.

The image is relayed optically by a mirror and a lens from the detector onto a gated microchannel plate (MCP); the output image of the MCP is reduced by a fiber-optics taper and then recorded on a charge-coupled device (CCD) with a  $19\text{-}\mu\text{m}$  pixel size. The CCD is shielded by a 25-cm-thick piece of plastic followed by 5 cm of lead. At 8 m from the source, the external dose of 12 mrad for a  $10^{14}$  neutron yield is reduced to several mrad inside the shield (an upper acceptable limit for the CCD). The detector image size is reduced to 0.27 and 0.068 of its original dimension onto the MCP and the CCD, respectively. Each fiber of the detector is recorded on the average onto a 5-by-5 array of CCD pixels. The spatial resolution of the

MCP is  $70 \mu\text{m}$  at FWHM, much smaller than the size of the detector pixel imaged onto the MCP ( $405 \mu\text{m}$ ). We conclude that the spatial resolution of our recording system is negligible compared to the spatial resolution of the detector.

The point-spread function (PSF) of the aperture is the neutron intensity distribution in the image plane for an isotropic point source located in the middle of the field of view. For a given entrance hole diameter, this PSF depends only on the field of view and the distance from the source. Figure 86.32 shows dependence of the FWHM ( $\delta_{\text{bic}}$ ) of the PSF on the distance from the middle of the aperture to the target ( $L_0$ ). Increasing the distance from the source to the aperture can improve the spatial resolution to less than  $10 \mu\text{m}$ . For these experiments, however, the magnification ratio decreases with  $L_0$  because the distance between the source and the scintillator ( $L_i$ ) is limited to 8 m. An optimal value for  $L_0$ , including the resolution of the detector, is found to be 80 mm.

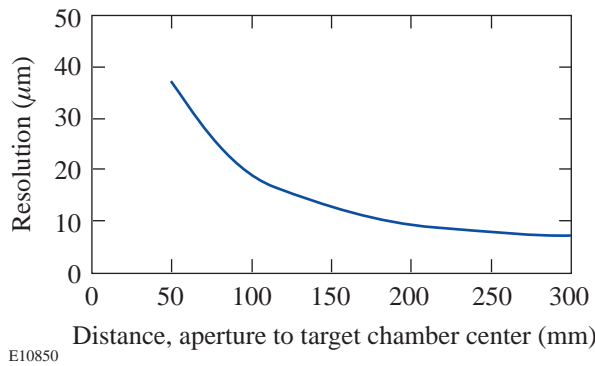


Figure 86.32

The spatial resolution limit (FWHM of the point-spread function) for the biconical aperture versus the distance ( $L_0$ ) from its center to the source.

A hole was recently dug in the concrete floor of the OMEGA Target Bay to allow a 13-m line of sight. A new detector will be installed with  $250\text{-}\mu\text{m}$ -diam capillaries filled with deuterated liquid scintillator. The new  $250\text{-}\mu\text{m}$  pixel size and estimated  $\delta_{\text{rec}}$  of  $500 \mu\text{m}$  lead to a redesigned aperture placed at  $L_0 = 160$  mm. These modifications should reduce the noise background by a factor of 100 and allow a  $13\text{-}\mu\text{m}$  resolution.

Several methods exist to unfold penumbral images.<sup>11</sup> After testing these methods on synthetic penumbral images, the autocorrelation method<sup>12</sup> was found to give the best results with minimum mathematical complexity. Most penumbral unfolding processes assume that the aperture can be repre-

sented by a thin hole of radius  $R_d$  surrounded by a medium with a transmission  $\tau$  to neutrons. With this assumption, the Fourier transform  $I$  of the image is the product of the Fourier transform  $S$  of the source and the aperture:  $I(k) = S J_1(2\pi k R_d) / \pi k R_d$ , where  $J_1$  is the first-order Bessel function. The unfolding process consists of multiplying  $I$  by a function  $U$ , which has the following mathematical properties: inverse Fourier transform  $[U J_1(2\pi k R_d) / \pi k R_d] = \delta$ , the Dirac function, and a small amplitude oscillatory function at radius  $2R_d$ , which is outside the field of view. We find  $U = 2J_1(2\pi k R_d) k^3 / \pi k R_d$ . The multiplication of  $I$  by  $U$  gives the Fourier transform of the source image, avoiding any problems caused by dividing by zero.

In practice, the unfolded Fourier transform of the image contains both noise and the signal from the spatial distribution of the neutron source. The primary source of noise is the Poisson statistics of events in the detector. Reducing this noise requires a low band-pass filtration that limits overall design performance. A reliable criterion to find the frequency at which noise starts to dominate is to set the noise power spectrum equal to the power spectrum of the signal without noise.<sup>13</sup>

For Poisson noise, it can be shown that the power spectrum of the image with noise,  $P_{s+n}$ , is the sum of the power spectrum of the image without noise,  $P_s$ , and the spectrum  $N_s$  of the number of detected neutrons in the full field of the image.<sup>14</sup> For an homogeneous neutron source of radius  $R_s$  and yield  $N$ , we have

$$N_s = \frac{\epsilon N G^2}{4(L_i + L_0)^2} \left[ (1 - \tau) R_d^2 + \tau (R_d + R_s)^2 \right],$$

$$P_s = \left[ \frac{\epsilon (1 - \tau) N R_d^2 G^2}{4(L_i + L_0)^2} \frac{J_1(2\pi k R_d)}{\pi k R_d} \frac{J_1(2\pi k R_s)}{\pi k R_s} \right]^2.$$

Using the first-order approximation of the Bessel function valid for  $k R_{d,s}$  greater than about 1.2 (appropriate for penumbral imaging), the equation  $P_s = N_s$  gives the cutoff frequency  $k_c$ :

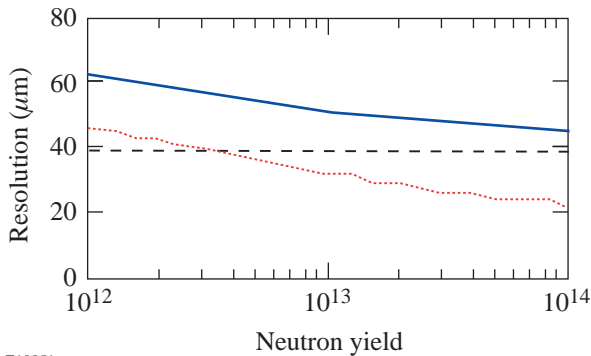
$$k_c = \frac{1}{\pi} \sqrt[6]{\frac{\epsilon N G^2}{4\pi(L_i + L_0)} \frac{(1 - \tau)^2}{\left[ (1 - \tau) R_d^2 + \tau (R_d + R_s)^2 \right]} \frac{R_d}{\pi R_s^3}}. \quad (1)$$

The spatial spectrum of the signal beyond the cutoff frequency is within one standard deviation of the noise. Recovering signal information beyond  $k_c$  requires sophisticated filtering.<sup>12</sup> In our design,  $1/k_c$  is used as a preliminary estimation of the limit of spatial resolution due to the signal-to-noise ratio and the unfolding process.

Combining the effects of statistics on resolution, the shape of the aperture, the pixel size, and the recoil proton range leads to an estimation of the overall spatial resolution  $\delta_s$ :

$$\delta_s = \sqrt{\frac{1}{k_c^2} + \delta_{\text{bic}}^2 + \left(\frac{2\delta_{\text{pix}}}{G}\right)^2 + \left(\frac{\delta_{\text{rec}}}{G}\right)^2}. \quad (2)$$

Figure 86.33 shows the variation of the overall spatial resolution for neutron yield between  $10^{12}$  and  $10^{14}$  and for a neutron source size of  $50\text{-}\mu\text{m}$  diameter. For a high-yield shot, the spatial resolution is  $45\text{ }\mu\text{m}$ , dominated by the sampling limit ( $30\text{ }\mu\text{m}$ ) and the PSF of the aperture ( $24\text{ }\mu\text{m}$ ) (dotted curve of Fig. 86.33). The design is unable to resolve spatial variation of such a source because the resolution and the source size are comparable. A neutron source size of  $100\text{-}\mu\text{m}$  diameter, however, can be differentiated from one of  $50\text{ }\mu\text{m}$ .



E10851  
 Figure 86.33  
 The instrument’s contributions to the spatial resolution versus the neutron yield; overall resolution (solid), spatial resolution limit due to the cutoff frequency  $k_c$  (dashed) for a  $50\text{-}\mu\text{m}$ -diam neutron source, and spatial resolution limit (dotted).

Correct alignment is crucial to the experiment. A straight reference line is established between a  $400\text{-}\mu\text{m}$ -diam, back-lighted sphere at target chamber center and an autocollimator near the detector. The penumbral aperture axis is made colinear to an accuracy of  $0.1\text{ mrad}$  using an attached, prealigned half reflecting plate. The aperture is then centered on the back-

lighted sphere to an accuracy of  $50\text{ }\mu\text{m}$ . The alignment procedure takes at least 2 h for a trained experimentalist to complete.

Several operations are conducted on the raw penumbral image before it is unfolded. First, the average of the CCD backgrounds before and after the shot is subtracted. Then CCD pixels in which neutrons or gamma rays have interacted directly are detected by amplitude discrimination and replaced by the average value of the neighboring pixels. This eliminates CCD pixels that have values more than three times higher than the standard variation of the local average signal; however, CCD pixels where neutrons or gamma rays have created comparable or lower levels than the signal coming from the scintillator still remain. Several shots are also acquired without the aperture. The average of these images is used to correct the image for the spatial variation of the response of the detector and the recording system.

Figure 86.34 shows an unfolded image; Figs. 86.35 and 86.36 show the profiles obtained from the implosions (shots 21054 and 20290) of two glass microballoons filled with 20 atm of DT driven by 1-ns square laser pulses. The shells had thicknesses of  $4.2\text{ }\mu\text{m}$  and  $2.5\text{ }\mu\text{m}$ , diameters of  $890\text{ }\mu\text{m}$  and  $920\text{ }\mu\text{m}$ , and laser energies of 23.1 kJ and 31.1 kJ; they produced yields of 3.6 and  $6 \times 10^{13}$  neutrons, with measured ion temperatures of 10.3 and  $\sim 9\text{ keV}$ . The FWHM of the measured neutron source sizes is  $62\text{ }\mu\text{m}$  (21054) and  $78\text{ }\mu\text{m}$  (20290), respectively. The filter processing limits the minimum detail that can be resolved to  $45\text{ }\mu\text{m}$  for shot 21054 and

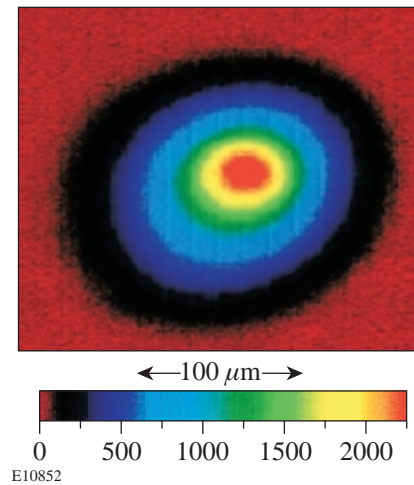
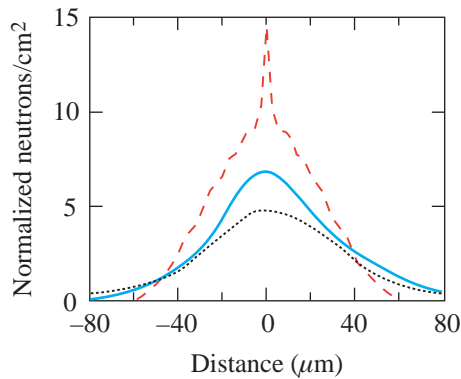


Figure 86.34  
 Unfolded image of shot 21054 showing a slight asymmetry.

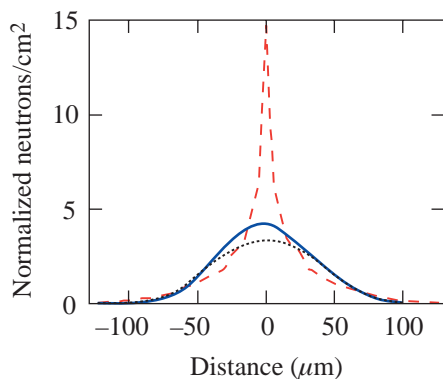
53  $\mu\text{m}$  for shot 20290. These values are in agreement with the expected performance calculated with Eq. (2) (see Fig. 86.33). For comparable neutron yield, the diagnostic resolution performance is better when the source size is smaller, as predicted by Eq. (1).

One-dimensional calculations of these implosions with a radiation-hydrodynamic code<sup>15</sup> were postprocessed using a neutron transport code to produce the calculated neutron image profiles shown in Figs. 86.35 and 86.36. These images were then processed to include the effects of noise by first calculat-



E10853

Figure 86.35  
Horizontal lineout (solid) of a DT capsule with a 4.2- $\mu\text{m}$ -thick glass shell (shot 21054) compared to calculated profiles without (dashed) and with (dotted) the effects of experimental noise.



E10854

Figure 86.36  
Horizontal lineout (solid) of a DT capsule with a 2.5- $\mu\text{m}$ -thick  $\text{SiO}_2$  glass shell (shot 20290) compared to calculated profiles without (dashed) and with (dotted) the effects of experimental noise.

ing a simulated penumbral image, then adding Poisson noise at the level seen in the experiments, and finally deconvolving and smoothing using the same process as used for the data. The resulting profiles in both cases are within the experimental resolution of the observed profiles (all profiles are normalized in 2-D to the same integral). The implosion of the capsule with a 4.2- $\mu\text{m}$ -thick wall had a calculated convergence ratio (initial fuel radius/final fuel radius) of 9, producing the smaller source. The implosion of the capsule with a 2- $\mu\text{m}$ -thick wall was very similar to that of Ress *et al.*<sup>4</sup> (capsule with a 2- $\mu\text{m}$  wall, 1000- $\mu\text{m}$  diameter, 25 atm DT, 20-kJ laser energy, 1-ns square pulse, convergence ratio of  $<3$ , neutron yield of  $\sim 10^{13}$ , and a 9-keV ion temperature). Both capsules were calculated to produce an image with a strong central peak. We find that the inclusion of instrumental resolution, which Ress *et al.*<sup>4</sup> did not address, explains the lack of an observed peak in our data. Our smaller observed FWHM of 78  $\mu\text{m}$  compared to their 150  $\mu\text{m}$  reflects the higher resolution of our imaging system as well as the better irradiation symmetry of OMEGA's 60 beams compared to Nova's 10 beams.

#### ACKNOWLEDGMENT

We would like to acknowledge the assistance of the OMEGA laser team in executing these experiments, and General Atomics and Los Alamos National Laboratory for fabricating and filling the DT capsules. These experiments were carried out in collaboration and participation of many people, including R. Fisher at General Atomics; S. Chiche, Ph. Millier, C. Ducrocq, C. Labbe, R. Debure, M. C. Monteil, B. Canaud, X. Fortin, and N. Dague at Bruyères le Châtel; S. J. Loucks, J. Mathers, G. Pien, J. Armstrong, and D. D. Meyerhofer at LLE; G. Morgan, F. Cverna, J. Faulkner, M. Wilke, T. Murphy, and C. Barnes at Los Alamos; R. A. Lerche, C. Sangster, and M. Cable at Lawrence Livermore National Laboratory. This work was funded by the Commissariat à l'Énergie Atomique, France, and the US Department of Energy.

#### REFERENCES

1. J. Paisner *et al.*, *Laser Focus World* **30**, 75 (1994).
2. P. A. Holstein *et al.*, *Laser Part. Beams* **17**, 403 (1999).
3. S. M. Pollaine *et al.*, *Phys. Plasmas* **8**, 2357 (2001).
4. D. Ress *et al.*, *Science* **241**, 956 (1988).
5. O. Delage *et al.*, *Rev. Sci. Instrum.* **66**, 1205 (1995).
6. G. L. Morgan *et al.*, *Rev. Sci. Instrum.* **72**, 865 (2001).
7. J. P. Garçonnet *et al.*, *Laser Part. Beams* **12**, 563 (1994); R. A. Lerche *et al.*, *Laser Part. Beams* **9**, 99 (1991).
8. R. K. Fisher *et al.*, *Rev. Sci. Instrum.* **72**, 796 (2001).

9. J. Birks and D. Fry, *Theory and Practice of Scintillation Counting*, International Series of Monographs in Electronics Instrumentation, Vol. 27 (Pergamon Press, New York, 1964).
10. G. Mosinski and B. Roy, CEA Bruyères le Châtel, Report No. 79/DR 83 (1983).
11. K. A. Nugent and B. Luther-Davies, *Opt. Commun.* **49**, 393 (1984).
12. A. Rouyer, "Unfolding Neutron Penumbral Images Using an Autocorrelation Technique," submitted to *Physical Review Letters*.
13. J. S. Beis, A. Celler, and J. S. Barney, *IEEE Trans. Nucl. Sci.* **42**, 2250 (1995).
14. J. W. Goodman and J. F. Belsher, in *Imaging Through the Atmosphere*, edited by J. C. Wyant (SPIE, Bellingham, WA, 1976), Vol. 75, pp. 141–154.
15. G. B. Zimmerman and W. L. Kruer, *Comments Plasma Phys. Control. Fusion* **2**, 51 (1975).

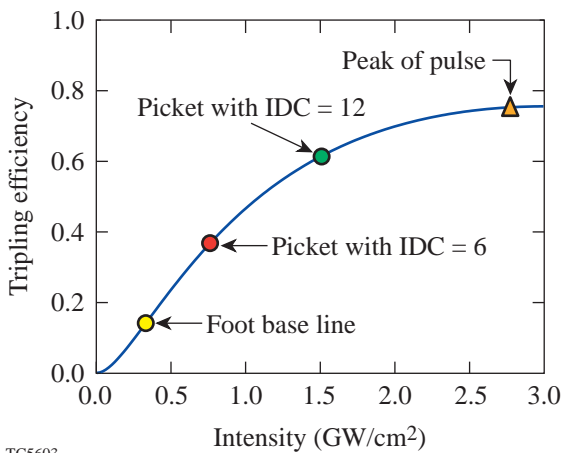
# The Smoothing Performance of Ultrafast Pickets on the NIF

## Introduction

In the direct-drive approach to inertial confinement fusion (ICF), the focal spots of a symmetrically arranged cluster of high-intensity, ultraviolet (UV) laser beams directly irradiate a capsule.<sup>1,2</sup> The base-line design for a direct-drive ignition target on the National Ignition Facility (NIF) uses shock preheat to control the isentrope of the ablation surface and the fuel. Control of the isentrope  $\alpha$  (where  $\alpha$  is the ratio of the fuel pressure to the Fermi-degenerate pressure) is achieved by changing the laser pulse shape. The UV pulse shape corresponding to  $\alpha = 3$  is chosen for the base-line design. This shape can be logically divided into two regions: a low-intensity “foot” (of duration  $\sim 4.2$  ns) followed by a high-intensity “drive” (duration  $\sim 5$  ns). This pulse shape represents a compromise that provides a certain safety margin for the implosion by reducing the target’s sensitivity to laser nonuniformity by ensuring that the target will remain intact during the drive portion of the pulse; however, laser nonuniformity still re-

mains an important issue. The laser irradiation nonuniformity seeds the Rayleigh–Taylor hydrodynamic instability, which consequently degrades target performance.<sup>3,4</sup>

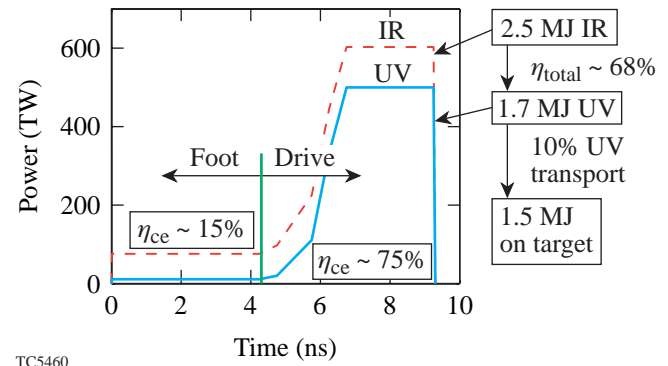
The energy efficiency of the KDP frequency-conversion crystals used in ICF lasers is a function of input intensity; efficiency increases as the third power of input intensity increases until saturation occurs (see Fig. 86.37). Consequently, the low-intensity foot portion of the pulse converts inefficiently and can represent a substantial overall reduction in the laser’s energy efficiency. As shown in Fig. 86.38, an  $\alpha = 3$ , direct-drive pulse has a total infrared (IR) energy of 2.5 MJ and a total UV energy delivered to target of 1.5 MJ (including 10% UV transport losses). The frequency-conversion efficiency in the foot of the  $\alpha = 3$  pulse is  $\sim 15\%$  and  $\sim 75\%$  in the drive portion, yielding an overall efficiency of  $\sim 68\%$ . This issue is even more problematic for the indirect-drive approach, where the overall conversion efficiency is as low as



TC5603

Figure 86.37

The IR to UV frequency-conversion-efficiency curve for the NIF. The drive portions of an  $\alpha = 3$  ICF pulse converts at efficiencies around 75%, where the efficiency is in saturation. The foot portion of the ICF pulse converts at a low efficiency of 15%. In addition, the frequency-conversion efficiency exhibits a third-power dependence for low-IR input intensity. This exacerbates any beam-to-beam power imbalance during the foot portion of an  $\alpha = 3$  ICF pulse.



TC5460

Figure 86.38

The  $\alpha = 3$ , direct-drive ICF pulse, which is logically divided into two regions: a low-intensity “foot” (about 4.2 ns) followed by a high-intensity “drive” (about 5 ns). The IR power as a function of time (dashed line) required to produce the desired UV power onto target (solid line). The total IR energy is 2.5 MJ, and the total UV energy delivered to target (accounting for 10% UV transport losses) is 1.5 MJ. The frequency-conversion efficiency is  $\sim 15\%$  in the foot and  $\sim 75\%$  in the drive, which yields an overall efficiency of  $\sim 68\%$ .

50% due to a much longer low-intensity foot.<sup>5</sup> Beam-to-beam power imbalance is also exacerbated for the low-intensity foot because of the third-power dependence of conversion efficiency on intensity at low intensities; during the drive portion of the ICF pulse the conversion efficiency is in saturation at  $\sim 75\%$  and does not contribute significantly to beam-to-beam power imbalance.

Ultrafast picket-fence pulses were proposed by Rothenberg<sup>5</sup> as a way to maximize conversion efficiency and minimize beam-to-beam power imbalance. In this article, we consider the application of the ultrafast pickets only to the foot portion of the  $\alpha = 3$  pulse. We assume that the pickets are temporally blended into the drive portion of the pulse. Ultrafast pickets consist of a train of laser pulses with an inverse duty cycle (IDC), which is defined as the ratio of the pulse-repetition period to the pulse width, chosen to maintain near-constant target illumination and a peak intensity that delivers the same average power to the target as when picket-fence modulation is absent. For example, if a pulse train of 20-ps pulses with  $\text{IDC} = 6$  is applied to the foot, the peak intensity of each picket can be increased sixfold while maintaining the same average power on target. Increasing the peak intensity sixfold boosts the conversion efficiency of the foot from 15% to 39% and the overall efficiency from 68% to 73% (see Fig. 86.39). (For indirect drive the overall conversion efficiency can be increased from  $\sim 50\%$  to  $\sim 72\%$  by using ultrafast pickets.<sup>5</sup>) For a pulse train of 10-ps pulse with  $\text{IDC} = 12$ , the efficiency of the foot is increased to 51% with an overall efficiency of 74%. The benefit of this shorter pulse is the minimized affect on beam-to-beam power imbalance as seen in Fig. 86.37.

The goal of this investigation is to assess the impact and benefits of implementing ultrafast pickets for direct-drive capsules on the NIF. The smoothing performance (defined as the time-integrated laser nonuniformity as a function of time) is the metric used to compare the ultrafast-picket-fence scheme to that of base-line 2-D SSD on the NIF. Various beam-smoothing techniques to be employed on the NIF are similar to those employed on the OMEGA<sup>6,7</sup> laser to improve on-target laser uniformity, which reduces laser imprint. These techniques include two-dimensional smoothing by spectral dispersion (2-D SSD),<sup>8–10</sup> distributed phase plates (DPP's),<sup>11,12</sup> polarization smoothing,<sup>6,13,14</sup> and multiple-beam overlap.

The code *Waaikwa*'<sup>15</sup> is used to calculate the time evolution of the far field and the single-beam time-integrated laser nonuniformity for the first 3 ns of the foot. *Waaikwa*' will be

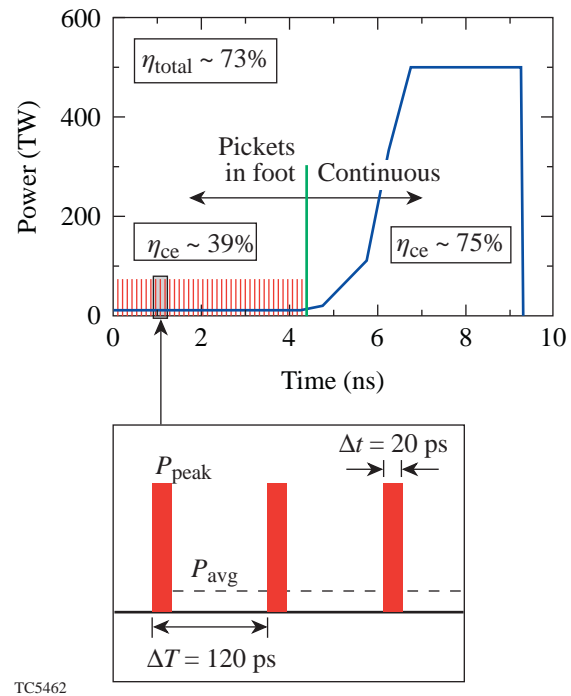


Figure 86.39

The UV power of an  $\alpha = 3$ , direct-drive pulse with ultrafast pickets applied during the foot. The frequency-conversion efficiency has been increased in the foot from 15% to  $\sim 39\%$ , which yields an overall efficiency of  $\sim 73\%$ .

used under a variety of near-field conditions that describe the base-line 2-D SSD system as well as various ultrafast-picket configurations. The calculated single-beam, time-dependent, laser nonuniformity will be used as the basis of comparison.

In the following sections we describe the base-line 2-D SSD system, the generation of an ultrafast picket pulse train, the far-field characteristics of ultrafast pickets, the smoothing performance, and conclusions.

### Base-Line 2-D SSD

The 2-D SSD system on the NIF is similar to that on OMEGA with one exception: only one grating is used in the first SSD dimension on the NIF because it is implemented with a fiber-optic-based phase modulator. As a result, the beam suffers a residual time shear. OMEGA utilizes a bulk phase modulator in the first dimension so it can precompensate for this shear (compare Ref. 16). The second SSD dimension on the NIF has two gratings, like OMEGA. A schematic of the NIF's 2-D SSD design is shown in Fig. 86.40.

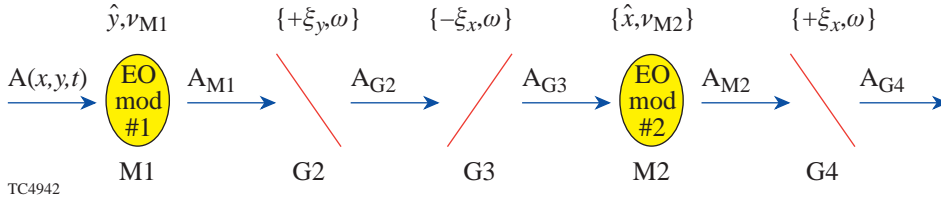


Figure 86.40

A schematic representation of the NIF's 2-D SSD system. Notice that the first dimension has only one grating, which causes a residual temporal shear across the beam.

The spatiotemporal evolution the complex-valued UV electric field of a 2-D SSD pulsed beam can be expressed as

$$E(x, y, t) \equiv E_0(x, y, t) e^{i\phi_{2\text{-D SSD}}(x, y, t)} e^{i\phi_{\text{DPP}}(x, y)}, \quad (1)$$

where  $E_0(x, y, t)$  defines the electric field's pulse and beam shape,  $\phi_{2\text{-D SSD}}$  is the 2-D SSD phase contribution, and  $\phi_{\text{DPP}}(x, y)$  is the static DPP phase contribution. The mapping of the DPP phase contribution was designed to yield a far-field intensity distribution of an eighth-order super-Gaussian with a 95% enclosed energy contour of 3.40-mm diameter in the target plane. For these simulations, the fundamental spatial and temporal shapes of the pulsed beam are assumed to be separable prior to the 2-D SSD operation. The uncompensated grating operation distorts this fundamental shape and can be written as

$$E_0(x, y, t) \equiv G\{\text{beam}(x, y) \cdot \text{pulse}(t)\}, \quad (2)$$

where  $\text{beam}(x, y)$  is the near-field beam shape,  $\text{pulse}(t)$  is the temporal pulse shape, and  $G\{\bullet\}$  represents an uncompensated grating operator, which is defined by

$$G\{f(x, y, t)\} \equiv f(x, y, \zeta), \quad (3)$$

where the spatially coupled time domain is given by  $\zeta \equiv t - \xi_y y$  and  $\xi_y$  is the angular grating dispersion (see Ref. 16 for a detailed examination of the angular spectrum representation of the 2-D SSD operation). As a consequence of the assumed separability, the uncompensated grating operation couples the temporal pulse shape to the spatial dimension corresponding to the first SSD dimension while the spatial beam shape remains unaltered and is given by

$$E_0(x, y, t) \equiv \text{beam}(x, y) \cdot \text{pulse}(t - \xi_y y). \quad (4)$$

For the *Waasikwa*' simulations the fundamental beam shape at the final magnification is defined as a square-shaped 20th-order super-Gaussian:

$$\begin{aligned} \text{beam}(x, y) \equiv & \exp\left[-\ln(2)\left(\frac{|x|}{30.8 \text{ cm}}\right)^{20}\right] \\ & \times \exp\left[-\ln(2)\left(\frac{|y|}{30.8 \text{ cm}}\right)^{20}\right], \quad (5) \end{aligned}$$

which has an intensity full-width half-maximum (FWHM) width in each direction of  $D_{\text{FWHM}} = 30.8 \text{ cm}$  and a 95% enclosed energy contour with a width in each direction of  $D_{\text{NIF}} = 35.1 \text{ cm}$ , and the fundamental pulse shape is given by a fourth-order super-Gaussian to a "flat-top":

$$\text{pulse}(t) \equiv \begin{cases} \exp\left[-\ln(2)\left(\frac{t-t_0}{19 \text{ ps}}\right)^4\right]; & 0 < t \leq t_{\text{peak}} \\ 1 & ; t > t_{\text{peak}} \end{cases}, \quad (6)$$

where the quantity  $t_0$  is defined to yield a nominally, small initial value for the pulse, e.g.,  $\text{pulse}(0) = 0.001$ , and the quantity  $t_{\text{peak}}$  defines the time when the pulse shape achieves a value of unity, i.e.,  $\text{pulse}(t_{\text{peak}}) = 1$ . The foot pulse is defined in this manner to make a more accurate comparison of the early development of the nonuniformity with the ultrafast pickets defined later.

The spatially and temporally varying phase due to 2-D SSD is given by (see Ref. 16)

$$\begin{aligned} \phi_{2\text{-D SSD}}(x, y, t) \equiv & 3\delta_{\text{M1}} \sin[\omega_{\text{M1}}(t + \xi_y y)] \\ & + 3\delta_{\text{M2}} \sin[\omega_{\text{M2}}(t + \xi_x x)], \quad (7) \end{aligned}$$

where  $\delta_{M1}$  is the first-dimension modulation depth,  $\nu_{M1} \equiv \omega_{M1}/(2\pi)$  is the first-dimension microwave or radio frequency (RF) modulation frequency,  $\xi_y$  is the first-dimension angular grating dispersion,  $\delta_{M2}$  is the second-dimension modulation depth,  $\nu_{M2} \equiv \omega_{M2}/(2\pi)$  is the second-dimension RF modulation frequency, and  $\xi_x$  is the second-dimension angular grating dispersion. The factor of 3 in Eq. (7) indicates that the electric field has undergone frequency tripling from the IR to UV. The relevant NIF 2-D SSD base-line system parameters are assumed to be  $\delta_{M1} = 16.7$ ,  $\nu_{M1} = 8.76$  GHz,  $\xi_y = 0.325$  ns/m,  $\Delta\lambda_{M1} = 10.8$  Å,  $\delta_{M2} = 8.37$ ,  $\nu_{M2} = 3.23$  GHz,  $\xi_x = 0.878$  ns/m, and  $\Delta\lambda_{M2} = 2.0$  Å, assuming a nominal beam diameter of  $D_{NIF} = 35.1$  cm.

The base-line 2-D SSD design for direct-drive NIF is defined in this article as having IR bandwidths of

$$\Delta\lambda_{M1} = 2\delta_{M1}\nu_{M1}\lambda_{IR}^2/c = 10.8 \text{ Å}$$

and

$$\Delta\lambda_{M2} = 2\delta_{M2}\nu_{M2}\lambda_{IR}^2/c = 2.0 \text{ Å}$$

in the first and second dimensions, respectively, where  $c$  is the vacuum speed of light and  $\lambda_{IR} = 1053$  nm is the IR wavelength. Two different measures of combined UV bandwidth or widths of the temporal power spectrum are used here: the first measure is the root-sum-square and is defined by

$$\Delta\nu_{\text{rss}} = \sqrt{\Delta\nu_{M1}^2 + \Delta\nu_{M2}^2}, \quad (8)$$

where the UV bandwidths of each modulator are given separately by  $\Delta\nu_{M1} \equiv 6\delta_{M1}\nu_{M1}$  and  $\Delta\nu_{M2} \equiv 6\delta_{M2}\nu_{M2}$ ; and the second measure is known as the autocorrelation width<sup>17</sup> and is defined by

$$\Delta\nu_{\text{eff}} = \frac{\left| \int \tilde{I}(v) dv \right|^2}{\int \tilde{I}(v)^2 dv}, \quad (9)$$

where the quantity  $\tilde{I}(v) \equiv |\tilde{E}(v)|^2$  represents the smoothed envelope of the temporal power spectrum due to the 2-D SSD phase modulation  $\phi_{2-D}$  SSD. The base-line 2-D SSD system yields  $\Delta\nu_{\text{rss}} = 891$  THz and  $\Delta\nu_{\text{eff}} = 979$  THz in the UV.

The bandwidth  $\Delta\lambda_M$ , laser divergence  $\Delta\theta_M$  and the number of color cycles  $N_{\text{cc}}$  determine the required grating dispersion  $\xi$ , the temporal delay  $\tau_D$ , modulator frequency  $\nu_M$ , and modula-

tion depth  $\delta_M$  for the given beam diameter  $D_{NIF}$ . Due to current pinhole requirements of the spatial filters, the imposed laser divergence is limited to  $\Delta\theta_{M1} = 100$   $\mu$ rad and  $\Delta\theta_{M2} = 50$   $\mu$ rad in the first and second dimensions, respectively. The number of color cycles across the beam is defined by  $N_{\text{cc}} \equiv \tau_D\nu_M$ , where  $\tau_D$  is the time shear imposed by the dispersion gratings and  $\nu_M$  is the modulator's frequency. It can be shown that the laser divergence  $\Delta\theta_M$  is proportional to the applied SSD bandwidth  $\Delta\lambda_M$  and is given by

$$\Delta\theta_M = \tau_D \Delta\lambda_M \frac{c}{\lambda_{IR} D_{NIF}}, \quad (10)$$

where  $c$  is the vacuum speed of light,  $\lambda_{IR} = 1053$  nm is the IR vacuum wavelength, and  $D_{NIF} = 35.1$  cm is the nominal beam diameter. Since the pinholes restrict the laser divergence  $\Delta\theta_M$ , and the base-line 2-D SSD design calls for  $\Delta\lambda_{M1} = 10.8$  Å, applying Eq. (10) to the first dimension yields a time delay  $\tau_{D1} = 114.15$  ps, which implies that the required modulator frequency for the first dimension, to achieve  $N_{\text{cc}1} = 1$ , is  $\nu_{M1} = 8.76$  GHz. Similarly, applying Eq. (10) to the second dimension yields  $\tau_{D2} = 309.60$  ps and  $\nu_{M2} = 3.23$  GHz for  $N_{\text{cc}2} = 1$ . This base-line design will be designated as BL1 in this article. An alternative base-line 2-D SSD design, designated as BL2, is also proposed, which has  $N_{\text{cc}1} = 2$ ,  $\delta_{M1} = 8.33$ , and  $\nu_{M1} = 17.52$  GHz with all other parameters left the same. In addition, a base-line design the same as BL1 but without the temporal shear will be designated as BL1b. The relevant parameters are summarized in Table 86.III.

### Ultrafast-Picket-Smoothing Scheme

The ultrafast-picket-smoothing scheme produces a sub-apertured near field that sweeps across the full-beam aperture when using a pulse-modulated laser whose pulse width is smaller than the residual time shear  $\tau_{D1}$  due to the dispersing grating. The sweeping motion causes smoothing in the time-integrated far field because the speckle pattern changes as the sub-apertured near field moves across the randomly phased background of the DPP. Applying a time-varying phase or phase chirp to each picket enhances the efficiency of this smoothing mechanism. The phase chirp increases the inherent bandwidth of each pulse and asymptotically produces many independent speckle patterns (or far-field modes), similar to SSD, as long as the grating dispersion matches the pulse repetition rate. Unlike SSD, the phase chirp can be tailored to produce a uniform far-field distribution of modes that not only reduces the asymptotic nonuniformity but also alleviates pinhole loading in the laser amplification chain. The ultrafast-picket-smoothing scheme supplants only the first SSD

dimension. The efficient and asymptotic smoothing of the ultrafast pickets depends on a second and orthogonal SSD smoothing dimension in the same way that 2-D SSD does.

The ultrafast-picket-pulse train is defined to have an intensity FWHM pulse width of  $\Delta t_{\text{FWHM}}$ , a pulse repetition period of  $\Delta T$ , and an inverse duty cycle given by  $\text{IDC} \equiv \Delta T/\Delta t$ , where  $\Delta t$  is the pulse width that contains 99% of the pulses's energy. The pulse train that will be discussed is a fourth-order super-Gaussian and can be written as

$$\text{picket}(t) \equiv \sum_{n=0}^N \exp \left[ -\ln(2) \left( \frac{t-t_0-n\Delta T}{\Delta t_{\text{FWHM}}} \right)^4 \right], \quad (11)$$

s.t.  $N\Delta T \leq 3$  ns. The pulse width as defined in Eq. (11) is  $\Delta t = 28.1$  ps. The fundamental beam shape for the pickets is defined to be the same as the base-line 2-D SSD [i.e., Eq. (5)].

A pulsed laser beam followed by a phase modulator that is then dispersed by a grating describes any ultrafast-picket scheme schematically (see Fig. 86.41). This schematic graphically describes the mathematical functions of the resultant pulsed beam used in the *Waasikwa'* simulations. The phase modulator in Fig. 86.41 represents an optional phase chirp that can be applied to the pickets. If the phase chirp is locked to the pulse repetition rate of the pickets, the phase chirp of each picket, whose function is given by  $\phi_{\text{chirp}}(t)$ , is then appended to Eq. (11) in the form of  $\exp[i\phi_{\text{chirp}}(t-t_0-n\Delta T)]$ .

The grating G2, in Fig. 86.41, disperses the ultrafast pickets with a grating dispersion,  $\xi_y$ , which temporally shears the beam by an amount  $\tau_{D1}$ . Consequently, the beam becomes sub-apertured and then sweeps across the whole near-field aperture as time progresses (see Fig. 86.42). The sub-apertured width

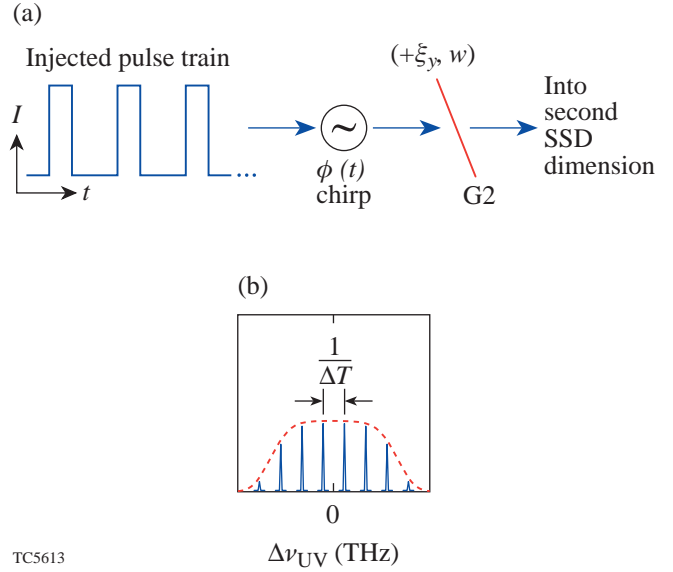


Figure 86.41 (a) Schematic describing a chirped UV pulsed beam in the *Waasikwa'* simulations. A pulse-modulated laser is chirped by the phase modulator M<sub>1</sub> with the phase given by  $\phi_{\text{chirp}}(t)$  and then dispersed by the grating G2. This schematic does not describe the layout of an actual implementation; it is simply a graphical representation of the mathematical function of the resultant pulsed beam. (b) A plot representing the envelope of the temporal spectrum from a generic chirped-pulse train, which is identical to the temporal spectrum from a single chirped pulse. The series of delta functions represents the temporal-spectral modes from the chirped-pulse train that are spaced by  $1/\Delta T$ . The envelope modulates these modes.

$W_a$  is equivalent to the ratio of the pulse width  $\Delta t$  to the grating dispersion  $\xi_y$ , which can then be related to other quantities,

$$W_a = \frac{\Delta t}{\xi_y} = \frac{\Delta T}{\xi_y \text{IDC}} = \frac{D_{\text{NIF}}}{\text{IDC} \cdot N'_{\text{cc}}}, \quad (12)$$

Table 86.III: Summary of the relevant parameters for the NIF 2-D SSD base-line models.

Sim Name	2-D SSD Base-Line Models													
	First Applied SSD Dimension						Second Applied SSD Dimension						Combined BW	
	$\delta_{M1}$	$\nu_{M1}$ (GHz)	$\Delta\lambda_{M1}$ (Å) IR	$\Delta\nu_{M1}$ (GHz) UV	$\Delta\nu_{\text{eff}}$ (GHz) UV	$N_{\text{cc}1}$	$\delta_{M2}$	$\nu_{M2}$ (GHz)	$\Delta\lambda_{M2}$ (Å) IR	$\Delta\nu_{M2}$ (GHz) UV	$\Delta\nu_{\text{eff}2}$ (GHz) UV	$N_{\text{cc}2}$	$\Delta\nu_{\text{rss}}$ (GHz)	$\Delta\nu_{\text{eff}}$ (GHz)
BL1	16.67	8.76	10.8	876	665	1	8.37	3.23	2.0	162	167	1	891	979
BL1b	16.67	8.76	10.8	876	665	1							891	979
BL2	8.333	17.52	10.8	876	656	2							891	979

where  $N'_{cc}$  is analogous to the number of color cycles in an SSD system and is defined as

$$N'_{cc} \equiv \frac{\tau_D}{\Delta T}. \tag{13}$$

When the quantity  $N'_{cc} > 1$ , multiple pickets will simultaneously illuminate the near field and will result in improved low-spatial-frequency smoothing and resonant features in the far-field power spectrum similar to an SSD system of multiple color cycles. The target will experience an intensity ripple when  $N'_{cc}$  is not an integer. Under these conditions, however, the IDC decreases, which degrades the benefit of improved frequency conversion and decreased power imbalance. When the quantity  $N'_{cc} < 1$ , the IDC increases (for a given grating dispersion) and will increase frequency conversion and reduce power imbalance. The target will experience an intensity ripple, however, due to the absence of any pickets over the duration of  $\Delta T - \tau_D$  (unless the pickets can be timed to alter-

nately illuminate different beams in each quad to compensate). More importantly, the smoothing will become inefficient because the far-field modes will become statistically dependent, just as in the SSD case. When the quantity  $N'_{cc} = 1$ , the target will experience little ripple (in fact, if the pulse is rectangular, the target will experience no intensity ripple) and the smoothing will be efficient over all spatial wavelengths.

As originally conceived, the chirp would be applied by allowing the pickets to enter a phase-locked phase modulator such as the current fiber modulator. In this scenario the pulse period is phase-locked to the phase modulator such that the maximum instantaneous wavelength shift is applied to each picket (see Fig. 86.43). The pickets effectively “sample” the central portion of the bandwidth produced by the phase modulator. Notice in Fig. 86.43 how the “sampled” spectrum of the ultrafast pickets is nearly uniform and centrally distributed, unlike the distinctive Bessel mode pattern produced by the frequency-modulated (FM) spectrum of SSD.

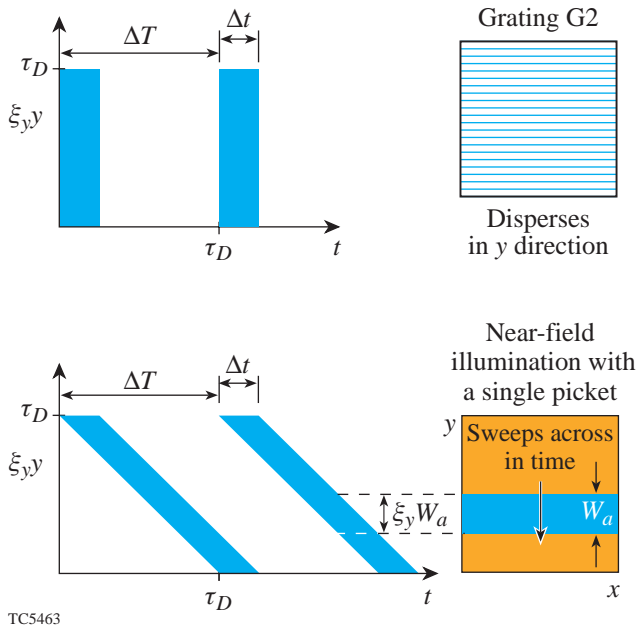


Figure 86.42 The two plots on the left-hand side represent beam cross sections before and after the grating G2, which temporally skews the beam. Consequently, the beam becomes sub-apertured and then sweeps across the whole near-field aperture as time progresses (see the plot on the lower right-hand side). If the pulse period  $\Delta t$  is chosen to equal the temporal shear  $\tau_D$  from grating G2, the target will be continuously illuminated since as one picket exits the aperture, the next one will enter on the opposite side.

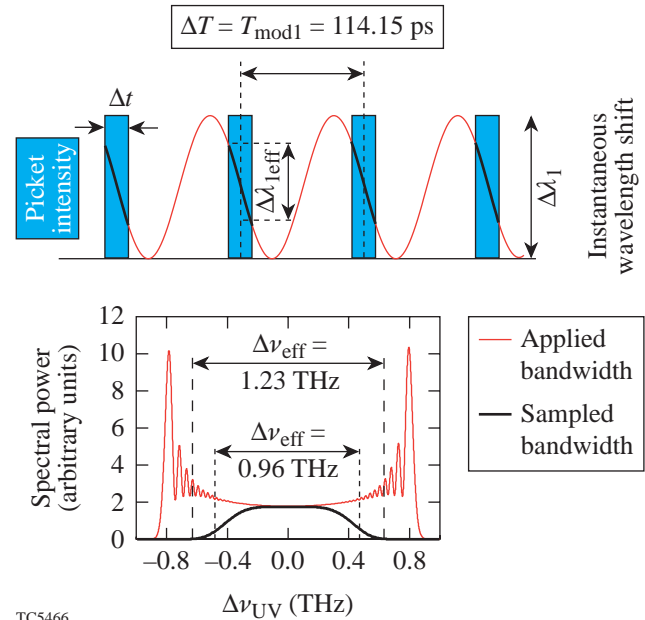


Figure 86.43 A chirp is applied to each picket using a phase-locked modulator. This diagram graphically illustrates how the modulator applies the maximum instantaneous wavelength shift to each picket. The pickets effectively “sample” the central portion of the bandwidth applied by the modulator.

1. Temporal Spectrum and Diffraction-Limited Far-Field Pattern of Ultrafast Pickets

The centrally distributed sampled spectrum directly translates into reduced pinhole loading. The applied temporal spectrum maps into the pattern of a diffraction-limited far field since the dispersed beam maps the applied temporal bandwidth into spatial bandwidth (see Ref. 16 for a detailed description). The time-integrated, diffraction-limited far-field patterns of the NIF 2-D SSD base-line and ultrafast pickets are illustrated in Fig. 86.44. The pattern from the NIF 2-D SSD base line

[Fig. 86.44(a)] shows high fluence levels near the four outer corners of the pattern. In contrast, the pattern from the ultrafast-picket design [Fig. 86.44(b)] shows a much lower and uniform fluence level more evenly distributed about the center. Both images show the distinct Bessel mode pattern in the direction corresponding to the second SSD dimension.

The temporal spectral modes of the ultrafast picket fence are separated by the inverse of the pulse repetition period, e.g.,  $1/\Delta T$ , and they conform to the envelope of the spectrum of a single pulse [see Fig. 86.41(b)]. These spectral modes become modes in the far field and lead to the number of independent speckle patterns in the asymptotic limit. The mode spacing in the far field in the direction corresponding to the grating G2 is calculated by  $N'_{cc} f_{NIF} \lambda_{UV} / D_{NIF}$ . The number of modes due to the ultrafast pickets can be calculated using

$$\text{Modes}' = \Delta v'_{UV} \cdot \Delta T = \frac{\Delta \theta'_{M1}}{\xi_y \lambda_{UV}} \Delta T = \frac{\Delta \theta'_{M1} D_{NIF}}{\lambda_{UV} N'_{cc}}. \quad (14)$$

The number of modes due to the SSD for either dimension can be calculated using

$$\text{Modes} = \frac{\Delta v_{UV}}{v_M} = \frac{\Delta \theta_M D_{NIF}}{\lambda_{UV} N_{cc}}, \quad (15)$$

where the laser divergence  $\Delta \theta_M$  and number of color cycles  $N_{cc}$  corresponding to either SSD dimension is substituted into Eq. (15). The total number of modes in the far field is computed as the product of the number of modes from the first smoothing dimension (either SSD or ultrafast picket fence) and the number due to the second orthogonal SSD dimension. If the temporal spectrum of either the ultrafast pickets or SSD is nonuniform, the effective number of modes is reduced, similar to SSD.<sup>18</sup> The reduction ratio is approximated as the ratio of the effective bandwidth calculated using Eq. (9) to the overall bandwidth of each smoothing direction separately. The ultrafast-picket-fence schemes proposed in this article have a very uniform distribution, which can decrease the asymptotic level reached by approximately 20% as compared to base-line 2-D SSD.

The temporal spectrum of the ultrafast pickets can be modified or tailored to reduce the pinhole loading due to the tails of the spectrum seen in Fig. 86.43. Through an iterative Fourier technique, similar to phase-retrieval techniques, a chirped pulse can be designed to produce the high-order super-Gaussian temporal spectrum as illustrated in Fig. 86.45.

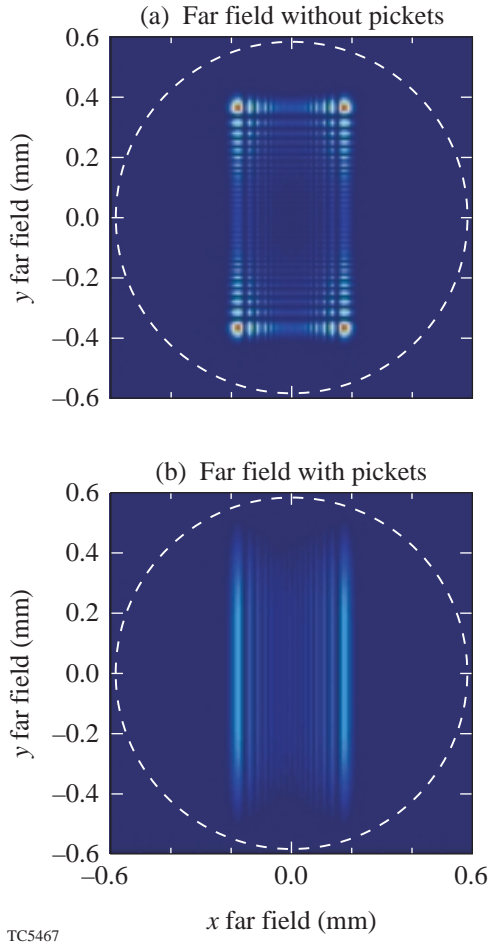
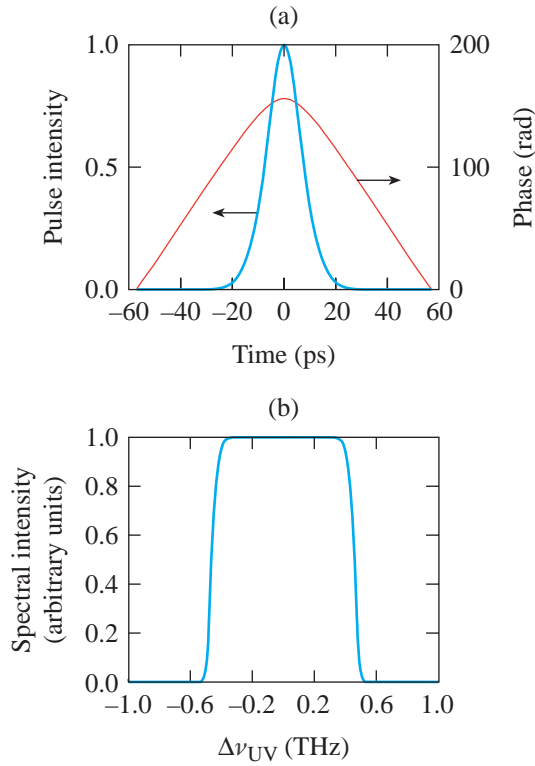


Figure 86.44 The time-integrated diffraction-limited far-field patterns for the NIF 2-D SSD (a) base-line and (b) ultrafast pickets. The images are plotted using the same gray scale to indicate relative fluence levels. The pattern from the NIF 2-D SSD base line shows high fluence levels near the four outer corners of the pattern. In contrast, the pattern from the ultrafast-picket design shows a much lower, uniform fluence level more evenly distributed about the center. Both images show the distinct Bessel pattern in the direction corresponding to the second SSD dimension.



TC5594

Figure 86.45

A chirped pulse (a) and its temporal spectrum (b). The spectrum was the design point of an iterative Fourier technique to find the required shape and phase of the pulse in (a). This spectrum can further reduce the pinhole loading by removing the energy located in the tails of the spectrum seen in Fig. 86.43.

## 2. Alternate Methods of Producing Chirped Ultrafast Pickets

Alternate methods are available for producing chirped ultrafast pickets that need not be phase locked. One method is to reflect a stretched and longer chirped pulse from a fiber-Bragg grating; this results in a train of chirped pulses of desired shape and chirp by properly engineering the fiber. This technique meshes well with the tailored chirped pulse seen in Fig. 86.45 since the pulse shape is approximately a  $\text{sec } h^2$  and the chirp is nearly linear, both of which are easily obtained using current laser and fiber technologies.

### Far-Field Simulation and Analysis

*Waasikwa*' calculates the planar far-field fluence using

$$F(x_{\text{ff}}, y_{\text{ff}}) \equiv \int_{\text{pulse duration}} I_{\text{ff}}(x_{\text{ff}}, y_{\text{ff}}, t) dt, \quad (16)$$

where  $I_{\text{ff}}(x_{\text{ff}}, y_{\text{ff}}, t)$  represents the instantaneous far-field intensity. The evolution of the far-field intensity is calculated by taking the modulus squared of a 2-D spatial Fourier transform of the UV near field [comp. Ref. 19, pp. 83–89]:

$$I_{\text{ff}}(x_{\text{ff}}, y_{\text{ff}}, t) \equiv \left| \iint_{\forall \text{space}} E(x, y, t) \exp \left[ -i \frac{2\pi}{\lambda_{\text{UV}} f_{\text{NIF}}} (x_{\text{ff}} x + y_{\text{ff}} y) \right] dx dy \right|^2, \quad (17)$$

where  $E(x, y, t)$  represents the complex-valued UV electric field strength in the near field and  $(x, y)$  and  $(x_{\text{ff}}, y_{\text{ff}})$  are the near- and far-field coordinate systems, respectively;  $\lambda_{\text{UV}} = 351 \text{ nm}$  is the UV vacuum wavelength; and  $f_{\text{NIF}} = 770 \text{ cm}$  is the assumed NIF focal length. The integrations are calculated as a running summation at every simulation time step  $dt$ . For these  $\sim 1\text{-THz}$ -bandwidth pulsed beams, the time step is defined to be  $dt = 0.75 \text{ ps}$ , which sufficiently over-samples the bandwidth based on the Nyquist criterion.

The 2-D power spectral density (2-D power spectrum or simply the 2-D PSD) is derived from the simulated far-field fluence by taking the modulus squared of the 2-D spatial Fourier transform:

$$\text{PSD}(k_{x_{\text{ff}}}, k_{y_{\text{ff}}}) \equiv \left| \iint_{\forall \text{far field}} F(x_{\text{ff}}, y_{\text{ff}}) \exp \left[ -i(k_{x_{\text{ff}}} x_{\text{ff}} + k_{y_{\text{ff}}} y_{\text{ff}}) \right] dx_{\text{ff}} dy_{\text{ff}} \right|^2, \quad (18)$$

where  $F(x_{\text{ff}}, y_{\text{ff}})$  represents the far-field fluence as defined by Eq. (16),  $(x_{\text{ff}}, y_{\text{ff}})$  is the far-field coordinate system, and  $(k_{x_{\text{ff}}}, k_{y_{\text{ff}}})$  is the far-field's spatial-frequency coordinate system. The azimuthal sum at each radial wave number of the 2-D power spectrum defines the 1-D power spectral density (1-D power spectrum or simply the 1-D PSD) and is given by

$$\text{psd}(k_{\text{ff}}) \equiv \oint \text{PSD}(k_{x_{\text{ff}}}, k_{y_{\text{ff}}}) k_{\text{ff}} d\theta, \quad (19)$$

where the transformation into polar coordinates is defined as  $k_{\text{ff}} \equiv \sqrt{k_{x_{\text{ff}}}^2 + k_{y_{\text{ff}}}^2}$  and  $\tan \theta \equiv k_{y_{\text{ff}}} / k_{x_{\text{ff}}}$ . The single-beam

irradiation nonuniformity  $\sigma_{\text{rms}}$  is defined as the square root of the ratio of the speckle power (e.g., the high frequencies  $k_{\text{ff}} \geq 5.88$  rad/mm at the NIF target plane or  $\ell$ -modes  $\ell \geq 10$ ) to the envelope power of the far-field spot (i.e., the low frequencies  $k_{\text{ff}} < 5.88$  rad/mm). The wave number 5.88 rad/mm divides the envelope and speckle frequencies. A finite entrance pupil imposes a limitation on the spatial-frequency bandwidth of an optical system (compare the intensity-impulse response or point-spread function of a diffraction-limited system with a rectangular exit-pupil function in Ref. 19, pp. 110–113). On the NIF, the highest spatial frequency of the far field, regardless of the near-field beam profile, is limited by the finite square shape of the full aperture beam whose width is defined as  $D_{\text{NIF}} = 35.1$  cm. Consequently, the 2-D PSD possesses a square-shaped absolute cutoff whose width along both the  $k_{x\text{ff}}$  and  $k_{y\text{ff}}$  axes corresponds to the  $f$ -number limited spatial frequency

$$k_{\text{cutff}} = \frac{2\pi D_{\text{NIF}}}{\lambda_{\text{UV}} f_{\text{NIF}}} = 0.816 \frac{\text{rad}}{\mu\text{m}}. \quad (20)$$

Due to the square-shaped cutoff of the 2-D PSD, the 1-D PSD has an absolute cutoff of

$$k'_{\text{cutff}} = \sqrt{2} \cdot k_{\text{cutff}}. \quad (21)$$

For the ultrafast picket fence schemes, the high aspect ratio (which is proportional to IDC) of the sub-apertured near field corresponds to an absolute cutoff  $k'_{\text{cutff}} \cong k_{\text{cutff}}$ .

**Smoothing Performance Results**

*Waasikwa*' far-field simulations calculated the single-beam nonuniformity as a function of time for a duration of 3 ns. Three NIF 2-D SSD base-line designs and four ultrafast picket designs were calculated using the parameters listed in Tables 86.III and 86.IV. The names listed under the ‘‘Sim Name’’ column in these tables will be used to designate each model.

The smoothing performances for Picket1, Picket2, and the BL1 designs are plotted in Fig. 86.46 for a 3-ns duration for all

Table 86.IV: Summary of the relevant parameters for the NIF ultrafast-picket-smoothing schemes. The second SSD dimension has the same parameters as in Table 86.III.

Sim Name	Pulse Type	First Smoothing Dimension										Combined BW
		Applied SSD				Ultrafast Pickets						
		$\delta_{\text{M1}}$	$\nu_{\text{M1}}$ (GHz)	$\delta\lambda_{\text{M1}}$ (Å) IR	$N_{\text{cc1}}$	IDC	$N'_{\text{cc}}$	$\Delta T$ (ps)	$\Delta t_{\text{FWHM}}$ (ps)	$\Delta t$ (ps)	$\Delta\nu_{\text{eff}}$ (GHz) UV	
Picket1	Single SG4	31.02	8.76	20.1	1	4	1	114.15	19.0	28.1	970	994
Picket1b	Single SG4	31.02	8.76	20.1	1	4	1	114.15	19.0	28.1	970	994
Picket2	Double SG4	31.02	8.76	20.1	1	2	2	57.075	19.0	28.1	970	995
Chirped1	Single $\text{sech}^2$	n/a	n/a	n/a	n/a	2.5	1	114.15	19.0	45	947	993

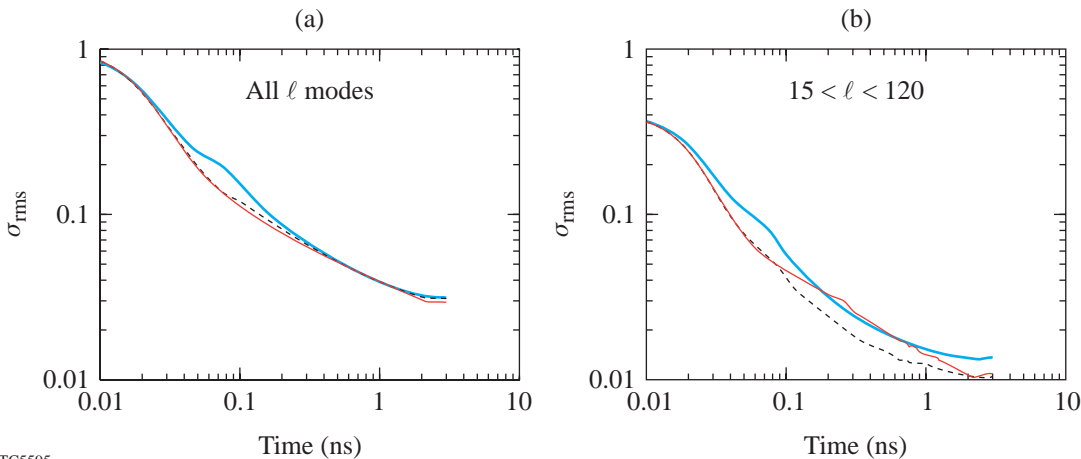


Figure 86.46 The nonuniformity plotted against time for (a) all  $\ell$  modes and (b) the  $\ell$ -mode range  $15 < \ell < 120$ . The red line is the NIF ultrafast Picket1, the dashed line is the NIF ultrafast Picket2, and the blue line is the NIF 2-D SSD base-line BL1.

TC5595

the  $\ell$  modes and over the  $\ell$ -mode range of  $15 < \ell < 120$ . The smoothing performance of both picket designs is initially better than and later is nearly equivalent to BL1 design. The Picket2 design produces better smoothing than the other two designs for the range  $15 < \ell < 120$  because two pickets are simultaneously illuminated, which is analogous to a two-color-cycle 2-D SSD system. The smoothing performances for the tailored chirped pulse (designated as Chirped1), Picket1, and BL1 are plotted in Fig. 86.47 for a 3-ns duration for all the  $\ell$ -modes and over the  $\ell$ -mode range,  $15 < \ell < 120$ .

The smoothing performances for the BL1, Picket1, and Picket2 simulations are identical for the first 15 ps because they have the same pulse rise time and a similarly shaped sub-apertured near field (BL1 is sub-apertured during the time corresponding to the initial temporal shear and the shape matches the picket's shape for the first 15 ps). The smoothing performance for Chirped1 is initially not as good as Picket1 or Picket2 because it has a much longer rise time of approximately 25 ps. The smoothing performance for both picket types, however, is better than BL1 over the duration  $20 \text{ ps} < t < 200 \text{ ps}$ . This is due to the fact that the ultrafast picket designs are designed to smooth efficiently, i.e., full-smoothing, full-bandwidth for a sub-apertured near field; whereas the base-line designs do not achieve full-smoothing/full-bandwidth until the aperture is filled, i.e., after the initial temporal shear  $\tau_{D1} = 114.15 \text{ ps}$ . Therefore, the picketed designs effectively have  $\sim 115 \text{ ps}$  of smoothing accomplished before the base-line designs achieve efficient smoothing. Over the  $\ell$ -band

range  $20 \leq \ell < 120$ , Picket2 has better smoothing performance than Picket1 for  $t > 80 \text{ ps}$  because by this time the second picket has appeared in Picket2 and remains for the rest of the simulation. The second picket reduces the nonuniformity in this  $\ell$ -band range due to the aforementioned multiple-color-cycle effects. The overall smoothing performance for all the simulations are nearly equivalent, for the duration  $t > 200 \text{ ps}$  and until the asymptotic levels are reached (approximately  $t \sim 3 \text{ ns}$ ). The Picket #1 simulation has reduced asymptotic overall nonuniformity because of the uniform bandwidth distribution. The simulation Picket1 has a lower asymptotic nonuniformity relative to Picket2 because of  $N'_{cc} = 2$ . The asymptotic levels for both picket-type simulations, however, are nearly equivalent for the  $\ell$ -band range  $15 \leq \ell \leq 120$ .

The instantaneous 1-D PSD, defined by Eq. (19), for the ultrafast-picket-fence schemes is approximately  $4\times$  higher over the  $\ell$ -band range  $15 \leq \ell \leq 120$  as compared to BL1 (see Fig. 86.48). The ultrafast-picket-fence schemes produce a sub-apertured near field, which corresponds to a 2-D PSD whose extent (i.e., its cutoff wave number  $k_{\text{cutff}}$ ) is reduced in the corresponding direction by a factor of  $\sim \text{IDC}$  (for  $N'_{cc} = 1$ ). By conservation of energy, the sub-apertured near field increases the spectral power in the picketed direction by a factor of  $\sim \text{IDC}$ . Consequently, the azimuthal sum (i.e., the 1-D PSD) reflects this additional power. Note also that there is still power up to  $k_{\text{cutff}} = 0.816 \text{ rad}/\mu\text{m}$  because the second SSD dimension is still full aperture.

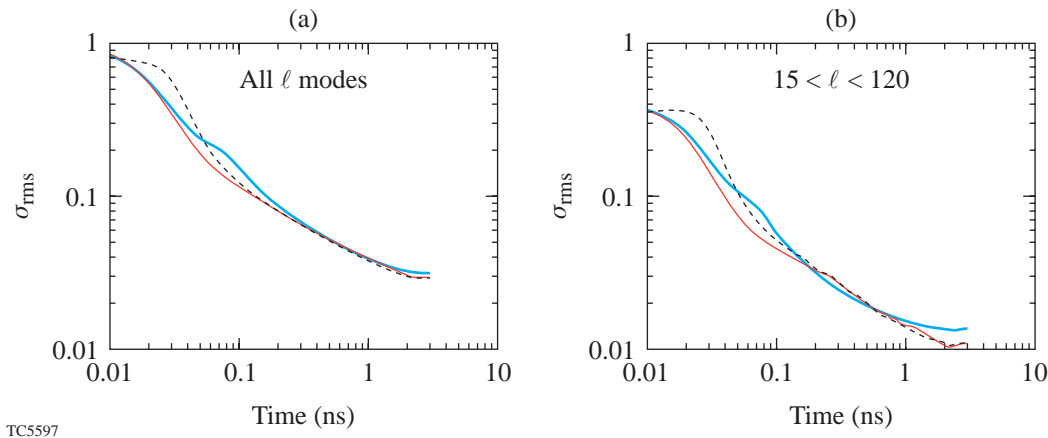


Figure 86.47

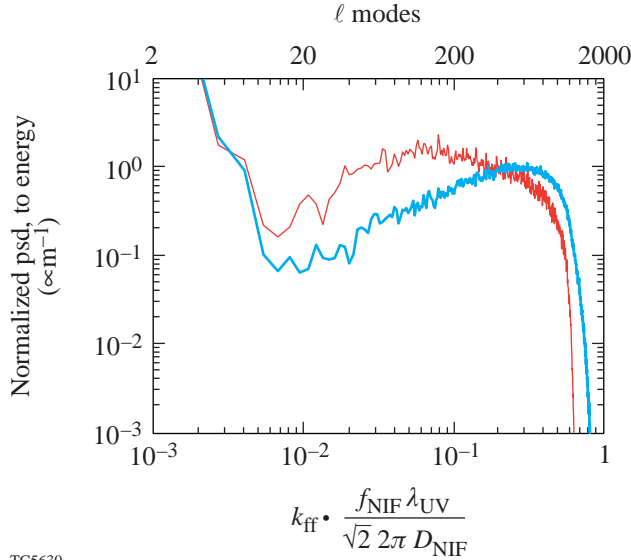
The nonuniformity plotted against time for (a) all  $\ell$  modes and (b) the  $\ell$ -mode range  $15 < \ell < 120$ . The red line is the NIF ultrafast Picket1, the dashed line is the NIF ultrafast chirped-picket Chirped1, and the blue line is the NIF 2-D SSD base-line BL1.

To relate the smoothing performance to effective bandwidth or inverse coherence time, the initial rise-time behavior must be eliminated because the simple model of the nonuniformity as a function of time and wave number does not account for this rise-time behavior<sup>7</sup>

$$\sigma^2(t, k_{\text{ff}}) = \sigma_0^2(k_{\text{ff}}) \frac{t_c}{t + t_c} + \sigma_{\text{asym}}^2(k_{\text{ff}}), \quad (22)$$

where  $\sigma_0^2(k_{\text{ff}}) = \sigma^2(0, k_{\text{ff}})$  is the initial value of the nonuniformity and  $\sigma_{\text{asym}}^2(k_{\text{ff}}) = \sigma^2(\infty, k_{\text{ff}})$  is the asymptotic level of the nonuniformity for the radial wave number  $k_{\text{ff}}$ . Advancing the pulse by this delay and delaying the time-integrated far field by the same time accomplish this task. Therefore, two additional simulations were run with a delay of an amount corresponding to the rise-time delay for each model. The base-line model BL1b is identical to BL1 except for the included delay of 130 ps. The ultrafast-picket-fence model Picket1b is identical to Picket1 except for the included delay of 30 ps.

The nonuniformity of Picket1b is nearly equivalent to BL1b over the  $\ell$ -band range  $15 \leq \ell \leq 120$  even though the instanta-



TC5630

Figure 86.48

The instantaneous far-field 1-D power spectra for models BL1 (blue line) and Picket1 (red line). The subapertured near field of the ultrafast picket scheme increases the power in modes  $\ell < 400$  relative to the base-line 2-D SSD model. The increase is approximately equal to the IDC value for the ultrafast picket scheme over the majority of the affected  $\ell$  modes.

neous power is  $4\times$  higher in these modes (see Fig. 86.48). The reason for this behavior is simple: the effective bandwidth or inverse coherence time is approximated  $4\times$  higher for Picket1b relative to BL1b. The sub-apertured near field of the Picket1b causes the bandwidth to be distributed over a reduced wave-number range and consequently smoothes these wavelengths faster. This effect is calculated two independent ways: (1) smoothing performance of a full simulation is fit to the model of Eq. (22) and (2) a phenomenological model is developed.

Calculating the effective bandwidth distribution for either the 2-D SSD system or the ultrafast-picket-fence scheme is essentially a 2-D problem. Two- and one-dimensional phenomenological models of the effective bandwidth are given here. In the first smoothing direction, the bandwidth is distributed as<sup>10</sup>

$$\Delta v_x(k_{x_{\text{ff}}}) = 2\Delta v_{M1} \sin\left(k_{x_{\text{ff}}} \frac{\kappa_1}{2} N_{\text{cc1}}\right), \quad (23)$$

where  $\Delta v_{M1}$  is the FM modulator bandwidth in the UV for the first SSD modulator or the chirped-pulse bandwidth and the parameter  $\kappa_1$  is the one-half speckle width, ( $\kappa_1 = \kappa_{\text{SSD1}} = f_{\text{NIF}}/\lambda_{\text{UV}}/D_{\text{NIF}}$  for the first SSD dimension or  $\kappa_1 = \kappa_{\text{picket}} = \text{IDC} \cdot f_{\text{NIF}}/\lambda_{\text{UV}}/D_{\text{NIF}}$  for the ultrafast picket fence). In the second smoothing direction, the bandwidth is distributed as

$$\Delta v_y(k_{y_{\text{ff}}}) = 2\Delta v_{M2} \sin\left(k_{y_{\text{ff}}} \frac{\kappa_2}{2} N_{\text{cc2}}\right), \quad (24)$$

where  $\Delta v_{M2}$  is the FM modulator bandwidth in the UV for the second SSD modulator and  $\kappa_2 = \kappa_{\text{SSD1}}$  is the one-half speckle width for the second SSD dimension. For the 2-D problem, it is assumed that the orthogonal components of the wave vector  $\mathbf{k}_{\text{ff}} \equiv k_{x_{\text{ff}}}\hat{x} + k_{y_{\text{ff}}}\hat{y}$  are affected independently so that the effective bandwidth is given by the quadrature sum

$$\Delta v'_{\text{eff}}(k_{x_{\text{ff}}}, k_{y_{\text{ff}}}) = \sqrt{|\Delta v_x(k_{x_{\text{ff}}})|^2 + |\Delta v_y(k_{y_{\text{ff}}})|^2}. \quad (25)$$

The smoothing of the 1-D PSD then corresponds to the weighted azimuthal average of the two-dimensional effective bandwidth function Eq. (25).

$$\Delta v_{\text{eff}}(k_{\text{ff}}) = \frac{\oint \Delta v'_{\text{eff}}(k_{x_{\text{ff}}}, k_{y_{\text{ff}}}) \text{PSD}_0(k_{x_{\text{ff}}}, k_{y_{\text{ff}}}) k_{\text{ff}} d\theta}{\oint \text{PSD}_0(k_{x_{\text{ff}}}, k_{y_{\text{ff}}}) k_{\text{ff}} d\theta}, \quad (26)$$

where the weighting function  $\text{PSD}_0(k_{x\text{ff}}, k_{y\text{ff}})$  is the 2-D PSD of the aberration-free ideal near field of Eq. (4) at one instant of time for either the 2-D SSD base-line full-aperture designs or the sub-apertured ultrafast picket-fence designs.

The nonuniformity  $\sigma^2(t, k_{\text{ff}})$  calculated from the simulations BL1b and Pickets1b is fit to the nonuniformity model of Eq. (22) using the coherence time as the one degree of freedom in order to estimate the effective bandwidth by  $\Delta\tilde{v}_{\text{eff}}(k_{\text{ff}}) = 1/t_c$ . The simulation data  $\sigma^2(t, k_{\text{ff}})$  is averaged over  $\pm 5$  neighboring wave numbers before being fit to the model of Eq. (22). The estimated effective bandwidth by  $\Delta\tilde{v}_{\text{eff}}(k_{\text{ff}})$  is compared to that calculated with the phenomenological effective bandwidth model given by Eq. (26) [see Fig. 86.49(a)]. The ratio of the effective bandwidths from the phenomenological model is plotted in Fig. 86.49(b). The fact that the effective bandwidth for the Picket1b is approximately 4x higher than the BL1b over the  $\ell$ -band range  $15 \leq \ell \leq 120$  explains why they have a similar smoothing performance over the l-band range in Fig. 86.46(b).

**Conclusion**

The underlying motivation of implementing the ultrafast pickets on the NIF is the ability to increase the frequency-conversion efficiency and to reduce the contribution to the beam-to-beam power imbalance in the foot portion of an ICF laser pulse.<sup>5</sup> In this article, the smoothing performance of the ultrafast pickets was analyzed and shown to be equivalent to the NIF 2-D SSD base-line designs for direct-drive ICF as long as the applied bandwidths and divergences are close to the base-line designs. If no bandwidth is applied in the first dimension or if the IDC is too large, the early-time smoothing performance is not as effective. It was also discovered that the diffraction-limited far-field pattern produced by the chirped pickets can reduce pinhole loading, which might lead to an increase in the permitted laser divergence. Overall, a properly designed ultrafast picket system offers many system-wide benefits at the cost of a more complicated front end.

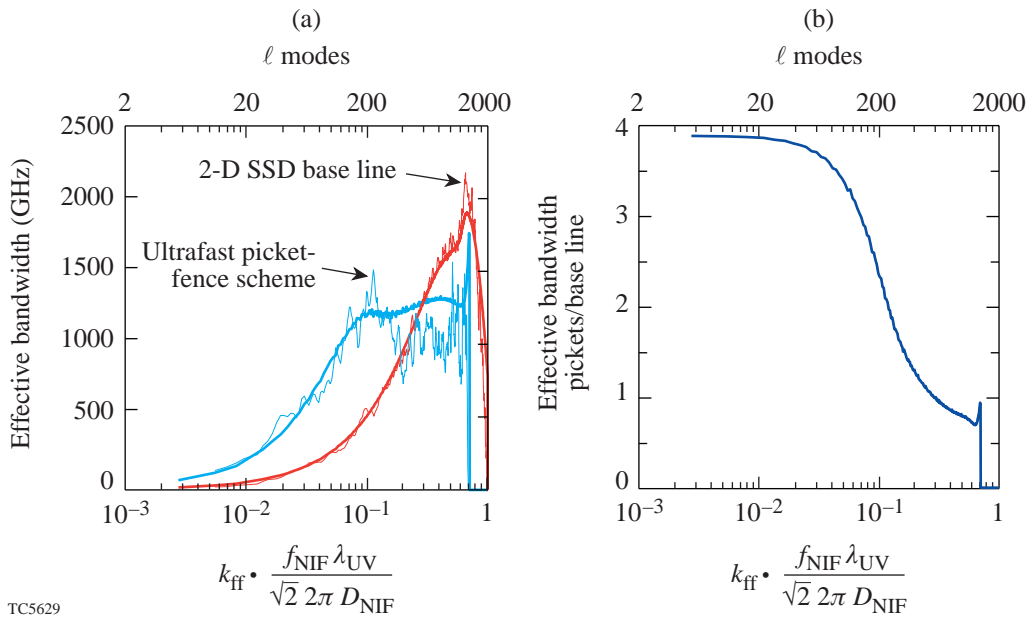


Figure 86.49

(a) The one-dimensional phenomenological model of the effective bandwidth  $\Delta v_{\text{eff}}(k_{\text{ff}})$  and the estimated effective  $\Delta\tilde{v}_{\text{eff}}(k_{\text{ff}})$  bandwidth are compared for both the BL1b and Picket1b *Waasikwa*' simulations. The bold traces represent the phenomenological model  $\Delta v_{\text{eff}}(k_{\text{ff}})$ , and the thin traces represent the simulation's effective bandwidth  $\Delta\tilde{v}_{\text{eff}}(k_{\text{ff}})$ . (b) The ratio of phenomenological models  $\Delta v_{\text{eff}}(k_{\text{ff}})$  for Picket1b to BL1b is plotted, which shows the increased bandwidth in the lower  $\ell$ -band range.

## ACKNOWLEDGMENT

This work was partially supported by the U.S. Department of Energy Office of Inertial Confinement Fusion under Cooperative Agreement No. DE-FC03-92SF19460, the University of Rochester, and the New York State Energy Research and Development Authority. The support of DOE does not constitute an endorsement by DOE of the views expressed in this article.

## REFERENCES

1. C. P. Verdon, *Bull. Am. Phys. Soc.* **38**, 2010 (1993).
2. S. E. Bodner, D. G. Colombant, J. H. Gardner, R. H. Lehmburg, S. P. Obenschain, L. Phillips, A. J. Schmitt, J. D. Sethian, R. L. McCrory, W. Seka, C. P. Verdon, J. P. Knauer, B. B. Afeyan, and H. T. Powell, *Phys. Plasmas* **5**, 1901 (1998).
3. D. K. Bradley, J. A. Delettrez, and C. P. Verdon, *Phys. Rev. Lett.* **68**, 2774 (1992); J. Delettrez, D. K. Bradley, and C. P. Verdon, *Phys. Plasmas* **1**, 2342 (1994); J. D. Kilkenny, S. G. Glendinning, S. W. Haan, B. A. Hammel, J. D. Lindl, D. Munro, B. A. Remington, S. V. Weber, J. P. Knauer, and C. P. Verdon, *Phys. Plasmas* **1**, 1379 (1994); R. Epstein, *J. Appl. Phys.* **82**, 2123 (1997); V. A. Smalyuk, T. R. Boehly, D. K. Bradley, V. N. Goncharov, J. A. Delettrez, J. P. Knauer, D. D. Meyerhofer, D. Oron, and D. Shvarts, *Phys. Rev. Lett.* **81**, 5342 (1998).
4. F. J. Marshall and G. R. Bennett, *Rev. Sci. Instrum.* **70**, 617 (1999); F. J. Marshall, J. A. Delettrez, V. Yu. Glebov, R. P. J. Town, B. Yaakobi, R. L. Kremens, and M. Cable, *Phys. Plasmas* **7**, 1006 (2000).
5. J. E. Rothenberg, *Appl. Opt.* **39**, 6931 (2000).
6. T. R. Boehly, D. L. Brown, R. S. Craxton, R. L. Keck, J. P. Knauer, J. H. Kelly, T. J. Kessler, S. A. Kumpan, S. J. Loucks, S. A. Letzring, F. J. Marshall, R. L. McCrory, S. F. B. Morse, W. Seka, J. M. Soures, and C. P. Verdon, *Opt. Commun.* **133**, 495 (1997).
7. S. P. Regan, J. A. Marozas, J. H. Kelly, T. R. Boehly, W. R. Donaldson, P. A. Jaanimagi, R. L. Keck, T. J. Kessler, D. D. Meyerhofer, W. Seka, S. Skupsky, and V. A. Smalyuk, *J. Opt. Soc. Am. B* **17**, 1483 (2000).
8. S. Skupsky, R. W. Short, T. Kessler, R. S. Craxton, S. Letzring, and J. M. Soures, *J. Appl. Phys.* **66**, 3456 (1989).
9. Laboratory for Laser Energetics LLE Review **69**, 1, NTIS document No. DOE/SF/19460-152 (1996) (copies may be obtained from the National Technical Information Service, Springfield, VA 22161); S. Skupsky and R. S. Craxton, *Phys. Plasmas* **6**, 2157 (1999).
10. J. E. Rothenberg, *J. Opt. Soc. Am. B* **14**, 1664 (1997).
11. T. J. Kessler, Y. Lin, J. J. Armstrong, and B. Velazquez, in *Laser Coherence Control: Technology and Applications*, edited by H. T. Powell and T. J. Kessler (SPIE, Bellingham, WA, 1993), Vol. 1870, pp. 95–104.
12. Y. Lin, T. J. Kessler, and G. N. Lawrence, *Opt. Lett.* **21**, 1703 (1996).
13. Y. Kato, unpublished notes from work at LLE, 1984; K. Tsubakimoto *et al.*, *Opt. Commun.* **91**, 9 (1992); K. Tsubakimoto *et al.*, *Opt. Commun.* **103**, 185 (1993).
14. Laboratory for Laser Energetics LLE Review **45**, 1, NTIS document No. DOE/DP40200-149 (1990) (copies may be obtained from the National Technical Information Service, Springfield, VA 22161); T. E. Gunderman, J.-C. Lee, T. J. Kessler, S. D. Jacobs, D. J. Smith, and S. Skupsky, in *Conference on Lasers and Electro-Optics*, Vol. 7, 1990 OSA Technical Digest Series (Optical Society of America, Washington, DC, 1990), p. 354.
15. J. A. Marozas, S. P. Regan, J. H. Kelly, D. D. Meyerhofer, W. Seka, and S. Skupsky, "Laser Beam Smoothing Caused by the Small-Spatial-Scale *B*-Integral," to be published in the *Journal of the Optical Society of America B*.
16. Laboratory for Laser Energetics LLE Review **78**, 62, NTIS document No. DOE/SF/19460-295 (1999). Copies may be obtained from the National Technical Information Service, Springfield, VA 22161.
17. R. N. Bracewell, *The Fourier Transform and Its Applications*, 2nd ed., rev., McGraw-Hill Series in Electrical Engineering. Circuits and Systems (McGraw-Hill, New York, 1986).
18. J. E. Rothenberg, in *Solid State Lasers for Application to Inertial Confinement Fusion*, edited by W. F. Krupke (SPIE, Bellingham, WA, 1995), Vol. 2633, pp. 634–644.
19. J. W. Goodman, *Introduction to Fourier Optics* (McGraw-Hill, New York, 1968).

---

# Tests of EXAFS on OMEGA: Feasibility for Shock-Heating Measurements

## Introduction

As part of its participation in the Stockpile Stewardship Program (SSP), LLE is studying the feasibility of using extended x-ray absorption fine structure (EXAFS)<sup>1</sup> to characterize the properties of solid materials shocked at moderately high pressures (up to a few megabars). In particular, there is an interest in examining material properties since they affect the growth of hydrodynamic instabilities. Thus, a shocked material that retains its strength (or shear) will be more resistant to such instabilities than a molten solid. EXAFS is sensitive to the short-range order in crystals (as opposed to diffraction, which depends on longer-range order). It can be seen in amorphous materials<sup>2,3</sup> as well as liquids,<sup>4-6</sup> but the reduction in short-range order due to melting is then evident in the EXAFS spectrum. EXAFS can measure the density and temperature of the shocked solid in addition to indicating melting. The main limitation in shock-heating studies is the reduction of the EXAFS modulation amplitude with increasing temperature. This problem is discussed in detail in this article. EXAFS can possibly indicate whether the shock compression of the solid is one- or three-dimensional: the distances to the nearest atomic neighbors (which is measured by EXAFS) are different in the two cases. Initial tests show very high contrast EXAFS modulations when a thick, undriven Ti foil is backlit by the x-ray radiation from an imploded CH shell. The high contrast achieved in these tests is due to three factors: (a) using an imploded target as a backlighter, (b) using a very thick Ti absorber, and (c) using a CID array for detection. In preparation for future shocked-Ti experiments, we scope out the range of shock strengths where significant EXAFS modulation can be expected. Briefly, although a higher temperature reduces the amplitude of EXAFS modulations, a higher density mitigates this reduction (by raising the Debye temperature). For varying shock strengths we determine the temperature and density of the Ti metal and then the expected EXAFS visibility. EXAFS has been previously seen in laser-produced plasma experiments,<sup>7</sup> and at LLE it has been studied<sup>8</sup> in imploded spherical targets (where the absorber was also Ti).

## Experiment

The tests reported here were performed with undriven, 12.5- $\mu\text{m}$ -thick Ti foils, positioned in front of an x-ray spectrometer. Such tests are useful for determining the ability of the diagnostic system to measure the high-quality EXAFS modulations required to analyze shock-heated materials. The last section of this article discusses the problem of EXAFS visibility in future shocked-Ti experiments. In the present experiment, the 60-beam OMEGA laser system with SSD-smoothed beams (1.5  $\times$  11- $\text{\AA}$  bandwidth) was used to implode CH shells. We show data from two almost identical shots (21238 and 21239), where a 1-ns square pulse of energy  $\sim$ 22.8 kJ was used to implode 20- $\mu\text{m}$ -thick CH shells of 937- $\mu\text{m}$  outer diameter, filled with a mixture of hydrogen at 2.4 atm and deuterium at 0.6 atm.

Figure 86.50 shows the spectrum from shot 21238 obtained when the radiation emitted by the imploding CH shell is transmitted through the 12.5- $\mu\text{m}$ -thick Ti foil and measured by a Ge(1,1,1) crystal and a CID array (see below). The EXAFS modulations above the Ti *K* edge are clearly seen. The high-contrast modulations are due to three factors employed in these tests:

- (a) Using the intense (and smooth) emission of an imploding CH target as a backlighter. The smoothness of the incident spectrum is important for measuring modulations in the absorption. In other applications, a high-*Z* planar target is typically used for backlighting because it generates a line spectrum. The compressed CH, on the other hand, produces a smooth continuum spectrum; the high radiation intensity ( $\sim 10^{17}$  keV/keV at 5 keV) is due to the high density, not the high *Z*. Additional advantages of the imploded backlighter are the short emission time,  $\sim$ 120 ps (which may yield useful results even without time resolution), and the small dimension, leading to higher spectral resolution.

(b) Using a thick Ti foil, which results in a very high attenuation,  $\sim \exp(-4)$ , rather than the customary attenuation of  $\sim \exp(-1)$ . This increases the relative modulations in the measured signal: if the latter is written as  $I \sim \exp(-\tau d)$ , where  $\tau$  is the opacity and  $d$  is the foil thickness, the relative modulation  $|\Delta I/I| \sim d\Delta\tau$  is proportional to the foil thickness. The optimal thickness is the largest for which the signal is still above the noise level. The choice of 12.5- $\mu\text{m}$  thickness is possible due to the high intensity of the flux from an imploded target. We show below that measuring an EXAFS spectrum through such a thick foil does not detract from our ability to study shocks launched into the foil. Specifically, the shock is quite uniform when its front has reached the back of the foil. This is important for an unambiguous interpretation of the absorption results. The choice of titanium (rather than a lower- $Z$  foil) results from the fact that with a high attenuation the detected spectrum is dominated by the second-order crystal diffraction (for which the attenuation is much smaller). In Ti the second-order radiation (around  $\sim 10$  keV) is too weak to affect the results.

(c) Using CID electronic detection rather than film. The CID array we used (from CID Technologies, Inc.) was an  $812 \times 604$  array having square pixels with 38.5- $\mu\text{m}$  center-to-center spacing, uncooled and with no conversion phosphor. The analog-to-digital converter with 16-bit resolution was fast enough to minimize the effect of dark current. The superior performance with respect to film is mainly due to the lower noise. CID arrays are more immune to radiation damage than CCD arrays; they have been extensively studied, implemented, and calibrated at LLE.<sup>9</sup>

The spectrum in Fig. 86.50 is spatially resolved in the vertical direction. Above the  $K$  edge, because of the strong attenuation, only the more intense radiation from the compressed core can be seen. Below the  $K$  edge the intensity is high enough to be seen over the whole target volume (and to saturate the core image). The spectrum without the absorber (i.e., the incident spectrum) is measured in parallel by employing additional filtering.

Figure 86.51 is a lineout through the calibrated spectrum, and it shows that the depth of modulation is indeed high. The choice of Ti foil thickness is about optimal for the available x-ray flux, as seen from the fact that the minimum intensity is close to zero.

The theory of EXAFS<sup>1</sup> yields an expression for  $\chi(k) = \mu(k)/\mu_0(k) - 1$ , where  $\mu(k)$  is the absorption coefficient (or opacity) and  $\mu_0(k)$  is the absorption of the isolated atom (i.e., without the EXAFS oscillations). By passing a smooth curve through the EXAFS oscillations,  $\mu_0(k)$  can be obtained (it is also known from published tables). The wave number  $k$  of the ejected photoelectron is given by  $\hbar^2 k^2 / 2m = E - E_K$ , where  $E$  is the absorbed photon energy and  $E_K$  is the energy of the  $K$  edge. Figure 86.52 shows the quantity  $\chi(k)$  derived from Fig. 86.51. The period and magnitude of the oscillations agree well with what is obtained in synchrotron experiments on Ti,<sup>10</sup> but the first peak is too high in comparison.

To assess the noise in the measured spectrum we compare successive spectra in adjacent rows of pixels (horizontal rows in Fig. 86.50). If  $S_i$  is the signal (or spectrum) of the  $i$ th row, the average signal  $S$  (such as was used in Fig. 86.51) is given by

$$S = \sum_{i=1}^m S_i / m, \quad (1)$$

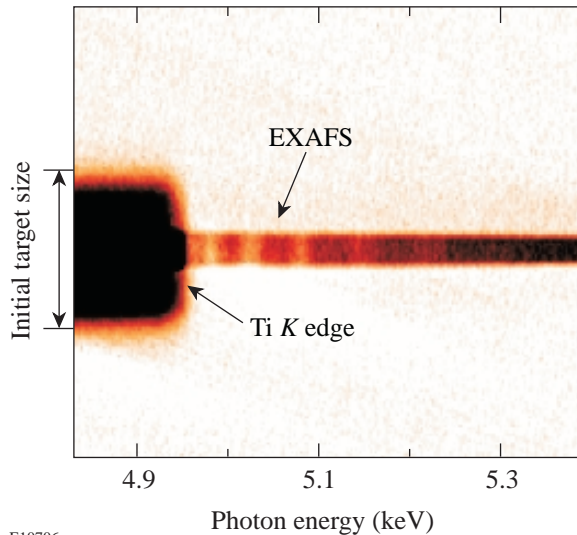


Figure 86.50  
EXAFS modulation spectrum obtained on a CID array (shot 21238) when the x rays from an OMEGA-imploded CH target are absorbed by a 12.5- $\mu\text{m}$ -thick Ti foil. Below the  $K$  edge the radiation from the entire target is strong enough to be seen; above the  $K$  edge only radiation from the compressed core is seen.

where we select  $m$  central rows within the spatial (vertical) profile to avoid edge effects. For the average noise  $N$ , using the same rows, we write

$$N = \sum_{i=1}^{m/2} (S_{2i-1} - S_{2i})/m. \quad (2)$$

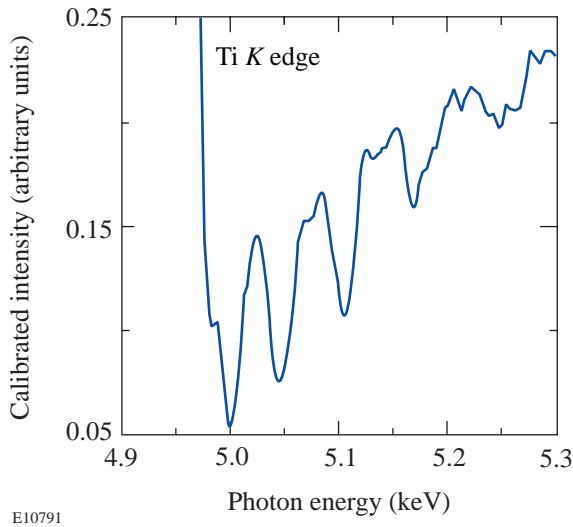


Figure 86.51  
The calibrated EXAFS signal for shot 21238 in arbitrary units. The relative depth of modulation is seen to be very high.

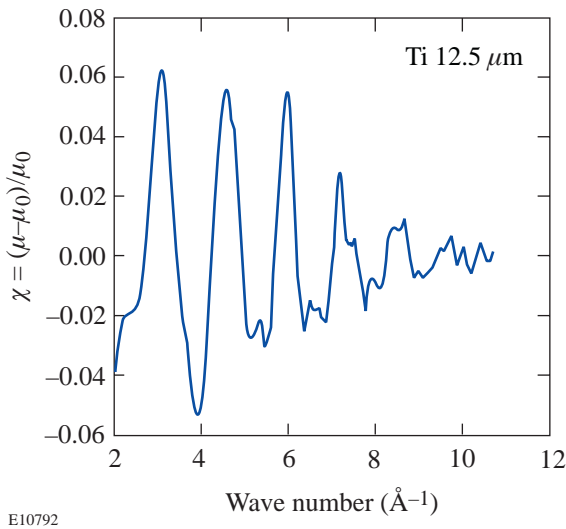


Figure 86.52  
Measured relative modulation of the absorption in Ti derived from Fig. 86.51 as a function of the wave number of the ejected electron (following  $K$ -shell photoionization).

The random components of the measured signal add up in Eq. (2), whereas the net signal cancels out; thus,  $N$  is the appropriate noise quantity to be compared with  $S$ . Figure 86.53 compares the signal (above the  $K$  edge) and the noise in the same units (pixel values). The signal is taken to be the modulations in Fig. 86.51 around a smooth average curve [the subtraction in Eq. (2) cancels out both this smooth curve and the EXAFS modulation around it]. The noise is seen to be negligible relative to the signal up to  $k \sim 10.5 \text{ \AA}^{-1}$ , beyond which the data is ignored.

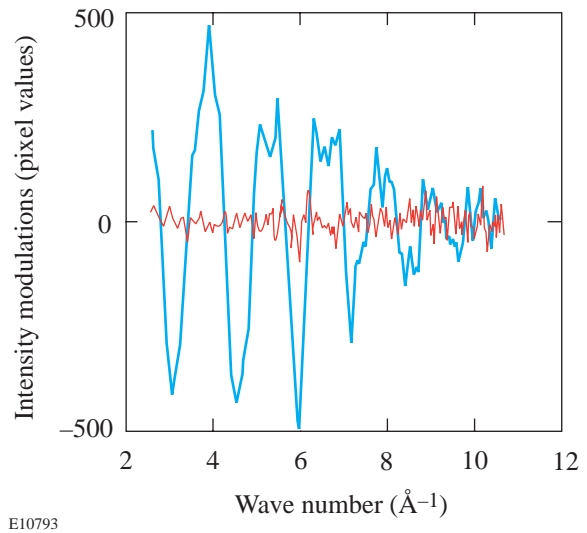


Figure 86.53  
Comparison of the EXAFS signal and noise using the results of Fig. 86.50 and Eqs. (1) and (2). The signal is given by the modulations in Fig. 86.51 around a smooth average curve.

### Theory of EXAFS

When photons of energy above the  $K$  edge (say, of Ti) are absorbed, a  $K$ -shell electron is ejected. In a solid material, the electron wave can be reflected from neighboring atoms and interfere with the outgoing electron wave. For different photon energies, the energy (and hence the wavelength) of the ejected electron will vary and so will the phase difference between the two waves. Thus, the interference translates into modulations in the cross section for photon absorption (i.e., the opacity). The period of the modulations is clearly related to the inverse of the interatomic distance and thus yields the density. The rate of decay of the modulations depends mostly on the temperature because at higher temperatures the ion-vibration amplitude increases, which causes a random phase shift of the reflected electron waves.

The basic theory yields the following expression for  $\chi(k)$ :

$$\chi(k) = \sum_j N_j F_j(k) \exp[-2\sigma^2 k^2 - 2R_j/\lambda(k)] \times \sin[2kR_j + \phi_j(k)]/kR_j^2, \quad (3)$$

where  $N_j$  is the number of atoms surrounding the absorbing atom at a distance  $R_j$  ( $N_1 = 12$  in Ti). The sum over  $j$  relates to the various shells of atoms around the photo-absorbing atom, in increasing distances. The backscattering amplitude  $F_j(k)$  and phase-shift factor  $\phi_j(k)$  for titanium were taken from the detailed calculations by Teo and Lee;<sup>11</sup> the mean free path of the ejected electron in titanium,  $\lambda(k)$ , was taken from the calculations of Blanche *et al.*<sup>10</sup> The vibration amplitude  $\sigma^2$  (the Debye-Waller factor) and the interatomic distances  $R_j$  are treated as adjustable parameters in fitting the experimental EXAFS spectrum to Eq. (3). The distances  $R_j$  (in particular  $R_1$ ) yield the density of the absorber. As discussed below,  $\sigma^2$  depends on both the temperature and the density; once the density is determined from  $R_1$ , the temperature can then be determined from  $\sigma^2$ . Equation (3) shows that the oscillations decay with increasing  $k$ , even if  $\sigma^2$  were negligibly small. For the temperatures of interest here, however, the decay is dominated by  $\sigma^2$ . In addition, an adjustable shift  $\Delta$  is introduced<sup>12</sup> in the  $K$ -edge energy because of solid-state effects at energies close to the edge. Equation (3) is based on some simplifying assumptions (such as plane rather than spherical electron waves and neglect of multiple scattering). More advanced theories<sup>13–15</sup> include such effects, but such improvements are not essential here because the shock compression will change the interatomic distance appreciably; thus a highly precise determination of the  $R_j$ 's is not required.

We next fit the experimental EXAFS spectrum to Eq. (3). The customary procedure is to work with the function  $k\chi(k)$  [or even  $k^3\chi(k)$ ] rather than  $\chi(k)$ . By doing so we place less weight on the low- $k$  part of the spectrum, where the theory is uncertain. Also, to simplify the fitting, we use only the first term ( $j = 1$ ) in Eq. (3). The equivalent experimental spectrum is obtained in the following manner. First, the experimental spectrum is Fourier transformed to the  $R$  space. The amplitude of the Fourier transform of  $\chi(k)$  gives the charge distribution around an absorbing Ti atom.<sup>1</sup> Simply put, a constructive interference occurs when the interatomic distance equals an integer multiple of half the electron wavelength. Figure 86.54 shows this distribution for the two consecutive laser shots analyzed in this article. The distribution is seen to be reproducible, and it agrees

well with the published data on Ti obtained with synchrotron radiation.<sup>10,15</sup> The major peak is due to the nearest neighbors around the absorbing atom, whereas the minor peak is due to the next shell of neighboring atoms.

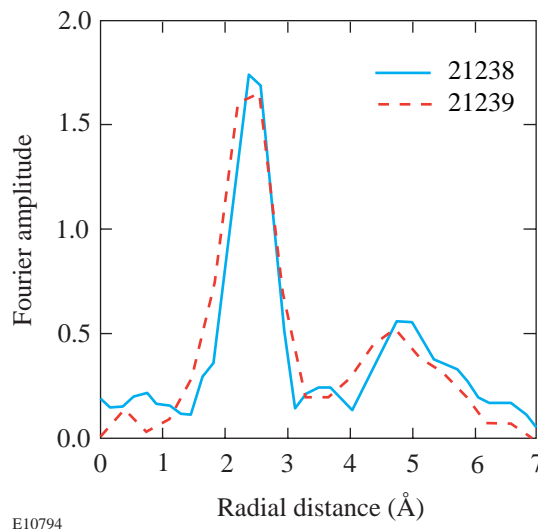


Figure 86.54

Amplitude of the Fourier transform of the EXAFS spectrum  $\chi(k)$  for two consecutive laser shots. The transform corresponds to the charge distribution around the photon-absorbing Ti atom. The weaker peak is particularly sensitive to reduction in short-range order due to melting.

In addition to crystalline materials, EXAFS has been measured in amorphous materials<sup>2,3</sup> as well as in liquids.<sup>4–6</sup> As compared with crystals, the amplitude of modulations in the absorption coefficient is lower; in addition, in the  $R$  space, the farther-shell peaks are reduced more than the nearest-neighbor peak. This provides a method for detecting melting. Of particular importance in these studies is the demonstrated ability to observe the minor peak since it is more sensitive to melting or to any change in short-range order. The main peak in Fig. 86.54 is selected by multiplying the distribution by a super-Gaussian filter centered on that peak. Finally a transform back to the  $k$  space is performed. This procedure is sufficient for determining the temperature and density. The range of 2 to 10.5  $\text{\AA}^{-1}$  was used to analyze  $k\chi(k)$ . Below 2  $\text{\AA}^{-1}$  the curve is negligibly small; above  $k \sim 10.5 \text{\AA}^{-1}$  the EXAFS spectrum is limited by noise.

Figure 86.55 shows the best fit, with  $R_1 = 2.9 \text{\AA}$ ,  $\sigma^2 = 0.0049 \text{\AA}^2$ , and  $\Delta = -13 \text{ eV}$ . These values agree with the results found for Ti in synchrotron-radiation experiments.<sup>15</sup> The experimental spectrum  $k\chi(k)$  had to be multiplied by a factor  $\sim 1.8$  to normalize it to the theoretical spectrum. This is consistent

with what is found in other EXAFS studies:<sup>16</sup> Rehr *et al.*<sup>16</sup> have shown that the relaxation of bound electrons that accompanies the ejection of *K*-shell electrons reduces the EXAFS amplitude from Eq. (3) by about a factor of 2. The quality of the fit can be improved if more-sophisticated versions of the theory are used. As explained above, however, this is not required in these studies.

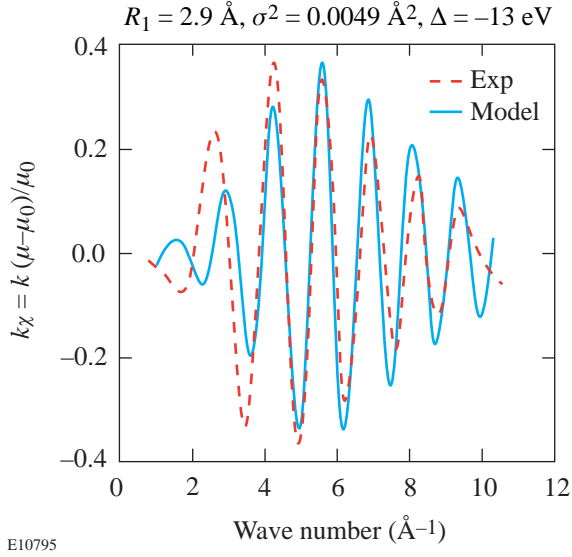


Figure 86.55

Fitting the model [Eq. (3)] to the observed EXAFS  $k\chi(k)$  spectrum. Shown are the parameter values giving the best fit. The interatomic distance  $R_1$  depends on the density, and the Debye–Waller factor  $\sigma^2$  depends mostly on the temperature.  $\Delta$  is an adjustable shift applied to the *K*-edge energy to account for solid-state effects.

## EXAFS Visibility

### 1. Dependence of $\sigma^2$ on Temperature and Density

As seen from Eq. (3), when the temperature (and thus  $\sigma^2$ ) increases, the EXAFS modulations decay faster with  $k$  and may become useless for diagnosing the target. To determine the useful temperature range for EXAFS observation we use the calculated dependence<sup>17</sup> of  $\sigma^2$  on temperature:

$$\sigma^2 = \frac{3\hbar^2}{Mk\Theta_D} \left[ \left( \frac{1}{4} \right) + \left( \frac{T}{\Theta_D} \right)^2 \int_0^{\Theta_D/T} \frac{x dx}{e^x - 1} \right], \quad (4)$$

where  $M$  is the atomic mass. Equation (4) was derived using a Debye model of lattice oscillations in a cubic, perfect crystal. It assumes harmonic oscillations so its validity is restricted to low temperatures. It also assumes uncorrelated vibrations of the absorbing and neighboring atoms. This correlation gives

rise to an additional term<sup>17</sup> in Eq. (4), which we have neglected. Studies of the correlation<sup>18,19</sup> show that it reduces  $\sigma^2$  by a about a factor  $\sim 1.6$  around room temperatures; this correction factor was incorporated in subsequent calculations at all temperatures. Figure 86.56 shows the dependence of the corrected  $\sigma^2$  on temperature for Ti at solid density. At room temperature the value of  $\sigma^2$  ( $\sim 0.005 \text{ \AA}^2$ ) agrees with the value found from the present experiment (Fig. 86.55), which also agrees with the results of synchrotron experiments on Ti.<sup>10</sup>

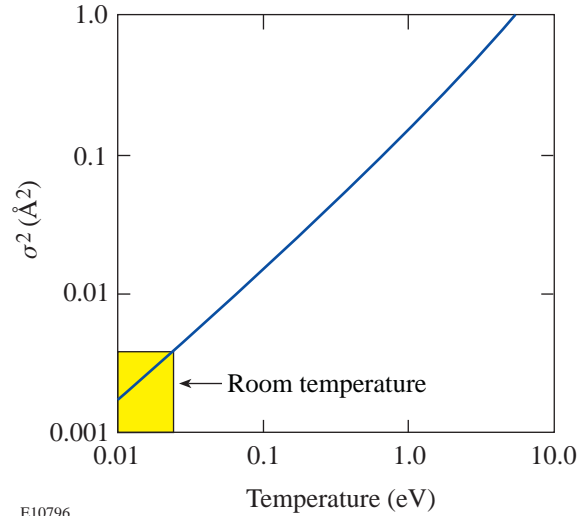


Figure 86.56

The dependence of the vibration amplitude  $\sigma^2$  (corrected for correlation) on temperature for solid Ti density.

Although the increased temperature due to the shock increases  $\sigma^2$  and reduces the EXAFS visibility, the increased density behind the shock *decreases*  $\sigma^2$  because  $\sigma^2$  depends on  $T/\Theta_D$  and  $\Theta_D$  increases with density. The latter can be understood by noting that  $\Theta_D$  is related to  $k_D$ , the maximum wave number of phonon vibrations, which changes as  $R^{-1}$ ; thus, shock compression reduces  $R$  and increases  $\Theta_D$ .

The density dependence of  $\Theta_D$  can be determined from an empirical model<sup>20</sup> due to Cowan, in terms of the nuclear charge  $Z$  and the atomic weight  $A$ . The result is

$$k\Theta_D = [1.68/(Z + 22)] \left[ \xi^{b+2} / (1 + \xi)^2 \right] \text{eV}, \quad (5)$$

where

$$b = 0.6 Z^{1/9}, \quad \xi = \rho / \rho_{\text{ref}}, \quad \rho_{\text{ref}} = (A/9Z^{0.3}) \text{g/cm}^3. \quad (6)$$

Figure 86.57 shows the dependence of the Debye temperature of Ti on the density;  $\rho_s$  is the solid density. At solid density  $\Theta_D$  of Ti is 0.0366 eV;<sup>21</sup> the model overestimates this value by about 15%, so we reduce the model-calculated  $\Theta_D$  by that factor. Because  $\sigma^2$  depends on both temperature and density, both parameters must be determined as a function of shock strength in order to assess the expected EXAFS visibility.

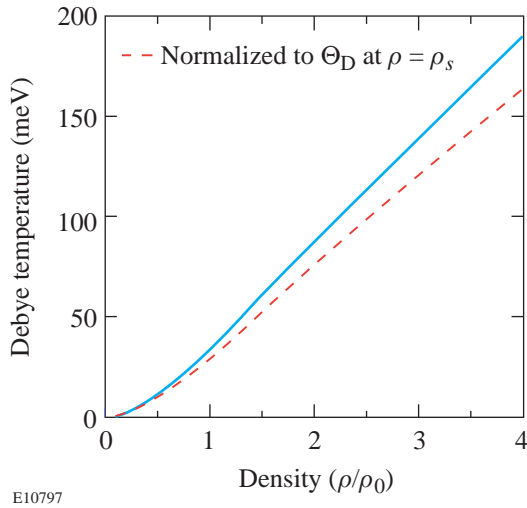


Figure 86.57  
Calculated dependence of the Debye temperature of Ti on compression using Cowan's model.<sup>20</sup> The dashed curve is normalized to the known  $\Theta_D$  of Ti at solid density  $\rho_s$ .

## 2. Dependence of Density and Temperature on Shock Strength

In future experiments the Ti foil will be embedded in a double CH layer and driven by a single laser beam, while still backlit by a spherically imploded target. The front CH layer will be thick enough to ensure that no burnthrough occurs before the shock traverses the Ti layer; the role of the rear-surface CH layer is to avoid extraneous effects due to unloading of the shock when arriving at the target–vacuum interface. The parameter space where high-amplitude EXAFS oscillations can be expected to be observed is now estimated. As seen above, both temperature and density achieved by shock compression of Ti as a function of laser irradiance must be determined by (a) using the experimentally known<sup>22</sup> Hugoniot of Ti and (b) simulating the interaction with the 1-D code *LILAC*. In these simulations a 10- $\mu\text{m}$ -thick Ti layer was assumed to be coated on each side by a 5- $\mu\text{m}$ -thick CH layer and irradiated by a 1-ns square pulse of various powers. These simulations also determine the uniformity behind the shock over a thick Ti layer.

This requirement is essential for an unequivocal interpretation of the EXAFS results. The *LILAC* simulations (see examples in Fig. 86.58) show that when the shock arrives at the back surface of the Ti layer, the temperature and density within the layer are uniform to within  $\pm 10\%$  and the Ti layer is unaffected by rarefaction.

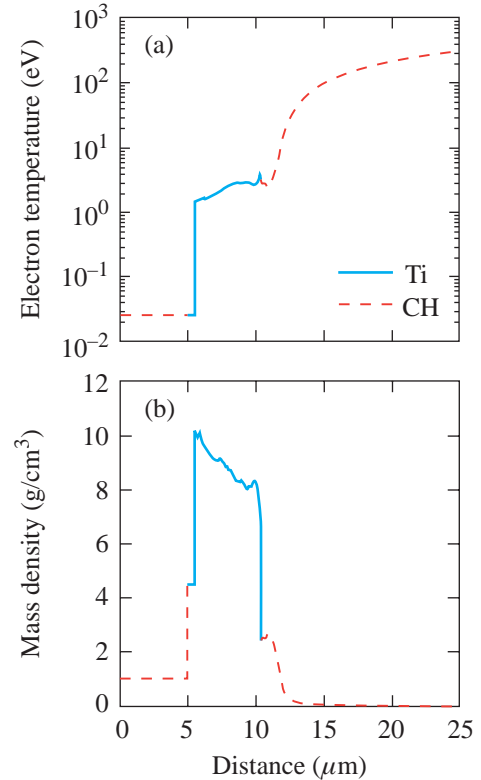


Figure 86.58  
Example of *LILAC* simulations of a shock wave in a 10- $\mu\text{m}$ -thick Ti layer sandwiched between two 5- $\mu\text{m}$ -thick CH layers, produced by a 1-ns square pulse at 20 TW/cm<sup>2</sup>. The density and temperature profiles are shown for the instant the shock arrives at the back surface of the Ti layer.

*LILAC* was run for a series of increasing values of laser intensity, and in each case the density and temperature (averaged over the Ti layer) were determined at the instant the shock arrived at the back surface of the Ti layer. The results are shown in Fig. 86.59 (for the density) and in Fig. 86.60 (for the temperature) as points marked by the value of laser intensity in TW/cm<sup>2</sup>. In parallel to these simulations the density and temperature were determined from experimentally known data. In Fig. 86.59, the red curve shows the measured principal Hugoniot of Ti.<sup>22</sup> Although the curves are shown over a wide pressure range, the main interest here is in their low-pressure portion; thus, the melting temperature of Ti at solid density is at 1941°K, or 0.167 eV.

Using the Hugoniot curve, we now determine the temperature in the shocked Ti layer. First, from the Rankine–Hugoniot relation

$$E - E_0 = (P/2) \left[ (1/\rho_0) - (1/\rho) \right] \quad (7)$$

we determine the energy increase due to the shock. Here  $E$ ,  $P$ , and  $\rho$  are the energy per unit mass, the pressure, and the density behind the shock front, and the subscripted quantities refer to the region in front of the shock front ( $P_0 = 0$  was assumed). From the energy increase  $E - E_0$  we calculate the temperature behind the shock front, using the quotidian equations of state for ions and electrons described in Ref. 20. For the ions, the energy per ion above  $\Theta_D$  is given by

$$E_i = 3kT \left[ 1 + (u^2/20) - \dots \right], \quad u = \Theta_D(\rho)/T. \quad (8)$$

For temperatures much higher than  $\Theta_D$ , as is the case here, this reduces to  $E_i = 3kT$  (the Dulong–Petit law). For the electrons, a modified Fermi–Thomas (FT) equation of state is used.<sup>23</sup> The FT theory at low temperatures yields too high an electron pressure ( $\sim$ Mbars) because the bonding between adjacent atoms is neglected and must be corrected. In a convenient semi-empirical correction method devised by Barnes<sup>24</sup> an

expression for the bonding energy  $\Delta E$  (negative for densities higher than solid) is added to the electron energy.  $\Delta E$  (energy per  $\text{cm}^3$ ) is given by

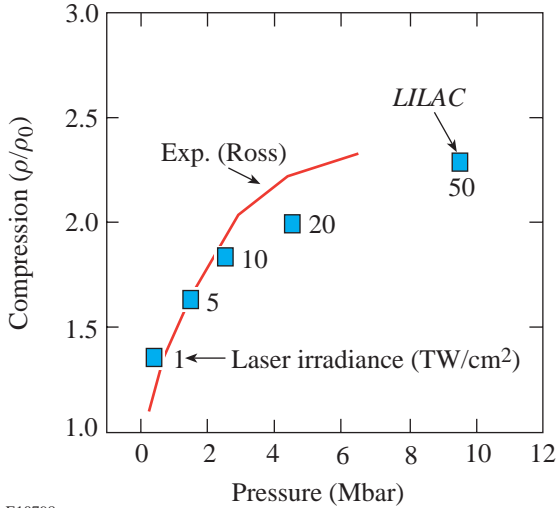
$$\Delta E = E_0 \left\{ 1 - \exp \left[ b - b(\rho_s/\rho)^{1/3} \right] \right\}, \quad (9)$$

where  $\rho_s$  is the solid density and  $E_0$  and  $b$  are adjustable parameters. To be consistent with thermodynamic relations, this change in energy must be accompanied with a change in pressure given by

$$\begin{aligned} \Delta p &= \rho^2 \frac{\delta \Delta E}{\delta \rho} \\ &= - \left( \frac{E_0 b \rho_s}{3} \right) \left( \frac{\rho}{\rho_s} \right)^{2/3} \exp \left[ b - b \left( \frac{\rho_s}{\rho} \right)^{1/3} \right], \end{aligned} \quad (10)$$

and the revised bulk modulus becomes

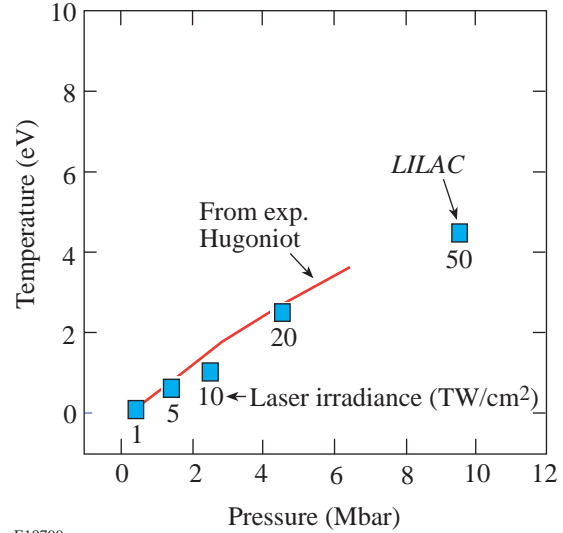
$$B = \rho (\delta p_e / \delta \rho)_{\rho_s} - (b + 2)(E_0 b \rho_s) / 9. \quad (11)$$



E10798

Figure 86.59

Experimentally determined<sup>22</sup> principal Hugoniot in Ti (red curve). The points were obtained from *LILAC* code simulations of a shock created when a laser of the shown irradiance (in  $\text{TW}/\text{cm}^2$ ) irradiated the buried-Ti target.



E10799

Figure 86.60

Temperature behind the shock as a function of the shock pressure in Ti (red curve) calculated from the known principal Hugoniot and the corrected Fermi–Thomas equation of state. The points were obtained from *LILAC* code simulations of a shock created when a laser of the shown irradiance (in  $\text{TW}/\text{cm}^2$ ) irradiated the buried-Ti target.

Here we neglected the ion pressure  $p_i$ . Using these two relations for the energy and the pressure,  $E_0$  and  $b$  are found from the following two conditions: (a) the corrected pressure  $p + \Delta p$  (where  $p$  is the Fermi–Thomas pressure) at solid density and  $T = 0$  should be 0, and (b)  $B$  should agree with the known bulk modulus at normal temperature and density (for Ti,  $B$  equals<sup>25</sup>  $1.1 \times 10^{12}$  dyn/cm<sup>2</sup>). We now add  $\Delta E$  from Eq. (9), with  $E_0$  and  $b$  thus determined, to the Fermi–Thomas energies<sup>23</sup> for Ti, using for the latter the fitting expressions worked out by Bell.<sup>26</sup> Using Eq. (7), the energy along the experimental Hugoniot (Fig. 86.59) can be calculated. We now equate these energy values with the revised Fermi–Thomas energies. Since these energies depend on density and temperature, using the known densities (Fig. 86.59), we can now search for the temperatures along the Hugoniot. The results are shown as a red curve in Fig. 86.60. Good agreement between the *LILAC* simulations and the experiment-based model is seen in Figs. 86.59 and 86.60, especially for the low-pressure range of relevance in this study.

### 3. EXAFS Visibility as a Function of Shock Strength

Finally, the vibration amplitude  $\sigma^2$  can be determined as a function of shock strength from Figs. 86.59 and 86.60, using Eqs. (4) and (5). The results, over the range of pressures of the experimental Hugoniot, are shown in Fig. 86.61. Using Eq. (3) we can show that significant EXAFS modulations can be seen whenever  $\sigma^2 \leq 0.1$ , so Fig. 86.61 indicates that such modulations in forthcoming shock experiments are expected to show significant amplitude. It should be noted, however, that the density affects the EXAFS visibility directly, in addition to affecting it through  $\sigma^2$ . Thus, at a higher density the modulation amplitude increases because of the appearance of the interatomic distance  $R$  in the denominator of Eq. (3). On the other hand, at a higher density the period of the EXAFS oscillations increases, and there are fewer oscillation periods within the range of  $k$  where their amplitude is significant. To demonstrate these effects, the EXAFS spectrum calculated from Eq. (3) was plotted in Fig. 86.62 for two conditions: (a)  $\sigma^2 = 0.04 \text{ \AA}^2$  at solid density. From Fig. 86.56 this corresponds to  $T \sim 0.25$  eV, just above the melting point. Significant EXAFS modulations are seen for this case. (b)  $\sigma^2 = 0.1 \text{ \AA}^2$  at  $2.5 \times$  solid density. This represents an extreme case where  $\sigma^2$  is higher than what will be encountered in these experiments (see Fig. 86.61). The EXAFS spectrum in this case is only marginally useful, especially for determining the density; however, it can still provide a good indication of the temperature. Finally, in calculating the expected EXAFS spectrum we have not included the effect of noncrystallinity, which would modify Eq. (3). Experiments on EXAFS in molten metals [see, e.g.,

Ref. 6(b)] show that the modulation amplitude upon melting is reduced by about a factor of 1.5. Thus, the conclusions reached above should not change significantly when melting is included in the analysis.

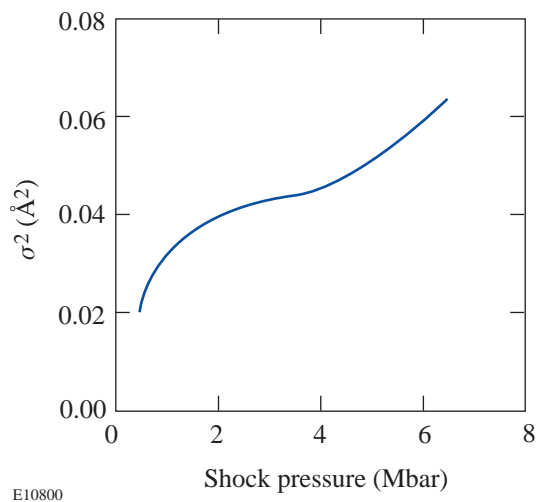


Figure 86.61  
The vibration amplitude  $\sigma^2$  as a function of shock strength, calculated from Figs. 86.59 and 86.60, using Eqs. (4) and (5).

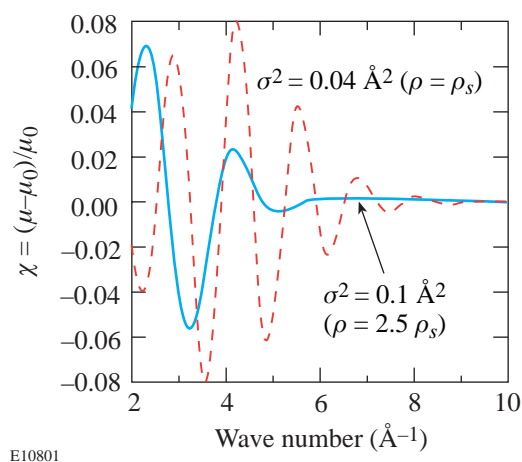


Figure 86.62  
Demonstration of the effects of  $\sigma^2$  and the density on the EXAFS spectrum in Ti. The density affects the spectrum both directly and through  $\sigma^2$ .

## ACKNOWLEDGMENT

This work was supported by the U.S. Department of Energy Office of Inertial Confinement Fusion under Cooperative Agreement No. DE-FC03-92SF19460, the University of Rochester, and the New York State Energy Research and Development Authority. The support of DOE does not constitute an endorsement by DOE of the views expressed in this article.

## REFERENCES:

1. P. A. Lee *et al.*, *Rev. Mod. Phys.* **53**, 769 (1981).
2. M. C. Ridgway *et al.*, *Nucl. Instrum. Methods Phys. Res. B* **147**, 148 (1999).
3. D. E. Sayers, E. A. Stern, and F. W. Lytle, *Phys. Rev. Lett.* **27**, 1204 (1971).
4. Y. Katayama, O. Shimomura, and K. Tsuji, *J. Non-Cryst. Solids* **250–252**, 537 (1999).
5. K. Tamura *et al.*, *J. Non-Cryst. Solids* **150**, 351 (1992).
6. E. D. Crozier, in *EXAFS Spectroscopy: Techniques and Applications*, edited by B. K. Teo and D. C. Joy (Plenum Press, New York, 1981), Chap. 6, p. 89; E. D. Crozier and A. J. Seary, *Can. J. Phys.* **58**, 1388 (1980).
7. R. W. Eason *et al.*, *J. Phys. C, Solid State Phys.* **17**, 5067 (1984); B. A. Shiwai *et al.*, *Laser Part. Beams* **10**, 41 (1992).
8. B. Yaakobi, F. J. Marshall, D. K. Bradley, J. A. Delettrez, R. S. Craxton, and R. Epstein, *Phys. Plasmas* **4**, 3021 (1997).
9. F. J. Marshall, T. Ohki, D. McInnis, Z. Ninkov, and J. Carbone, *Rev. Sci. Instrum.* **72**, 713 (2001).
10. G. Blanche *et al.*, *Ultramicroscopy* **50**, 141 (1993).
11. B.-K. Teo and P. A. Lee, *J. Am. Chem. Soc.* **101**, 2815 (1979).
12. See Ref. 1, Sec. IV(B); Ref. 15, p. 6358.
13. P. A. Lee and J. B. Pendry, *Phys. Rev. B* **11**, 2795 (1975).
14. J. J. Rehr and R. C. Albers, *Rev. Mod. Phys.* **72**, 621 (2000).
15. A. Balzarotti, M. De Crescenzi, and L. Incoccia, *Phys. Rev. B* **25**, 6349 (1982).
16. J. J. Rehr *et al.*, *Phys. Rev. B* **17**, 560 (1978); see also Ref. 1, Sec. III(G).
17. G. Beni and P. M. Platzman, *Phys. Rev. B* **14**, 1514 (1976).
18. R. B. Gregor and F. W. Lytle, *Phys. Rev. B* **20**, 4902 (1979).
19. G. Dalba and P. Fornasini, *J. Synchrotron Radiat.* **4**, 243 (1997).
20. R. M. More *et al.*, *Phys. Fluids* **31**, 3059 (1988).
21. R. E. Bolz and G. L. Tuve, eds. *CRC Handbook of Tables for Applied Engineering Science*, 2nd ed. (CRC Press, Boca Raton, FL, 1973), Chap. 2.2, p. 231.
22. M. Ross, *Rep. Prog. Phys.* **48**, 1 (1985).
23. R. Latter, *Phys. Rev.* **99**, 1854 (1955).
24. J. F. Barnes, *Phys. Rev.* **153**, 269 (1967).
25. G. V. Samsonov, ed. *Handbook of the Physicochemical Properties of the Elements* (IFI/Plenum, New York, 1968), Chap. VI, p. 397.
26. A. R. Bell, Rutherford and Appleton Laboratories, Chilton, Didcot, Oxon, England, Report RL-80-091 (1980).

---

# Microhardness and Indentation Fracture of Potassium Dihydrogen Phosphate (KDP)

## Introduction

Potassium dihydrogen phosphate (KDP) is an important electro-optic tetragonal crystal. For example, it is used as a photonic material in the third-harmonic generation (THG) to reduce light wavelength from 1.054  $\mu\text{m}$  to 351 nm. Microindentation has been used to measure the Vickers and Knoop hardness of KDP and the resulting cracking on (100) and (001) faces. Hardness anisotropy on the (001) face, or among the (100) and (001) faces, was found to be small (about 20%). An indentation size effect for both Vickers and Knoop hardness for indenting loads in the range of 25 to 200 g was observed. The large-load Vickers hardness was estimated as  $1.4 \pm 0.1$  GPa. Anisotropy in the crack sizes on (100) and (001) faces was also observed. Cracks were longer on (100) faces, scaling like  $c \sim P^{2/3}$ ; cracks on (001) faces were shorter, scaling like  $c \sim P^{1/2}$ . Assuming elastic and plastic isotropy, crack sizes were analyzed and fracture toughness  $K_c$  was extracted. An approximate model for analyzing crack-load microindentation data in tetragonal crystals is presented in this article. The model uses the minimum elastic modulus of the material. The effect of the isotropy assumption on the extracted fracture toughness is estimated at about 33%, with a 23% contribution from elastic anisotropy and 10% from the slip system plastic anisotropy. Strain-rate effects are identified as important aspects of KDP deformation, especially in laser damage applications.

One of the limiting factors in the use of KDP in THG is its susceptibility to laser damage, a process that couples light absorption with thermal and mechanical effects. (For a summary of the electro-optical properties, see Milek and Neuberger.<sup>1</sup>)

KDP crystals are water soluble and brittle. Above its ferroelectric Curie temperature (123 K) the crystal structure of KDP is tetragonal, lacking a center of inversion. KDP is optically uniaxial with the optic axis along the tetragonal  $z$  axis or [001] direction. At room temperature the lattice constants are  $a = 0.7453$  nm and  $c = 0.6975$  nm, as cited in Ref. 1. The natural habit of crystals grown from solution is a tetragonal prism combined with a tetragonal bipyramid. The prism faces are (100) and (010) planes. The prism axis is [001].

KDP is relatively soft and brittle as compared to other optical materials, including glasses. In this article microhardness and indentation cracking fracture measurements of KDP indented on crystal planes (100) and (001) are summarized.

Kishan Rao and Sirdeshmukh<sup>2</sup> measured the Vickers microhardness of KDP at loads of 50 and 100 g, reporting a value of  $H_v = 1.43$  GPa for indentation normal to {100} planes (what they called “ $a$ -direction”) and 1.29 GPa for indentation normal to {001} planes (“ $c$ -direction”). Their error was reported as  $\pm 4\%$ . Anbukumar *et al.*<sup>3</sup> also measured the Vickers hardness of {100} planes of KDP. They reported hardness in the range of 1.77 to 1.57 GPa for loads in the range of 5 to 50 g and an indentation size effect (ISE) where the hardness decreased with increased load.

Shaskol'skaya *et al.*<sup>4</sup> and Guin *et al.*<sup>5</sup> reported measurements of both hardness and cracking in the Vickers measurements of KDP and  $\text{KD}_{2x}\text{H}_{2-2x}\text{PO}_4$  (deuterated KDP, with  $x = 0$  to 0.95). They used loads of 50 to 200 g and reported a hardness reduction from 1.44 GPa to 1.22 GPa as the extent of deuteration  $x$  increased from 0 to 0.95. Shaskol'skaya *et al.*<sup>4</sup> also measured the length of cracks (tip-to-tip distance  $2c$ ) due to Vickers indents. They observed that  $(2c)/D$  varied from 3.87 to 3.61 as  $x$  increased from 0 to 0.95. They also reported a value of 51 MPa for the microstrength  $P/(2c)^2$  of both KDP and 95% deuterated KDP.

Guin *et al.*<sup>5</sup> reported measurements similar to those of Shaskol'skaya.<sup>4</sup> They also identified two types of slip systems in KDP: the first system consisted of slip planes (110), (101), (112) and (123) with a common Burgers vector  $\langle 111 \rangle / 2$ ; the second slip system was identified as (010)[100].

More recently, Marion<sup>6</sup> has reported measured values of fracture toughness in KDP crystals. Marion apparently used the direct crack method described by Anstis *et al.*,<sup>7</sup> although the measured data were not described. Marion<sup>6</sup> reported fracture toughness  $K_c$  of 0.2  $\text{MPa}\cdot\text{m}^{1/2}$ , as well as 0.09  $\text{MPa}\cdot\text{m}^{1/2}$  along the weakest direction (longest crack). No crystallo-

graphic orientation of the indented faces was reported, however, nor was the applicable elastic constant (modulus) given.

Given the importance of KDP in third-harmonic generation for 351-nm-wavelength laser systems, a systematic study of indentation hardness (Vickers and Knoop) and microindentation cracking in KDP is described below.

### Measurements

Vickers indentation was used to measure the indentation size effect on  $H_V$  and also to extract the fracture toughness from the measured dependence of crack size on indenting load. Vickers hardness on (100), (010), and (001) planes of single-crystal KDP was measured at room temperature with a Tukon Microhardness Tester equipped with a video image-capture camera. Typical descent rate of the indenter is about 1 mm/min.

The KDP crystal was provided by a commercial vendor and had been grown from the solution. The crystal surfaces were polished by conventional means with nonaqueous slurries to optical standards. Although surface roughness was not directly measured, it was estimated to be approximately 3 to 5 nm (rms).

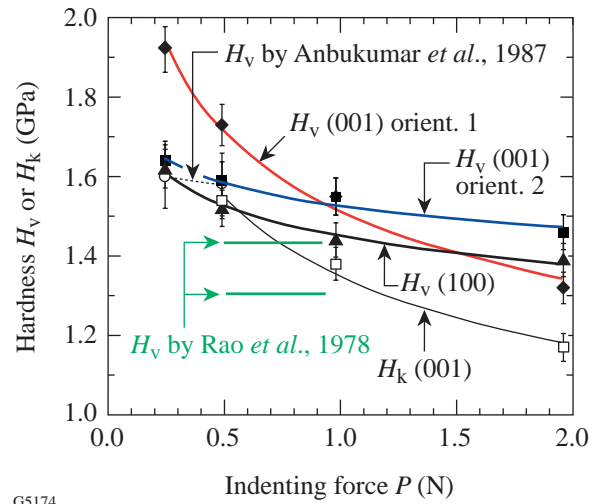
The indentation load was in the range of 2 to 200 g, and each load was applied for 15 s. Five indentations were performed at each load. The indentation diagonal  $D$  and crack size  $2c$  (tip-to-tip distance) were measured with an optical microscope with a 50 $\times$  objective lens. For the Vickers indentation of (100) and (010) planes, the indenter diagonals were along the principal directions of the type  $\langle 100 \rangle$ . No differences were observed in the indentation diagonal or crack size of (100) and (010) faces.

For the indentation of (001) planes, we selected two indenter orientations: in orientation (1), the indenter diagonals were parallel to [100] and [010]; in orientation (2), the indenter sides were along [100] and [010].

Figure 86.63 shows the measured hardness over the range of indenting loads used. Figure 86.64 shows the measured crack size for Vickers indentation of (100) and (001) faces. The crack-to-indent ratio  $c/(D/2)$  varied from 2 to 4.5, depending on load and orientation.

Knoop indentation was used to measure the indentation size effect on Knoop hardness and also the hardness anisotropy of the (001) faces. For the indentation size effect (loads of 50 to

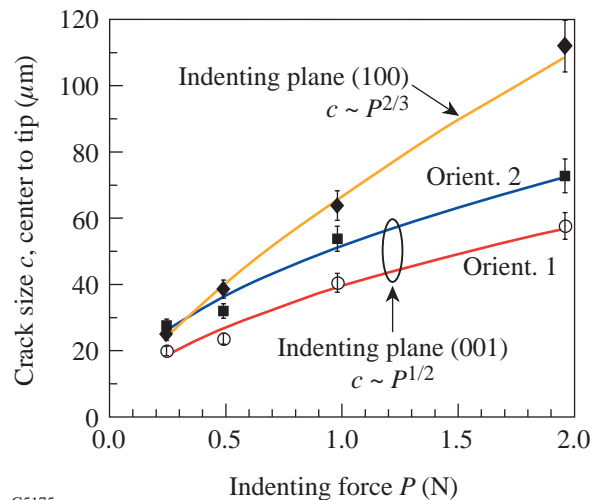
200 g), the indenter's long diagonal was along [010]. These results are included in Fig. 86.63.



G5174

Figure 86.63

Variation of measured hardness (Vickers and Knoop) with load for KDP at room temperature. Vickers indentation was done on faces (100) and on indenter orientations (1) and (2) on the (001) faces. Orientation (1) had the indent diagonals parallel to (100) and (010). Orientation (2) had the indent edges parallel to (100) and (010). Also shown are Vickers measurements by Anbukumar *et al.*<sup>3</sup> and Rao *et al.*<sup>2</sup> Guin *et al.*<sup>5</sup> reported Vickers hardness 1.45 GPa at 200 g.



G5175

Figure 86.64

Variation of indentation crack size  $c$  with indenting load. The tip-to-tip surface crack length is  $2c$ .

For the hardness anisotropy, we used a load of 50 g and measured the variation of  $H_k$  with orientation  $\theta$  of the Knoop indenter with respect to the indented surface. Angle  $\theta = 0^\circ$  corresponds to the indenter long diagonal along the [010] direction. The angle  $\theta$  was changed in increments of  $10^\circ$  from  $\theta = 0^\circ$  to  $90^\circ$ . The hardness anisotropy is shown in Fig. 86.65.

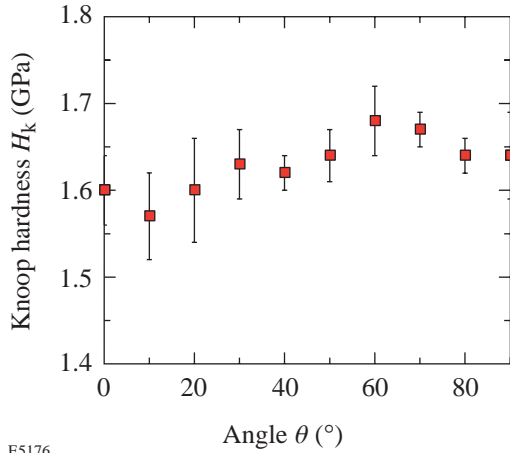


Figure 86.65  
Dependence of Knoop hardness on angle  $\theta$  of indent on the (001) plane.  $\theta = 0$  corresponds to the Knoop diagonals being along (100) and (010).

**Results**

The measured Vickers hardness is seen to vary between 1.7 and 1.4 GPa over the indenting load range of 50 to 100 g. This hardness range is consistent with the measurements of Rao *et al.*<sup>2</sup> over the same load range. Our measurements are also consistent with those of Anbukumar *et al.*<sup>3</sup> over the load range of 25 to 50 g, and with Guin *et al.*<sup>5</sup> and Shaskol'skaya *et al.*<sup>4</sup> who reported a hardness of 1.45 GPa at a load of 200 g.

The measured Vickers hardness brings up two questions: What is the relative hardness of (100) and (001) faces? What is the relative hardness of orientations (1) and (2) of the indenter on face (001)?

Our results show that for loads less than 150 g, (001) faces are harder than (100) faces by as much as 14% at lower loads. On (001) faces, orientation (1) is harder than orientation (2), by as much as 10%. At loads of about 200 g, however, both faces and both orientations have hardness in the range  $1.4 \pm 0.1$  GPa; therefore, this value may be used as the load-independent, orientation-insensitive Vickers hardness of KDP.

Our results also show that the Knoop hardness on the (001) face is not strongly anisotropic. The variation of hardness with direction is seen to be less than 10%.

No analysis is available to convert measured micro-indentation crack sizes to fracture toughness in tetragonal crystals. The only available analysis is for isotropic materials, such as glasses or polycrystalline ceramics (see Ref. 8). Therefore, to convert our direct measurements of indentation crack size to a fracture toughness, we shall assume that KDP can be described by an equivalent isotropic Young's modulus  $E = 38.7$  GPa. This value is the mean of the Reuss and Voigt averages for the Young's modulus, with the derivation presented in the Appendix. We have analyzed the microindentation crack measurements (indentation diagonal  $D$ , tip-to-tip crack size  $2c$ ) using the model of Evans<sup>9</sup> and Anstis *et al.*<sup>7</sup> The comparative merits and applicability of various models to extract the fracture toughness by microindentation cracking in optical glasses and brittle ceramics have been discussed by Ponton and Rawlings<sup>10,11</sup> and Lambropoulos *et al.*<sup>12</sup>

Evans<sup>9</sup> used dimensional analysis and curve fitting over a range of  $c/(D/2)$  from 1.5 to 7 and for many polycrystalline ceramic materials; thus, this model should be applicable to both short and long indentation cracks. According to the Evans model,<sup>9</sup>

$$K_c = H\sqrt{D/2} \left(\frac{E}{H}\right)^{0.4} 10^{f(x)}, \quad x = \log_{10}\left(\frac{c}{D/2}\right), \tag{1}$$

$$f(x) = -1.59 - 0.34x - 2.02x^2 + 11.23x^3 - 24.97x^4 + 16.23x^5,$$

where  $K_c$  is the fracture toughness,  $H$  is the hardness,  $D$  is the indentation diagonal,  $E$  is the Young's modulus, and  $c$  is the half-crack size. Lankford<sup>13</sup> included  $Al_2O_3$ , soda-lime silicate glass, and NaCl to the materials analyzed by Evans.<sup>9</sup>

Anstis *et al.*<sup>7</sup> examined various glasses (glass-ceramic, soda-lime, aluminosilicate, lead alkali), polycrystal  $Al_2O_3$  and sapphire,  $Si_3N_4$ , SiC, Ca-PSZ  $ZrO_2$ , Si, and SiC/Co and concluded that

$$K_c = (0.016 \pm 0.002) \left(\frac{E}{H}\right)^{1/2} \frac{P}{c^{3/2}}. \tag{2}$$

The Anstis model is based on the assumption that the observed surface cracks are surface traces of sufficiently large radial cracks, so that  $c \sim P^{3/2}$ . On the other hand, the Evans model is applicable for both shorter near-surface cracks, where  $c \sim P$ , and deeper radial cracks.

As an example of this approach, when the data by Shaskol'skaya *et al.*<sup>4</sup> or Guin *et al.*<sup>5</sup> are analyzed via the Evans model and with  $E = 38.7$  GPa, they yield  $K_c = 0.24 \pm 0.04$  MPa.m<sup>1/2</sup> at the indentation load of 200 g. The Anstis model leads to  $K_c = 0.17 \pm 0.03$  MPa.m<sup>1/2</sup> over the same increase of indentation load. The Anstis model predictions are in agreement with the reported values of 0.09 to 0.20 MPa.m<sup>1/2</sup> by Marion.<sup>6</sup> Note, however, that the work of neither Shaskol'skaya *et al.*<sup>4</sup> nor Guin *et al.*<sup>5</sup> describes the orientation of the indented planes or the orientation of the indenter with respect to the indented plane.

The results of our data analysis using the Evans model are shown in Fig. 86.66, where we have used  $E = 38.7$  GPa. We observe that the crack-to-indent aspect ratio  $2c/D$  is in the range of 2 to 4.5, therefore within the range of applicability of the Evans model. It is seen that the computed fracture toughness  $K_c$  of indenting the (001) planes is higher than that when indenting the (100) planes. It is also observed that smaller crack sizes apparently produce higher fracture toughness. For  $2c/D$  values of 3 or higher, however, it is seen that the fracture toughness becomes independent of the geometry of the indent producing the cracks. For completeness, Fig. 86.66 shows the (average)  $\pm$  (one standard deviation) of the computed fracture toughness for each of the two orientations (1) and (2) on faces (001), as well as that for face (100). The standard deviation was computed from the fracture toughness variation over all the indenting loads used. The results for the two orientations of face (001) overlap, while exceeding that for (100).

The comparisons of the models by Evans<sup>9</sup> and Anstis *et al.*<sup>7</sup> are shown in Fig. 86.67. Both results are based on using Young's modulus  $E = 38.7$  GPa. We observe that the Evans model predicts fracture toughness that is a factor of 1.2 to 1.45 higher than the predictions of the Anstis model; however, both models give the same qualitative ranking of the data.

**Discussion**

The analysis above rests on two important assumptions. The first assumption is that the anisotropic KDP crystals can be analyzed for fracture toughness using an equivalent isotropic Young's modulus.

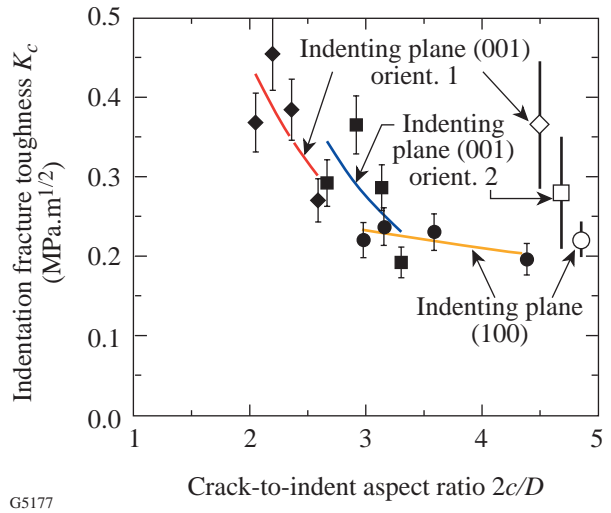


Figure 86.66 Dependence of fracture toughness computed via the Evans model<sup>9</sup> on the crack-to-indent aspect ratio  $2c/D$ , using the average Young's modulus  $E = 38.7$  GPa. Error bars on the data points reflect measurement uncertainty at each crack size. The thick vertical bars on the right show the (average)  $\pm$  (one standard deviation) for each indent orientation. The standard deviations shown on these bars reflect the variation of the fracture toughness over the whole range of indenting loads. To convert these values of fracture toughness to those with the minimum Young's modulus of  $E = 20.4$  GPa, multiply these values by 0.774.

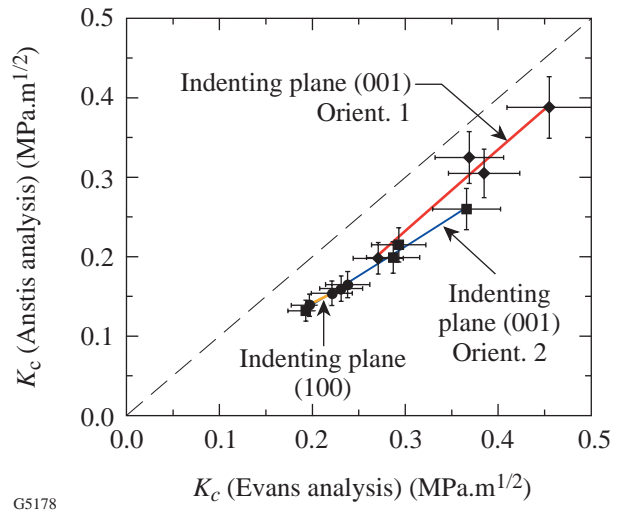


Figure 86.67 Comparison of prediction of fracture toughness by the Evans model<sup>9</sup> and the Anstis *et al.*<sup>7</sup> Results are for  $E = 38.7$  GPa. The dashed straight line is a line of slope 1.

To estimate the effect of such an assumption, for example, on the predictions by the Evans model, we observe that that model uses the term  $(E/H)^{0.4}$ . As the unconstrained Young's modulus  $E$  varies from 20.4 to 65 GPa, we conclude that the minimum fracture toughness corresponds to the lowest Young's modulus of 20.4 GPa. This, in turn, leads to a change in  $K_c$  by  $(20.4/38.7)^{0.4} = 0.774$ . Therefore, the effect of elastic anisotropy is estimated to be about 23% on the computed fracture toughness. These results are summarized in Table 86.V. In our data, we give the uncertainty over all the indenting loads used. It is seen that the Anstis *et al.* model,<sup>7</sup> when used in conjunction with the minimum Young's modulus of 20.4 GPa, yields fracture toughness in the range of  $0.09 \pm 0.02$  to  $0.22 \pm 0.06$  MPa.m<sup>1/2</sup>, in agreement with the values 0.09 to 0.2 MPa.m<sup>1/2</sup> cited by Marion.<sup>6</sup>

The other important assumption is that the material can be described as an elastic-plastic solid. With a melting point of  $T_m = 525.6$  K, the room temperature at which the tests were conducted represents a homologous temperature of  $293/525.6 = 0.57$ . At such a relatively high temperature, and under the action of the high compressive stresses due to indentation, it is expected that KDP may deform by a variety of mechanisms, including dislocation glide on crystallographic slip systems, or power-law creep by dislocation climb/glide. At temperatures of about 110°C, KDP is known to exhibit macroscopic plasticity in a uniaxial compression.<sup>5</sup> The room-temperature compressive yield stress does show anisotropy, being 140 MPa for compression along [100], 100 MPa along [110], and 130 MPa for compression along [001]. At 110°C, these values are

reduced by a factor of about 10;<sup>5</sup> therefore, anisotropy under uniaxial conditions is about 20% of the uniaxial compressive yield stress. The anisotropic variation of Knoop hardness that we have measured on the (001) faces was seen to be within 10% of the average value. Likewise, the largest observed difference in Vickers hardness of (100) and (001) faces was no more than about 10%. Therefore, a total variation of 20% in hardness due to crystallographic anisotropy is expected, consistent with the anisotropy of the uniaxial compressive yield stress. On the other hand, as Eqs. (3) and (4) show, a 20% variation in hardness is expected to lead to a variation in the computed fracture toughness of about 10%.

Thus, the estimates of the effects of the Young's modulus anisotropy and hardness anisotropy, when combined, lead to a difference of about 33% in the fracture toughness as computed by an isotropic elastic-plastic model such as by Evans<sup>9</sup> or Anstis *et al.*<sup>7</sup>

On the other hand, at a homologous temperature of 0.57 with respect to the melting point, power-law creep is a time-dependent process. Now, the strain rate depends on stress via a power law of exponent in the range of 3 to 8. In our experiments we have imposed a fixed strain rate, as determined by applying the indentation load for 15 s on the KDP faces. In typical laser-damage applications, the laser pulse duration over which damage accumulates is of the order of 10 ns, implying, therefore, that the applicable strain rates are much higher than those in indentation.

Table 86.V: Calculated fracture toughness  $K_c$  (Mpa.m<sup>1/2</sup>) for KDP.

Indents on	Using average $E = 38.7$ GPa		Using minimum $E = 20.4$ GPa	
	Evans model <sup>9</sup>	Anstis <i>et al.</i> model <sup>7</sup>	Evans model <sup>9</sup>	Anstis <i>et al.</i> model <sup>7</sup>
(100) plane	0.22±0.02	0.13±0.03	0.17±0.02	0.09±0.02
(001) plane, indent orientation (1)	0.37±0.08	0.30±0.08	0.29±0.06	0.22±0.06
(001) plane, indent orientation (2)	0.28±0.07	0.19±0.06	0.22±0.05	0.14±0.04
Shaskol'skaya <i>et al.</i> <sup>4</sup>	0.24±0.04	0.17±0.03	0.19±0.03	0.12±0.03
As cited in Marion <sup>6</sup>	0.09–0.20 Using direct crack method of Anstis <i>et al.</i> <sup>7</sup> but with no information on $E$ value used.			

Given the lack of data describing the dependence on stress and temperature of the deformation mechanisms of KDP, the strain-rate effects are more difficult to estimate. The development of deformation mechanism maps for KDP is thus an area identified for future research.

**ACKNOWLEDGMENT**

We wish to thank Prof. Stephen D. Jacobs and Mr. Douglas Smith, both of the Laboratory for Laser Energetics at the University of Rochester, for many discussions and suggestions and sample preparation.

**Appendix A: Elastic Anisotropy of KDP**

The elastic behavior of the single-crystal KDP is characterized by six elastic constants, which are shown in Table 86.VI.

Figure 86.68 shows the variation of the Young’s modulus of a rod of KDP with orientation of the rod. The figure shows the unconstrained Young’s modulus  $E_u$  (i.e., when the only stress is in the direction of the rod, without any transverse stresses):

$$\frac{1}{E_u} = \frac{S_{13}}{4} + \frac{S_{44}}{8} + S_{33} \cos^4 \theta - \frac{2S_{13} + S_{44}}{8} \cos 4\theta + \left[ S_{11} + \frac{(-2S_{11} + 2S_{12} + S_{66})}{4} \sin^2 2\phi \right] \sin^4 \theta, \quad (A1)$$

where  $\theta$  is the angle between the direction of the rod and the cubic axis [001] and  $\phi$  is the angle between the projection of the

rod axis on the (001) plane and the [100] direction. The Young’s modulus  $E_u$  varies from about 20 GPa to about 65 GPa. When averaged over all rod directions (i.e., integrated over the surface of a unit-radius sphere with differential element of area  $dA = \sin \theta d\theta d\phi$ ), we find  $\langle E_u \rangle = 35.5$  GPa.

Likewise, the constrained Young’s modulus  $E_c$  (where no strains transverse to the rod are allowed) is

$$E_c = \frac{C_{13}}{4} + \frac{C_{44}}{2} + C_{33} \cos^4 \theta - \frac{C_{13} + 2C_{44}}{4} \cos 4\theta + \left[ C_{11} + \frac{(-C_{11} + C_{12} + 2C_{66})}{2} \sin^2 2\phi \right] \sin^4 \theta; \quad (A2)$$

$E_c$  varies from about 40 GPa to 70 GPa, as shown in Fig. 86.68. When averaged over all directions, the result is  $\langle E_c \rangle = 51.4$  GPa. The results in Fig. 86.68 clearly show that KDP is quite anisotropic.

To get a better idea of the elastic anisotropy, we can also determine the Reuss and Voigt averages as described by Hirth and Lothe,<sup>16</sup> who summarize the earlier results by Hill.<sup>17</sup> The Voigt averages for the shear modulus  $G_V$  and Lamé constant  $\lambda_V$  are given by

$$G_V = (3C_{ijj} - C_{iij})/30, \quad \lambda_V = (-C_{iij} + 2C_{ijj})/15, \quad (A3)$$

Table 86.VI: Elastic constants of KDP at 20°C.

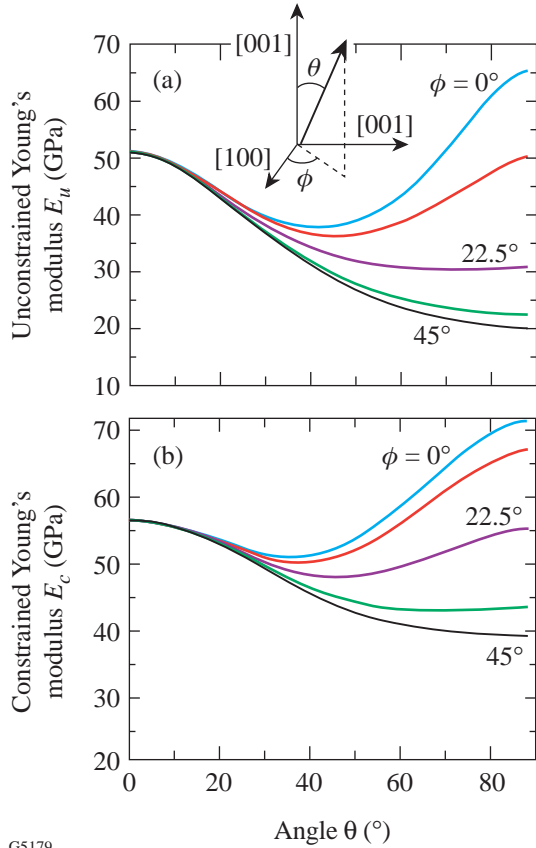
$C_{11}$	$C_{33}$	$C_{12}$	$C_{13}$	$C_{44}$	$C_{66}$
71.65	56.4	-6.27	14.94	12.48	6.21
Units of $C_{ij}$ are GPa; data from Haussühl, <sup>14</sup> as cited in Milek and Neuberger. <sup>1</sup> Stiffnesses $C_{ij}$ relates stresses and engineering strains.					
$S_{11}$	$S_{33}$	$S_{12}$	$S_{13}$	$S_{44}$	$S_{66}$
1.51	1.95	0.18	-0.40	7.81	16.2
Units of $S_{ij}$ are 1/(100 GPa); data from Hearmon, <sup>15</sup> as cited in Milek and Neuberger. <sup>1</sup> Compliances $S_{ij}$ relate engineering strains and stresses.					

where repeated indices are summed over the range  $i, j = 1, 2, 3$ . Here the constants  $C_{ijkl}$  relate the stress  $\sigma_{ij}$  and strain  $\epsilon_{ij}$  tensors,  $\sigma_{ij} = C_{ijkl} \epsilon_{kl}$ . We thus find the average Young's modulus based on the Voigt scheme as  $E_V = 44.3$  GPa. The corresponding Poisson ratio is  $\nu_V = 0.23$ .

The Reuss averages are given by

$$\frac{1}{E_R} = (2S_{ijj} + S_{ijj})/15, \quad \frac{1}{G_R} = (6S_{ijj} - 2S_{ijj})/15, \quad (A4)$$

where the constants  $S_{ijkl}$  relate the strain  $\epsilon_{ij}$  and stress  $\sigma_{ij}$  tensors,  $\epsilon_{ij} = S_{ijkl} \sigma_{kl}$ . We find the Reuss average of the Young's modulus  $E_R = 33.0$  GPa. The corresponding Poisson ratio is  $\nu_R = 0.30$ .



G5179

Figure 86.68  
Variation of Young's modulus of KDP with crystallographic orientation. The Young's modulus is the ratio of stress to strain for a rod making angles  $\theta, \phi$  with the crystallographic axes and stretched in the direction of the rod. Unconstrained  $E_u$  corresponds to no transverse stresses acting on the rod. Constrained  $E_c$  is valid when the rod is not allowed to strain in the transverse directions.

REFERENCES

1. S. Anbukumar, S. Vasudevan, and P. Ramasamy, *Indian J. Phys. A* **61A**, 397 (1987).
2. G. R. Anstis *et al.*, *J. Am. Ceram. Soc.* **64**, 533 (1981).
3. R. F. Cook and G. M. Pharr, *J. Am. Ceram. Soc.* **73**, 787 (1990).
4. A. G. Evans, in *Fracture Mechanics Applied to Brittle Materials*, edited by S. W. Freiman (American Society for Testing and Materials, Philadelphia, 1979), Vol. ASTM STP 678, Part 2, pp. 112–135.
5. C. H. Guin *et al.*, *Krist. Tech.* **15**, 479 (1980).
6. R. F. S. Hearmon, *Br. J. Appl. Phys.* **3**, 120 (1952).
7. S. Haussühl, *Z. Kristallogr.* **120**, 401 (1964).
8. R. Hill, *Proc. Phys. Soc.* **65A**, 349 (1952).
9. J. P. Hirth and J. Lothe, *Theory of Dislocations*, 2nd ed. (Wiley, New York, 1982), Chap. 13, Sec. 13.2, pp. 424–428.
10. K. K. Rao and D. B. Sirdeshmukh, *Indian J. Pure Appl. Phys.* **16**, 860 (1978).
11. J. C. Lambropoulos, T. Fang, P. D. Funkenbusch, S. D. Jacobs, M. J. Cumbo, and D. Golini, *Appl. Opt.* **35**, 4448 (1996).
12. J. Lankford, *J. Mater. Sci. Lett.* **1**, 493 (1982).
13. J. E. Marion, *J. Appl. Phys.* **62**, 1595 (1987).
14. J. T. Milek and M. Neuberger, *Linear Electrooptic Modular Materials*, Handbook of Electronic Materials, Vol. 8 (IFI/Plenum, New York, 1972), pp. 177–222.
15. C. B. Ponton and R. D. Rawlings, *Mater. Sci. Technol.* **5**, 865 (1989).
16. *ibid.*, p. 961.
17. M. P. Shaskol'skaya, H.-K. Ch'ang, and M. D. Katrich, *Izv. Akad. Nauk SSSR Neorg. Mater.* **14**, 716 (1978).



---

## Publications and Conference Presentations

---

### Publications

---

T. R. Boehly, Y. Fisher, D. D. Meyerhofer, W. Seka, J. M. Soures, and D. K. Bradley, "The Effect of Optical Prepulse on Direct-Drive Inertial Confinement Fusion Target Performance," *Phys. Plasmas* **8**, 231 (2001).

V. Yu. Glebov, D. D. Meyerhofer, C. Stoeckl, and J. D. Zuegel, "Secondary-Neutron-Yield Measurements by Current-Mode Detectors," *Rev. Sci. Instrum.* **72**, 824 (2001).

F. J. Marshall, T. Ohki, D. McInnis, Z. Ninkov, and J. Carbone, "Imaging of Laser-Plasma X-Ray Emission with Charge-Injection Devices," *Rev. Sci. Instrum.* **72**, 713 (2001).

A. V. Okishev, M. D. Skeldon, R. L. Keck, and W. Seka, "A New High-Bandwidth, All-Solid-State Pulse-Shaping System for the OMEGA Laser Facility," in *Laser Optics 2000: Ultrafast Optics and Superstrong Laser Fields*, edited by A. A. Andreev and V. E. Yashin (SPIE, Bellingham, WA, 2001), pp. 69–73.

A. B. Shorey, S. D. Jacobs, W. I. Kordonski, and R. F. Gans, "Experiments and Observations Regarding the Mechanisms of Glass Removal in Magnetorheological Finishing," *Appl. Opt.* **40**, 20 (2001).

C. Stoeckl, V. Yu. Glebov, D. D. Meyerhofer, W. Seka, B. Yaakobi, R. P. J. Town, and J. D. Zuegel, "Hard X-Ray Detectors for OMEGA and NIF," *Rev. Sci. Instrum.* **72**, 1197 (2001).

---

### Forthcoming Publications

---

R. Adam, R. Sobolewski, and M. Darula, "Subpicosecond Dynamics of the Switching Process in Y-Ba-Cu-O Josephson Junctions," to be published in *Oxide Superconductors: Physics and Nano-engineering IV*.

S. R. Arrasmith, S. D. Jacobs, I. A. Kozhinova, A. B. Shorey, D. Golini, W. I. Kordonski, S. Hogan, and P. Dumas, "Development and Characterization of Magnetorheological Fluids for Optical Finishing," to be published in the *Proceedings of Fine Powder Processing '99*, University Park, PA, 20–22 September 1999.

A. Babushkin, M. J. Harvey, and M. D. Skeldon, "The Output Signal-to-Noise Ratio of a Nd:YLF Regenerative Amplifier," to be published in *Applied Optics*.

R. Betti and J. P. Freidberg, "Low- $\beta$ , Magnetohydrodynamic Tokamak Equilibria with Poloidal Transonic Flow," to be published in *Physical Review Letters*.

T. R. Boehly, J. A. Delettrez, J. P. Knauer, D. D. Meyerhofer, B. Yaakobi, R. P. J. Town, and D. Hoarty, "The Effect of Shock Heating on the Stability of Laser-Driven Targets," to be published in *Physical Review Letters*.

T. R. Boehly, Y. Fisher, D. D. Meyerhofer, W. Seka, J. M. Soures, and D. K. Bradley, "The Effect of Optical Prepulses on Direct-Drive Inertial Confinement Fusion Target Performance," to be published in *Physics of Plasmas*.

T. R. Boehly, V. N. Goncharov, O. Gotchev, J. P. Knauer, D. D. Meyerhofer, D. Oron, S. P. Regan, Y. Srebro, W. Seka, D. Shvarts, S. Skupsky, and V. A. Smalyuk, "The Effect of Plasma Formation Rate and Beam Smoothing on Laser Imprinting," to be published in *Physical Review Letters*.

D. P. Butler, Z. Celik-Butler, and R. Sobolewski, "Y-Ba-Cu-O as an Infrared Radiation Sensing Material," to be published in the *Handbook of Advanced Electronic and Photonic Materials* (Academic Press, NY).

W. R. Donaldson, J. H. Kelly, R. L. Keck, and R. Boni, "Predicting and Measuring Optical Pulse Shapes on the OMEGA Laser System," to be published in *OSA Technical Digest*.

J. A. Frenje, D. G. Hicks, C. K. Li, F. H. Séguin, R. D. Petrasso, K. Fletcher, H. Olliver, S. Padalino, S. Thompson, J. M. Soures, S. Roberts, C. Sorce, T. C. Sangster, and T. W. Phillips, "CR-39 Tract Detector Response to Charged Particles and Neutrons," to be published in the *Review of Scientific Instruments*.

G. N. Gol'tsman, O. Okunev, G. Chulkova, A. Dzardanov, A. Lipatov, A. Semenov, K. Smirnov, B. Voronov, C. Williams, and R. Sobolewski, "Picosecond Superconducting Single-Photon Optical Detector," to be published in *Applied Physics Letters*.

V. N. Goncharov, P. W. McKenty, S. Skupsky, R. P. J. Town, R. Betti, and C. Cherfils-Clérouin, "Modeling Hydrodynamic Instabilities in Inertial Confinement Fusion Targets," to be published in *Physics of Plasmas*.

P. A. Jaanimagi, R. Boni, and R. L. Keck, "Neutron-Induced Background in CCD Detectors," to be published in the *Review of Scientific Instruments*.

C. K. Li, D. G. Hicks, F. H. Séguin, J. Frenje, R. D. Petrasso, J. M. Soures, P. B. Radha, V. Yu. Glebov, C. Stoeckl, J. P. Knauer, F. J. Marshall, D. D. Meyerhofer, S. Skupsky, S. Roberts, C. Sorce, T. C. Sangster, T. W. Phillips, and M. D. Cable, "Measuring Fusion Yields, Areal Densities, and Ion Temperatures of Imploded Capsules at OMEGA," to be published in the *Review of Scientific Instruments*.

V. Lobatchev and R. Betti, "Ablative Stabilization of the Deceleration-Phase Rayleigh-Taylor Instability," to be published in *Physical Review Letters*.

A. E. Marino, S. D. Jacobs, L. L. Gregg, G. Chen, and Y. Due, "Durable Phosphate Glasses with Lower Transition Temperatures," to be published in the *Journal of Non-Crystalline Solids*.

J. A. Marozas, "Self- and Cross-Phase Modulation of High-Intensity Laser Beams Emerging from a Diamond-Turned KDP Wedge," to be published in the *Journal of the Optical Society of America B*.

J. A. Marozas, S. P. Regan, J. H. Kelly, D. D. Meyerhofer, W. Seka, and S. Skupsky, "Laser Beam Smoothing Caused by the Small-Spatial-Scale  $\beta$ -Integral," to be published in the *Journal of the Optical Society of America B*.

J. A. Marozas, J. D. Zuegel, D. Jacobs-Perkins, and J. H. Kelly, "Angular Spectrum Representation of Pulsed Laser Beams with Two-Dimensional Smoothing by Spectral Dispersion," to be published in the *Journal of the Optical Society of America B*.

R. L. McCrory, R. E. Bahr, R. Betti, T. R. Boehly, T. J. B. Collins, R. S. Craxton, J. A. Delettrez, W. R. Donaldson, R. Epstein, J. Frenje, V. Yu. Glebov, V. N. Goncharov, O. V. Gotchev, R. Q. Gram, D. R. Harding, D. G. Hicks, P. A. Jaanimagi, R. L. Keck, J. Kelly, J. P. Knauer, C. K. Li, S. J. Loucks, L. D. Lund, F. J. Marshall, P. W. McKenty, D. D. Meyerhofer, S. F. B. Morse, R. D. Petrasso, P. B. Radha, S. P. Regan, S. Roberts, F. Seguin, W. Seka, S. Skupsky, V. A. Smalyuk, C. Sorce, J. M. Soures, C. Stoeckl, R. P. J. Town, M. D. Wittman, B. Yaakobi, and J. D. Zuegel, "OMEGA ICF Experiments and Preparation for Direct-Drive Ignition on NIF," to be published in the proceedings of the 18<sup>th</sup> IAEA Fusion Energy Conference.

A. V. Okishev, R. Boni, M. Millecchia, P. A. Jaanimagi, W. R. Donaldson, R. L. Keck, W. Seka, K. V. Dukelsky, M. A. Eronyan, V. S. Shevandin, G. A. Ermolaeva, G. Nikolaev, and V. B. Shilov, "Unique High-Bandwidth, UV Fiber Delivery System for the OMEGA Diagnostic Applications," to be published in the *IEEE Journal on Selected Topics in Quantum Electronics*.

F. H. Séguin, C. K. Li, D. G. Hicks, J. A. Frenje, R. D. Petrasso, J. M. Soures, V. Yu. Glebov, C. Stoeckl, P. B. Radha, D. D. Meyerhofer, S. Roberts, C. Sorce, T. C. Sangster, and M. D. Cable, "Diagnostic Use of Secondary D<sup>3</sup>He Proton Spectra for D-D OMEGA Targets," to be published in *Physics of Plasmas*.

M. D. Skeldon, "An Optical-Pulse-Shaping System Based on an Electrooptic Modulator Driven by an Aperture-Coupled-Stripline Electrical-Waveform Generator," to be published in the *Journal of the Optical Society of America B*.

S. Skupsky, R. L. McCrory, R. E. Bahr, T. R. Boehly, T. J. B. Collins, R. S. Craxton, J. A. Delettrez, W. R. Donaldson, R. Epstein, V. N. Goncharov, R. Q. Gram, D. R. Harding, P. A. Jaanimagi, R. L. Keck, J. P. Knauer, S. J. Loucks, F. J. Marshall, P. W. McKenty, D. D. Meyerhofer, S. F. B. Morse, O. V. Gotchev, P. B. Radha, S. P. Regan, W. Seka, V. A. Smalyuk, J. M. Soures, C. Stoeckl, R. P. J. Town, M. D. Wittman, B. Yaakobi, J. D. Zuegel, R. D. Petrasso, D. G. Hicks, and C. K. Li, "Recent Progress in Direct-Drive ICF Research at the Laboratory for Laser Energetics," to be published in SPIE's Proceedings of the XXVI European Conference on Laser Interaction with Matter.

V. A. Smalyuk, T. R. Boehly, L. S. Iwan, T. J. Kessler, J. P. Knauer, F. J. Marshall, D. D. Meyerhofer, C. Stoeckl, B. Yaakobi, and D. K. Bradley, "Fourier-Space Image Processing for Spherical Experiments on OMEGA," to be published in the *Review of Scientific Instruments*.

V. A. Smalyuk, B. Yaakobi, J. A. Delettrez, F. J. Marshall, and D. D. Meyerhofer, "Compressed-Shell Integrity Measurements in Spherical Implosion Experiments," to be published in *Physics of Plasmas*.

V. A. Smalyuk, B. Yaakobi, J. A. Delettrez, F. J. Marshall, D. D. Meyerhofer, S. P. Regan, and R. P. J. Town, "Evolution of Shell Nonuniformities Near Peak Compression of Spherical Implosion," to be published in *Physical Review Letters*.

D. J. Smith, J. A. Warner, N. E. LeBarron, T. J. Kessler, and S. LaDelia, "The Development of Ion-Etched Phase Plates," to be published in *Applied Optics*.

E. A. Startsev and C. J. McKinstrie, "Relativistic Ponderomotive Dynamics of a Test Particle in a Plasma," to be published in *Physical Review E*.

B. Yaakobi, C. Stoeckl, T. Boehly, D. D. Meyerhofer, and W. Seka, "Measurement of Preheat due to Fast Electrons in Laser Implosions," to be published in SPIE's Proceedings of the XXVI European Conference on Laser Interaction with Matter.

J. D. Zuegel and D. W. Jacobs-Perkins, "An Efficient, High-Frequency Bulk Phase Modulator," to be published in *Applied Optics*.

J. D. Zuegel and S. A. Letzring, "Bulk Microwave Phase Modulators for Smoothing by Spectral Dispersion," to be published in *Applied Optics*.

---

### Conference Presentations

---

L. Waxer and J. Kelly, "Spectral Sculpting for NIF Demonstration Project," Third Annual Joint US-JAPAN Workshop on Laser-Driven Inertial Fusion Energy (IFE), Livermore, CA, 25–27 January 2001.

W. Seka, S. P. Regan, D. D. Meyerhofer, B. Yaakobi, C. Stoeckl, R. S. Craxton, R. W. Short, H. A. Baldis, and J. Fuchs, "Multibeam Interaction Experiments Under Direct-Drive NIF Conditions," 4th International Workshop on Laser-Plasma Interaction Physics, Banff, Alberta, Canada, 21–24 February 2001.

UNIVERSITY OF  
ROCHESTER